# Chem Soc Rev

Chemical Society Reviews
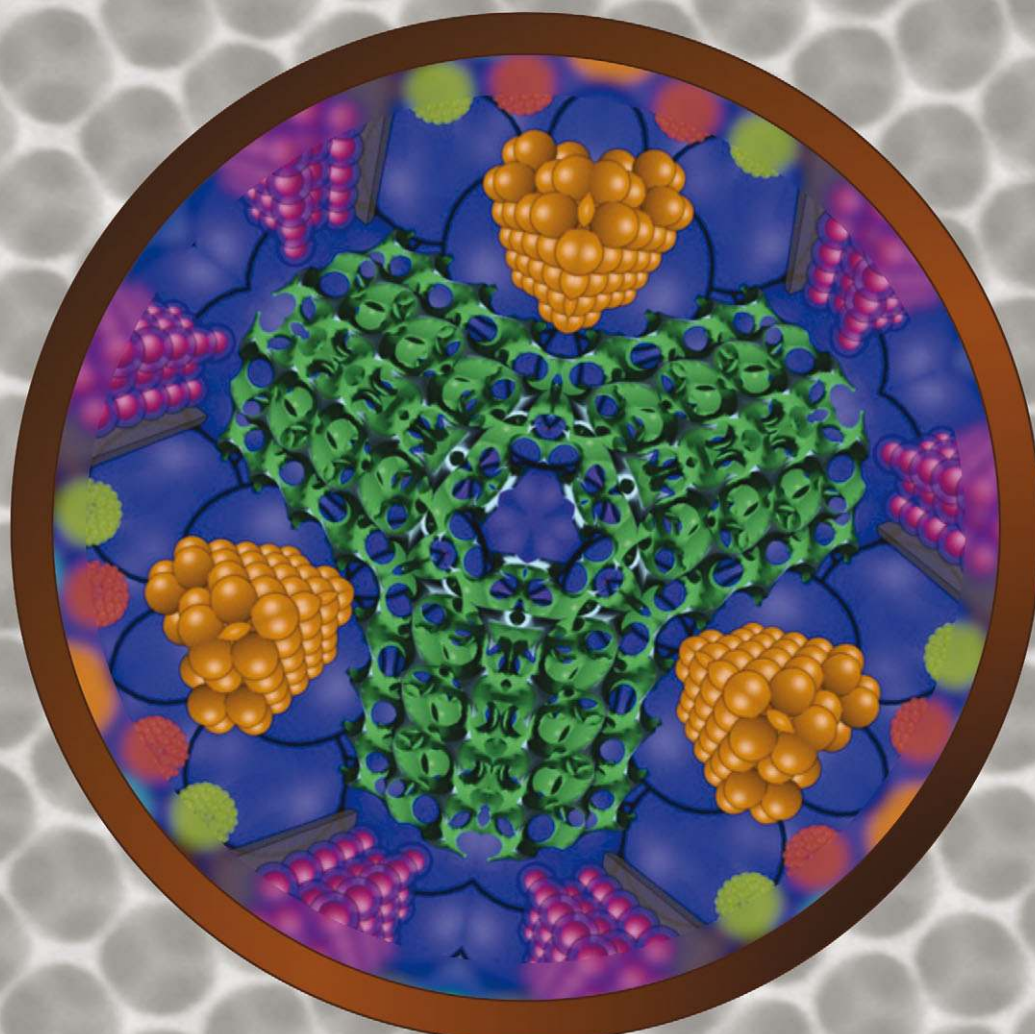
Themed issue: Bioinspired surfaces and materials

ROYAL SOCIETY
OF CHEMISTRY

**REVIEW ARTICLE**
Joanna Aizenberg *et al.*
A colloidoscope of colloid-based porous materials and their uses

175 YEARS

# A colloidoscope of colloid-based porous materials and their uses

Katherine R. Phillips,[a] Grant T. England,[b] Steffi Sunny,[b] Elijah Shirman,[bc] Tanya Shirman,[bc] Nicolas Vogel[de] and Joanna Aizenberg*[abc]

Nature evolved a variety of hierarchical structures that produce sophisticated functions. Inspired by these natural materials, colloidal self-assembly provides a convenient way to produce structures from simple building blocks with a variety of complex functions beyond those found in nature. In particular, colloid-based porous materials (CBPM) can be made from a wide variety of materials. The internal structure of CBPM also has several key attributes, namely porosity on a sub-micrometer length scale, interconnectivity of these pores, and a controllable degree of order. The combination of structure and composition allow CBPM to attain properties important for modern applications such as photonic inks, colorimetric sensors, self-cleaning surfaces, water purification systems, or batteries. This review summarizes recent developments in the field of CBPM, including principles for their design, fabrication, and applications, with a particular focus on structural features and materials' properties that enable these applications. We begin with a short introduction to the wide variety of patterns that can be generated by colloidal self-assembly and templating processes. We then discuss different applications of such structures, focusing on optics, wetting, sensing, catalysis, and electrodes. Different fields of applications require different properties, yet the modularity of the assembly process of CBPM provides a high degree of tunability and tailorability in composition and structure. We examine the significance of properties such as structure, composition, and degree of order on the materials' functions and use, as well as trends in and future directions for the development of CBPM.

## 1. Introduction

Functional properties in nature often arise from hierarchical structuration in a variety of forms. In particular, unique and interesting properties occur due to structure between the molecular and bulk scales even with common materials. For example, some feathers have bright blue colors,[1–5] chameleons can change color,[6] and Lotus leaves are hydrophobic,[7–10] as shown in Fig. 1A; additionally, many seeds,[11] shells,[12] and butterfly wings[13–16] have bright iridescent colors, and shells can have high fracture toughness.[17,18] Generally, the structure of a material on the nano to microscale strongly affects its optical, wetting, mechanical, and chemical properties; thus, controlling features on this length scale can lead to a myriad of materials possibilities.

Synthetically, monodisperse colloids can be made and subsequently used to create structures similar to those found in nature, where simple building blocks are used to achieve a variety of functions despite a limited materials space. Self-assembly of colloids creates nanoscale features simply, inexpensively, and quickly over large areas from the bottom up by taking advantage of molecular interactions that lead to the assembly of nanoscale building blocks.[19] Block copolymers can also be used, to achieve features below 100 nm,[20,21] whereas colloids are in the range between 100 nm and 1000 nm (1 μm). Colloids can be used to make colloid-based porous materials (CBPM), which provide the ability to control important aspects of the structure including porosity and order (Fig. 1B). Control over the CBPM structure on the colloidal length scale is particularly useful because many important properties occur at this scale, such as the wavelength of visible light, providing CBPM the ability to control many physical phenomena. By expanding the range of materials beyond what nature uses, synthetic CBPM can achieve a variety of structures with specific compositions, leading to properties beyond those found in natural mesoscale materials, for example for catalytic and electrochemical uses. Indeed, CBPM fabrication methods allow for a highly tailorable composition and structure.

[a] Department of Chemistry and Chemical Biology, Harvard University, Cambridge, USA

[b] John A. Paulson School of Engineering and Applied Sciences, Harvard University, Cambridge, USA. E-mail: jaiz@seas.harvard.edu

[c] Wyss Institute for Biologically Inspired Engineering, Harvard University, Cambridge, USA

[d] Institute of Particle Technology, Friedrich-Alexander-University Erlangen-Nürnberg, Erlangen, Germany

[e] Cluster of Excellence Engineering of Advanced Materials, Friedrich-Alexander-University Erlangen-Nürnberg, Erlangen, Germany

This journal is © The Royal Society of Chemistry 2016

*Chem. Soc. Rev.*, 2016, **45**, 281–322 | 281

In this review, the underlying theme is the influence of CBPM structure on their macroscopic properties. We start our discussion with a short introduction to colloidal self-assembly and templating processes and survey the variety of structures and patterns that can be generated. We then introduce and critically review different application fields of such structures and discuss the desired key properties for different applications and how colloidal self-assembly processes can be applied to

meet these requirements. We focus on the areas of optics, wetting, sensing, catalysis, and electrodes, as summarized in Fig. 1C, to illustrate the scope of colloidal assemblies, using specific but not exhaustive examples. While biology uses mainly organic building blocks, different technological applications require more specialized materials. A variety of materials can be incorporated into CBPM structures including metals, metal oxides, and polymers. All applications benefit from the tunability, tailorability, and
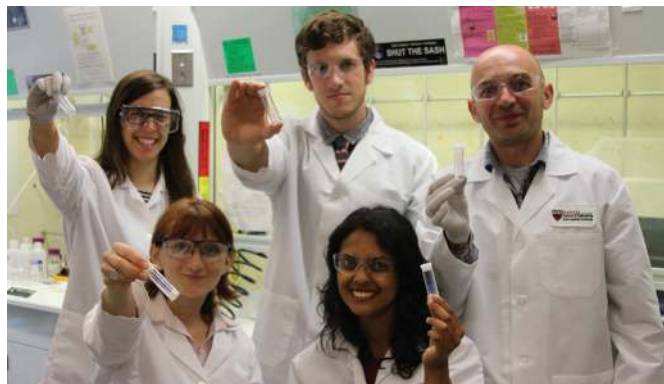
**Clockwise from top left: Katherine R. Phillips, Grant T. England, Dr Elijah Shirman, Steffi Sunny and Dr Tanya Shirman**

*Katherine Phillips graduated from Brown University in 2010 with an ScB in chemistry and mathematics. She subsequently joined the Department of Chemistry and Chemical Biology at Harvard, where she is a PhD candidate in the group of Prof. Joanna Aizenberg. Her research interests broadly include using chemistry to make nanomaterials for optical, catalytic, and electrochemical uses, and she is currently working to develop sol–gel processes for the fabrication of inverse opals with optical and catalytic functions.*

*Grant T. England obtained his BE in electrical engineering and mathematics in 2009 from Vanderbilt University. He is currently pursuing a PhD in Applied Physics in the John A. Paulson School of Engineering and Applied Sciences at Harvard working with Prof. Joanna Aizenberg. His research is focused on bio-inspired photonics and structurally colored materials.*

*Dr Elijah Shirman received a BSc and MSc in Physical Chemistry from the Hebrew University and a PhD from the Weizmann Institute of Science, in Israel, working on laser-induced processes and self-assembled photoactive molecular structures. As a postdoc at Tufts University, he worked on silk-based photonic crystals and hybrid bioelectronic devices. He then moved to the Aizenberg group, where he focuses on the development of sensors and adaptive photonic materials using a combination of colloidal self-assembly, nanofabrication, surface chemistry, and microfluidic methods.*

*Steffi Sunny completed her undergraduate degree in Nanotechnology Engineering at the University of Waterloo in 2012. She is currently pursuing a PhD in Bioengineering in the John A. Paulson School of Engineering and Applied Sciences at Harvard in the group of Prof. Joanna Aizenberg. Steffi's research in the Aizenberg group involves work on omniphobic surfaces and their applications.*

*Dr Tanya Shirman received her PhD in chemistry from the Weizmann Institute of Science. In 2012, she joined the group of Prof. Joanna Aizenberg as a postdoctoral fellow. In 2014, she was appointed Technology Development Fellow at the Wyss Institute for Biologically Inspired Engineering at Harvard University. She is working on a variety of projects focusing on the development of dynamic optical and functional materials based on structural color and inorganic nanoparticles for production of industrially valuable pigments and catalysts.*



**Prof. Nicolas Vogel**

*Prof. Nicolas Vogel studied chemistry at the Johannes Gutenberg-University in Mainz, Germany and Seoul National University in Seoul, Republic of Korea. In 2011, he received his PhD at the Max Planck Institute for Polymer Research in Mainz. He then joined the group of Prof. Joanna Aizenberg at Harvard University as a postdoctoral fellow. In 2014, he was appointed associate professor in the Department of Chemical and Biological Engineering at the Friedrich-Alexander-University Erlangen-Nuremberg. He likes to apply colloidal assembly to create functional materials and coatings, for example for structural color or tailored wetting properties.*



**Prof. Joanna Aizenberg**

*Prof. Joanna Aizenberg received a BS and MS in Chemistry from the Moscow State University, and a PhD in Structural Biology from the Weizmann Institute of Science. She then did postdoctoral research at Harvard University on micro/nanofabrication and near-field optics. After nearly a decade at Bell Labs, she joined the School of Engineering and Applied Sciences and Department of Chemistry and Chemical Biology at Harvard University in 2007. She is a pioneer of the rapidly developing field of biomimetic materials synthesis, using basic principles of biological design to develop advanced new materials.*
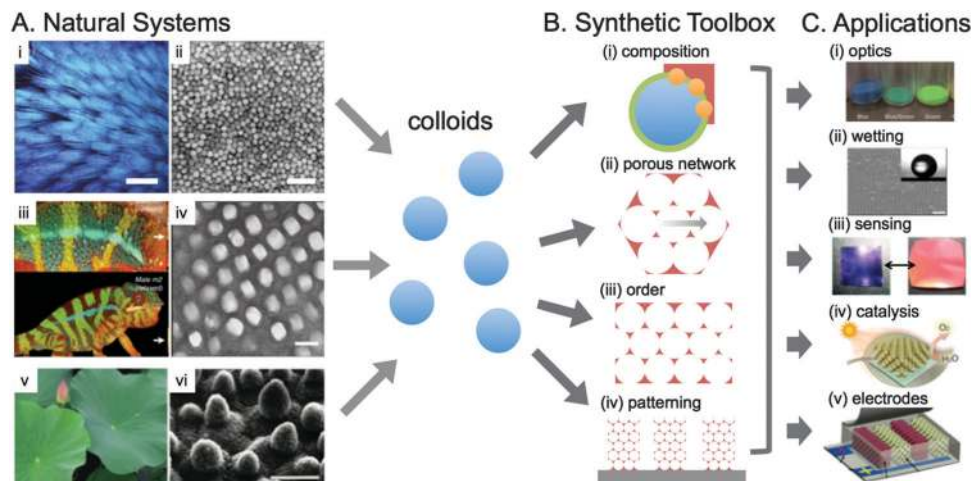
Fig. 1 Colloidal particles, from biology to applications. (A) Biological examples of structures on the colloidal length scale: (i and ii) disordered particles provide the crown feathers of the *Lepidothrix coronata* butterfly with a vivid blue color (scale bars = 200 mm (left), 1 μm (right)),[4] reproduced with permission from John Wiley and Sons, copyright 2010; (iii and iv) the skin of a *Furcifer pardalis* panther chameleon changes color in response to excitement as a result of the changing periodicity of the underlying structure (scale bar = 200 nm),[6] reproduced with permission from Nature Publishing Group, copyright 2015; and (v and vi) a lotus leaf has self-cleaning properties due to the microstructure of the surface (scale bar = 20 μm),[7] reproduced with permission from the Royal Society of Chemistry, copyright 2008. (B) Properties and degrees of freedom of colloidal assemblies. (C) Application areas that particularly benefit from using colloid-based materials are optics,[22] wetting,[23] sensing,[24] catalysis,[25] and electrodes.[26] Reproduced with permission from John Wiley and Sons (copyright 2014), the American Chemical Society (copyright 2004, 2013, and 2014), and Nature Publishing Group (copyright 2013).

hierarchy of CBPM, originating from the variety of fabrication and assembly methods. Much of the review focuses primarily on inverse opals, ordered structures templated from colloidal crystals, but we include comparisons with disordered and direct (untemplated) structures as well. We intend to highlight the versatility of colloid-based materials by providing a "colloidoscope" – an overview ranging from the multitude of available structures and their specific properties to a discussion of their advantages and potentials in a wide range of technological applications.

## 2. Fabrication of colloidal assemblies

A rich variety of structures can be generated by self-assembly using even the simplest colloidal particles as building blocks. We focus on spherical colloidal particles, typically prepared in the size range from 100 nm to several μm, made from common materials without any inherent special properties (mostly polystyrene, poly(methylmethacrylate), and silica),[27] rather than assemblies of functional nanoparticles. Such colloids can be synthesized with high precision and uniformity using emulsion polymerization,[28,29] dispersion polymerization,[30,31] and Stöber processes.[32,33] The composition can later be tailored as desired, as discussed below and described in Fig. 2. With the focus on the assembly of simple, spherical particles, this review does not cover the synthesis and self-assembly of more complex colloidal building blocks, such as Janus particles,[34,35] patchy particles,[36–39] core–shell particles,[40–42] particles with more complex internal structures,[43–45] anisotropic particles,[46] or non-spherical nanocrystals.[47–50]

Complex properties and highly functional materials can emerge solely by controlling the structure of the material or by providing a template to generate patterns in another material.
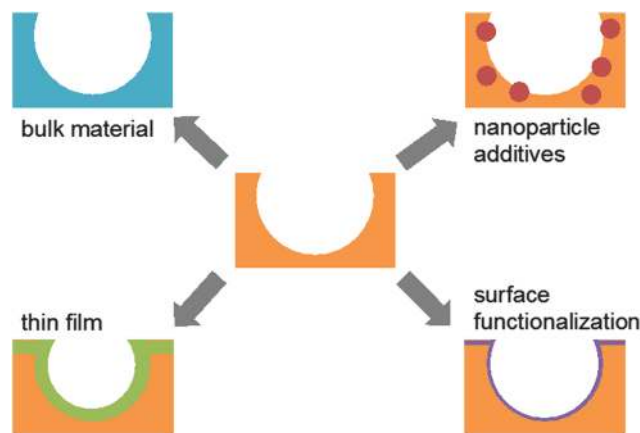


Fig. 2 Overview of various methods to control CBPM composition. The material itself can be controlled, functional additives such as nanoparticles can be used, and the surface can be modified, either with a conformal thin film or with a molecular surface layer.

The classical structures created by spherical assemblies are direct opals, consisting of three-dimensional assemblies of colloidal particles in the ordered arrangement of a face centered cubic crystal (Fig. 3A), and their inverse analogues created by backfilling the interstitial sites with a second material and subsequent removal of the colloids which serve as templates to generate an interconnected, porous matrix (Fig. 3C).

Within this chapter, we will briefly introduce the important structural aspects of colloidal assemblies and highlight the modularity and versatility of these structures. We organize the chapter according to the length scale of structures, starting from the composition of the material, *via* order and porosity of CBPM to a short overview of types of assemblies and

This journal is © The Royal Society of Chemistry 2016

*Chem. Soc. Rev.*, 2016, 45, 281–322 | 283
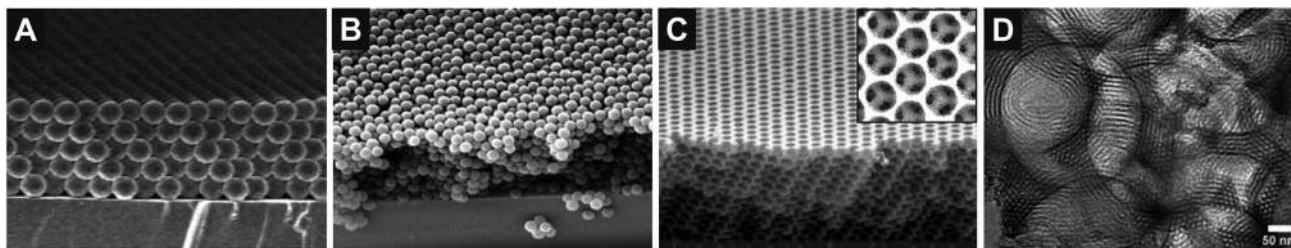
**Fig. 3** Colloidal assembly structures with different order and porosity. (A) Direct colloidal crystal, or opal.[80] Reproduced with permission from the American Chemical Society, copyright 2013. (B) Disordered assembly of colloids.[4] Reproduced with permission from John Wiley and Sons, copyright 2010. (C) Inverse colloidal crystal, or inverse opal, prepared by filling the interstitial sites of the colloidal assembly and removing the colloidal template.[59] Reproduced with permission from the National Academy of Sciences, copyright 2010. (D) Mesoporous–macroporous material from colloidal templating, where the inverse opal matrix is further structured with mesopores.[81] Reproduced with permission from the Royal Society of Chemistry, copyright 2010.

superstructures that can be created across several dimensions and length scales.

### 2.1 Control over structural features in colloidal assemblies

**Composition.** There is a high degree of control over the composition of CBPM even using simple building blocks. Some of the key benefits of CBPM are the modularity of the matrix material, the additives, and the surface chemistry, as shown in Fig. 2.

*(A) Bulk material.* The material choice for the colloidal particles is limited by the synthetic possibilities to prepare monodispersed spheres. There are numerous approaches to create metallic,[41,51] polymeric,[52,53] semiconducting,[48] and oxidic[49,50] nanoparticles, but the vast majority of colloidal assembly structures are prepared from simple polymer or silica particles.[27,54–56] Inverse structures have much more pronounced material variety since the matrix material can be chosen freely, provided it can fill the interstitial sites of the template crystal. By controlling the matrix material separately from the assembly process, one can combine properties of the structure (interconnected pores, high order, high surface area) with inherent material properties.[57,58] The variety of materials that can be used forms the basis for applications of colloidal structures in sensing, catalysis, and electrode materials, and specific examples will be discussed in these sections. These inverse structures are generally made by backfilling a pre-formed colloidal template with a precursor for the matrix material; however, when the matrix and colloids are co-assembled simultaneously, the resulting structure has better long-range order and fewer cracks.[59]

*(B) Nanoparticle additives.* The addition of functional nanoparticles within the architecture provided by the colloids can be used to add further functional properties. For example, carbon black[60] or gold nanoparticles[61] can be used for their absorbing properties, or catalytically active nanoparticles[62–64] can be embedded into the matrix material.

*(C) Surface modification.* Additional functional properties can be introduced to the inverse opal matrix by various surface modification techniques. The interconnected porosity enables the entire surface to be modified uniformly, for example using atomic layer deposition (ALD)[65–72] or electrodeposition[26,73–76] techniques.

The matrix material can also be conveniently chosen to allow for simple and reliable introduction of a rich variety of surface functionalities at a molecular level, for example *via* silane chemistry.[77,78]

**Porosity and order.** As colloids start to assemble, they form porous structures that can have a degree of order from single crystalline to amorphous. Using the colloids as a template and inverting the structure allows one to form macropores (defined as those with pore diameter $\geq \sim 30$ nm[79]) with interesting fluid and gas transport properties.

*(A) Order.* The self-assembly of colloidal particles in three dimensions creates close-packed structures with long-range order if the particles are sufficiently similar in size and if the assembly process is well-controlled.[54–56] The colloids assemble in a face-centered cubic crystal structure with periodicities in the hundred-nanometer range, as defined by the individual colloidal particle size. Colloidal crystals, for example in Fig. 3A, are also known as opals.

*(B) Disorder.* While the assembly of colloids into ordered structures require monodisperse particles and careful control over assembly conditions,[54–56] disordered assembly structures can be prepared more easily. Polydisperse particles, which are unable to crystallize in an ordered matrix, can be used to prepare amorphous assemblies without long-range order (Fig. 3B).[4,82] Simplistic and scalable approaches such as spray coating[83,84] or layer-by-layer assembly[85,86] of particles that are not suitable for crystallization due to high attractive forces or insufficient crystallization time can still be used to prepare disordered assembly structures in an experimentally straightforward way. Indeed, as we discuss in detail in several of the following sections, order is not necessary for every application of CBPM, and controlled disorder may even create desired properties.

*(C) Ordered porosity.* The inversion of a colloidal crystal, by backfilling the interstitial sites with a matrix material followed by removal of the templating colloids, produces materials with interconnected pores with uniform, defined neck sizes and long-range order inherited from the colloid templates (Fig. 3C).[57,58] These inverse opals are the subject of extensive research and will be discussed in depth in the following chapters. Direct opals

are also porous and interconnected, although the pores are not spherical and the degree of porosity much lower.

*(D) Multiple porosities.* To create porous materials with increasing complexity, additional interfaces and pores over multiple length scales can be fabricated by co-crystallizing particle populations with different sizes,[87,88] or by introducing porogens to produce mesopores within the matrix material (Fig. 3D).[81]

**Assembly structures and patterning.** As showcased in Fig. 4, colloidal assemblies and structures prepared from colloidal templates can be classified according to their dimensionality into: (A) colloidal monolayers, providing two-dimensional surface patterns; (B) colloidal crystals with periodic internal structures in three dimensions; (C) hierarchical assemblies, creating structural features at multiple length scales on solid substrates; and (D) superparticles, dispersible structures several microns wide and made from colloidal building blocks.

There have been a number of very recent review articles covering all facets of colloidal assembly, which we will refer to throughout the discussion. Nature creates these structures
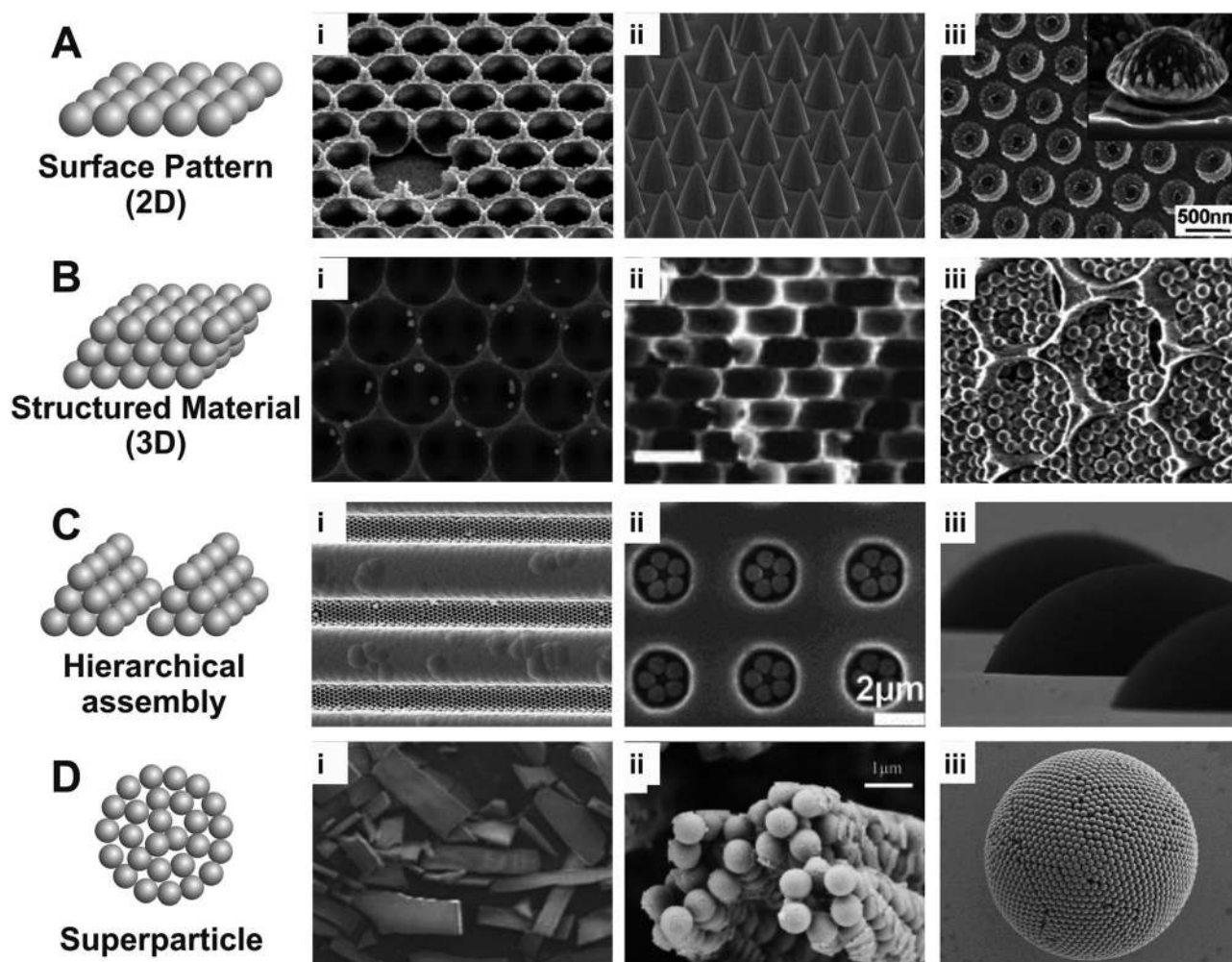


Fig. 4 Overview of types of patterned structures that can be created from colloidal self-assembly processes. (A) Colloidal monolayers create periodic surface structures at the nanoscale that can be used as templates or masks to produce (i) a honeycomb structure by backfilling with a second material[95] (reproduced with permission from Nature Publishing Group, copyright 2013), (ii) an array of nanocones from anisotropic etching processes using the colloids as a mask[96] (reproduced with permission from the American Chemical Society, copyright 2009), or (iii) complex nanostructures by a combination of angular evaporation and etching involving the monolayer as template[97] (reproduced with permission from the American Chemical Society, copyright 2011). (B) 3D porous materials from inverted colloidal crystals (i) with gold nanoparticles embedded inside[98] (reproduced with permission from the American Chemical Society, copyright 2012), (ii) with anisotropic pore shape[99] (reproduced with permission from the American Chemical Society, copyright 2014), and (iii) with two distinct periodicities[88] (reproduced with permission from John Wiley and Sons, copyright 2013). (C) Hierarchical assemblies produce materials with periodicities at multiple length scales and can be prepared by (i) photolithography of a self-assembled structure[100] (reproduced with permission from John Wiley and Sons, copyright 2015), (ii) assembly in a topographically structured substrate[101] (reproduced with permission from the American Chemical Society, copyright 2001), or (iii) inkjet printing of colloidal dispersions[102] (reproduced with permission from Elsevier, copyright 2006). (D) Assembly in confinement can also produce superparticles, micron-scale structures of self-assembled colloidal particles, for example *via* confinement in (i) surface channels on a substrate, producing bricklike structures[103] (modified with permission from OSA publishing, copyright 2014), (ii) a silicone microtube, forming a helical superstructure of colloidal particles[104] (reproduced with permission from the American Chemical Society, copyright 2005), or (iii) emulsion droplets, producing spherical superparticles[105] (reproduced with permission from the National Academy of Sciences, copyright 2015).

This journal is © The Royal Society of Chemistry 2016

*Chem. Soc. Rev.,* 2016, **45**, 281–322 | 285

from 100–1000 nm proteinaceous or lipid particles assembling into ordered structures.[89,90] In synthetic systems, the interplay of colloid interaction forces is the key factor in the control of any colloidal self-assembly process. Within this review, we focus on material and design aspects rather than colloidal physics, which has been exhaustively discussed elsewhere.[91–94]

(A) *Two-dimensional assembly structures.* The assembly of two-dimensional (2D) arrays of colloidal particles creates surface patterns with nanoscale dimensions and high order, with a resolution determined solely by the size of the colloids (Fig. 4A). Such monolayers can be deposited directly onto solid substrates *via* evaporation-driven convective assembly processes,[106–108] spin-coating,[109] electric field-assisted deposition,[55,110] or mechanical rubbing of dry powders.[111,112] They can also be pre-assembled at a liquid interface and subsequently transferred to a solid substrate.[113–116] The choice of assembly technique depends on the requirements with respect to the area to be coated, which have recently been discussed in detail.[52,117]

Colloidal monolayers can be especially valuable as templates or masks for etching or evaporation processes to create functional surface nanostructures or coatings. There have been intense research activities in the last decade on the generation of arrays of nanostructures using colloidal monolayers, as discussed in several recent review articles;[117–120] here, we only introduce general strategies and highlight a few examples in Fig. 4A.

(i) *Inversion of the monolayer structure.* Backfilling colloidal monolayers produces bowl-shaped, closed-cell nanostructures with high mechanical stability (Fig. 4A(i)).[95] Very similar structures with microscale dimensions can also be created using water droplets as the structuring material in a breath figure process.[121]

(ii) *Dry etching using colloidal monolayer masks.* The presence of colloids can shield parts of the surface from an etching process, leading to selective removal of exposed surface areas. Classically, this process produces ordered arrays of nanopillar[122] and nanocone[96] architectures (Fig. 4A(ii)).

(iii) *Colloidal lithography.* A colloidal monolayer can be used as a mask through which a second material can be deposited on the surface, typically by directed evaporation. In the simplest case, this process yields arrays of triangular nanoparticles from the geometry of the interstitial sites.[123] The process offers ample degrees of freedom: consecutive evaporation steps with changes in tilt angle and orientation of the substrate can create a range of complex nanostructures.[124] Adding directed dry etching steps to selectively remove material from defined parts of the surface further increases the accessible structures and geometries.[117,120] Fig. 4A(iii) shows the fabrication of arrays of crescent shaped nanoparticles by a combination of evaporation of gold under a tilted angle followed by an etching step normal to the surface.[97,125] Similarly, the colloids themselves can be used to deposit the metal using colloids that contain metal nanoparticles or molecular metal complexes as precursor materials.[126,127]

(iv) *Capillary-assisted deposition of structures.* If a colloid-decorated substrate is wetted by a dispersion of nanoparticles,

capillary forces confine the liquid to the necks in between particles and between the particles and the substrate during the drying process, leading to the formation of ring structures from nanoparticles deposited selectively at the contact points.[128]

(B) *Three-dimensional colloidal assemblies.* Three-dimensional (3D) colloidal crystals are predominantly prepared by convective assembly processes in which the colloidal particles are deposited from a dispersion *via* a receding meniscus.[107,108,129] Research over two decades has created a wealth of different assembly techniques under this umbrella, which are discussed in great detail in a number of recent reviews.[54–56,92,130] Briefly, methods to assemble colloidal particles into ordered three-dimensional crystals include sedimentation,[131,132] Langmuir–Blodgett techniques,[133] spin-coating,[134] and shear alignment.[135,136] Using evaporative deposition, nanoparticles can also be easily incorporated into the structure (Fig. 4B(i)).[61,98]

(i) *Control of crystal symmetry.* The substrate onto which colloidal particles assemble can be pre-structured with a defined hole pattern into which the first layer of the colloidal particles deposits in a process called colloidal epitaxy.[137] The surface pattern thus acts as a lattice-directing layer that defines the symmetry and lattice orientation of the colloidal particles,[138] predominantly into face-centered cubic structures.[55] Each subsequent layer consequently deposits into the voids present in the former layer, enabling the substrate pattern to control the macroscopic crystal orientation of the assembly structure, provided that the template structure exactly matches the size of the colloidal spheres. The process allows the formation of colloidal crystals with controllable crystal structures[138] and enables rapid fabrication of assemblies with minimal defect densities.[139]

(ii) *Control of pore shape.* Inverse opals with anisotropic pore structures can be prepared from simple spherical colloidal particles by exploiting volume shrinkage of the sol–gel matrix material: with increasing temperature, increased condensation induces volume loss in the matrix, which in turn leads to a selective shrinkage of the inverse opal film. Since this film is bound to the substrate within the substrate plane, the volume loss occurs entirely perpendicular to the substrate, leading to "squishing" of the pores into increasingly anisotropic geometries (Fig. 4B(ii)).[99]

(iii) *Binary and more complex assemblies.* The simultaneous assembly of colloids with multiple sizes can result in the formation of binary and multinary crystal structures provided that the diameter of the small particles is chosen in a way that they can be accommodated in the interstitial sites of the crystal formed by the large particles.[87] A size mismatch, however, will result in disordered crystal structures.[4,82] Additionally, the porous materials of an inverse opal can be backfilled by smaller colloidal particles (Fig. 4B(iii)), producing more complex materials with higher porosity and choice of materials.[88,140]

(iv) *Crack formation and homogeneity.* The formation of cracks is generally unwanted and results from various origins. One major source of cracking is volume loss and stress during

drying of a colloidal crystal.[129] In this case, cracking can be reduced by addition of filler materials to the assembly solution,[59] assembly on elastic substrates,[141] or use of low surface energy-substrates.[141] Cracks can also form due to chemical effects, for example crystallization of the matrix material, or polycondensation of sol–gel precursors.[99]

*(C) Hierarchical patterns.* We define hierarchical superstructures broadly as colloidal assembly structures with periodicities at multiple length scales. Confining the assembled structure to a desired region of a substrate or device can be important,[142–144] and this hierarchy can lead to more complex properties, for example by introducing light–matter interactions occurring at different length scales[100] or by creating pixelated structures.[145,146] Hierarchical structures can be produced from 2D and 3D assemblies by a multitude of approaches, which have been discussed in great detail recently.[54,55] Very generally, common strategies to create hierarchical structures from colloidal assemblies involve patterning from the top down, or assembling into patterns from the bottom up.

*(i) Top-down patterning.* A desired superstructure is imposed on a pre-assembled colloidal crystal using classical top-down fabrication methods such as photolithography[100,145,147] (Fig. 4C(i)), microcontact printing,[146] or imprinting.[148] Alternatively, colloidal dispersions can be printed onto desired parts of the substrate using inkjet printing (Fig. 4C(iii)).[102,144]

*(ii) Bottom–up assembly.* With convective assembly, the colloidal crystal will grow directly around any surface features present on a pre-patterned substrate.[149–152] The assembly conditions themselves are precisely adjusted to create superstructures, for example stripe patterns can form in a convective assembly process.[153,154] Alternatively, a preferred site for the colloidal assembly can be created *via* assembly on a substrate that is patterned either physically (topographically)[55,101,149] (Fig. 4C(ii)) or chemically (wetting contrast, differences in adhesion).[55,155]

*(D) Superparticles.* We define superparticles as dispersible particles on the 10–1000 μm scale that are comprised of colloids in their internal structure. Whereas the classical hierarchical structures introduced above create multiple periodicities on a substrate, for a superparticle, the hierarchical element exists as a powder or in a dispersed state. The assembly of such structures generally requires an element of confinement, in which the colloids organize within the hierarchical superstructure. This confining element can be realized in various fashions.

*(i) Release from substrate.* A colloidal crystal is assembled on a substrate, patterned into a desired shape, and released to form dispersed elements (Fig. 4D(i)).[103]

*(ii) Removal from confined assembly.* Colloidal particles are assembled in a desired confinement and released *via* selective removal of the confining architecture. The process is exemplarily shown for a helical colloidal crystal assembled in the confinement of a silicon tube (Fig. 4D(ii)).[104]

*(iii) Confinement in emulsion droplets.* A colloidal dispersion is confined to an emulsion droplet and left to evaporate, leading to the assembly of micron-sized spherical colloidal crystals (Fig. 4D(iii)).[105,156–158]

**Scalability.** One of the great advantages of colloidal self-assembly is the potential to marry an inexpensive and parallel fabrication process with the high resolution features necessary for the plethora of applications discussed below. For any real world application, these fabrication processes need to be scalable to macroscopic dimensions without compromising the properties. While many assembly processes easily achieve very high order and beautiful features over small areas (as observed in electron micrographs), methodologies capable of producing structures over macroscopic areas with similar fidelity are extremely important. Here we highlight potential possibilities for self-assembly-based fabrication techniques to be scaled up.

High quality colloidal monolayers can be assembled over extended areas at an air/water interface followed by transfer to the target substrate. Using a Langmuir trough, this process easily yields wafer-scale colloidal assemblies in high quality (Fig. 5A and B).[115]

There are several scalable methods for making three-dimensional colloidal structures. Three-dimensional colloidal assemblies over large areas can be produced, for example *via* spin-coating processes. Though the presence of shear forces can be detrimental to the order, with a proper choice of colloidal particles, polymerizable matrix material, and a precisely controlled coating protocol, the fabrication of wafer-scale opals and inverse opals can be achieved (Fig. 5C and D).[109,159] Melt extrusion of core–shell colloidal particles is another process that yields colloidal crystals over macroscopic dimensions in an industrial extrusion process. The particles used in this process consist of a hard core and a shell with a low glass transition temperature and are applied in the process as a powder without any solvent. At elevated temperatures, the shell softens, leading to melting of the powder. This colloid melt can then be extruded and sheared into a thin film. The shear forces induce ordering of the particles and upon cooling, a large area colloidal crystal results (Fig. 5E).[135,136] The shell can further be crosslinked, producing elastomeric colloidal crystals with strain-responsive structural color (Fig. 5F).[160] Finally, superparticles can be prepared in a microfluidic setup, allowing a continuous flow production of self-assembled materials with high fidelity (Fig. 5G and H).[105,161]

The composition, order, and assembly of colloidal particles creates a rich variety of structures. Improving the control over cracking, large-scale synthesis, and hierarchical elements will lead to advances in achievable structures, which will then influence how they will be used. We next turn to how one can take advantage of these various structures in several application areas.

# 3. Optical applications

In nature, colloidal particles have been used to change the visual appearance of various organisms in several ways, including by providing additional scattering,[12] allowing for angle-independent

This journal is © The Royal Society of Chemistry 2016

*Chem. Soc. Rev.*, 2016, **45**, 281–322 | 287
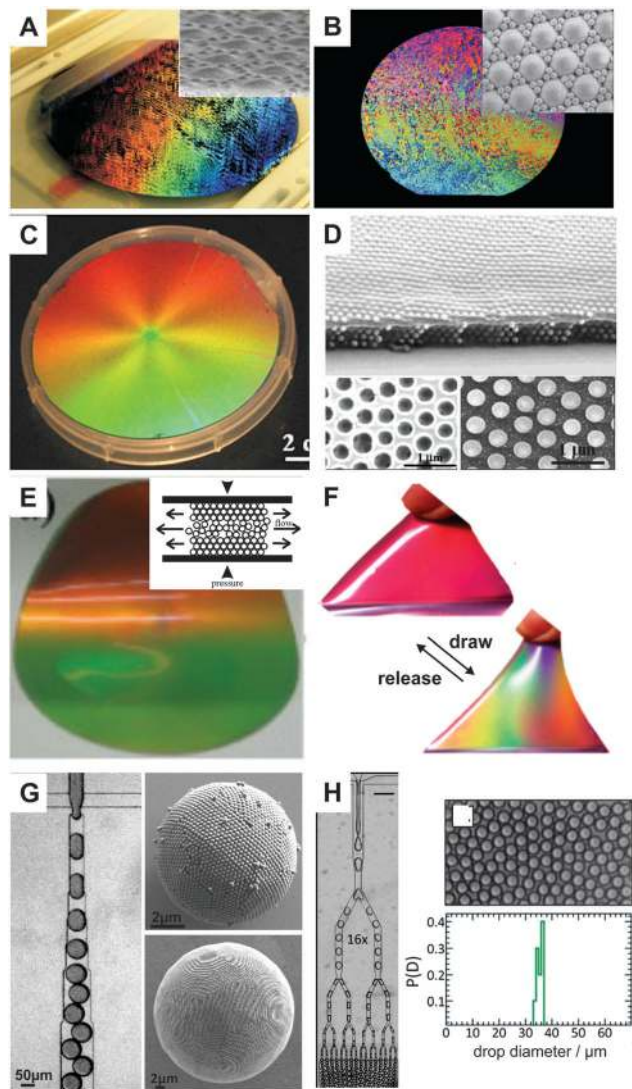
**Fig. 5** Colloidal self-assembly can yield surface patterns or structured materials with nanoscale dimensions in a parallel fabrication process over large areas. (A and B) Wafer scale colloidal monolayer deposition using a Langmuir trough.[115] Reproduced with permission from John Wiley and Sons, copyright 2011. (C and D) Wafer scale processing of opals *via* spin-coating.[109,159] Reproduced with permission from AIP publishing LLC (copyright 2006) and the American Chemical Society (copyright 2004). (E and F) Melt extrusion of core–shell particles can fabricate elastomeric, mechanically stable opals over large areas.[135,136,160] Reproduced with permission from John Wiley and Sons (copyright 2008), Elsevier (copyright 2003), and the American Chemical Society (copyright 2013). (G and H) Droplet-based microfluidics can be used to prepare spherical superparticles in a continuous-flow method[105] (reproduced with permission from the National Academy of Sciences, copyright 2015), and (H) the throughput can be increased by parallelization while maintaining monodispersity[161] (reproduced with permission from the Royal Society of Chemistry, copyright 2011).

structural color,[4] or providing bright, ordered structural color.[6] Colloids are useful in natural and biomimetic structural color applications because they have sizes on the same length scale as the wavelength of visible light, such that one can tune the optical properties of materials created from colloids by varying the size of the colloidal buildings blocks or the dielectric

constant of the material. Multi-step, hierarchical fabrication methods further enable additional optical properties occurring at larger dimensions such as grating effects and angular reflection properties. Structurally colored materials are increasingly sought for a wide range of applications, including high reflectivity mirrors, anti-reflective coatings, and optical fibers, as well as color elements for paint, cosmetics, decoration, or display technologies, and colloids are often used to template the photonic materials that enable these technologies due to their ease of fabrication and versatility. In particular, colloids can be assembled into structures with periodicity in all three spatial dimensions on the same order as the wavelength of visible light, forming 3D photonic crystals. By changing the material composition of these 3D photonic crystals—whether by using absorbing additives, responsive materials, or flexible materials—a variety of optical effects can be created. Fig. 6 schematically illustrates examples of different material parameters that can be tuned to modify the photonic properties of CBPM, with the resulting reflection spectra shown as insets. It should be noted that, although direct opals are shown in the schematics, the optical effects apply in the same way to inverse (templated) structures.

In addition to tailoring the properties of the individual colloids to tune the optical properties of CBPM, the assembly of colloidal particles can also be varied in several ways to alter the angle-dependence of the structural color (Fig. 7). Patterning the CBPM can enable more complicated security printing or display applications by allowing for more complex optical materials to be created, such as diffraction gratings (Fig. 7B). Changing the degree of order of the structure can drastically reduce the angle dependence of a structurally colored material, allowing for a much more angle-independent structural color (Fig. 7C). Assembling the opal structures further into dispersible particles either by top-down (*i.e.* grinding) or bottom-up (*i.e.* microfluidics) methods is an alternate method of changing the angle-dependent properties (Fig. 7D and E).

There are several parameters that can be used to tune the optical properties of colloidal crystals and derivatives thereof. The location of the Bragg peak in a photonic structure can be tuned in several ways as can be seen in the well-known Bragg–Snell equation (assuming a close-packed 111 lattice):

$$\lambda = \sqrt{\frac{8}{3}} D \sqrt{(\phi_1 n_1 + \phi_2 n_2)^2 - \sin^2\theta}, \qquad (1)$$

where $\lambda$ is the location of the Bragg peak of the structure, $D$ is the diameter of the colloids used in the HCP structure, $\phi_{1,2}$ and $n_{1,2}$ are the volume filling fractions and refractive indices of the constituent materials (colloids and air for direct opals or voids and matrix for indirect opals), and $\theta$ is the incidence angle measured from the surface normal. Note that while the parameters in eqn (1) can be used to modify the photonic stopband, the location of the photonic peak of the structure is not the only parameter that affects the appearance of the material. The bandwidth of the peak, the presence of additional orders, and the amount of scattering in the structure can also strongly influence the macroscopic appearance of the material. It should also be
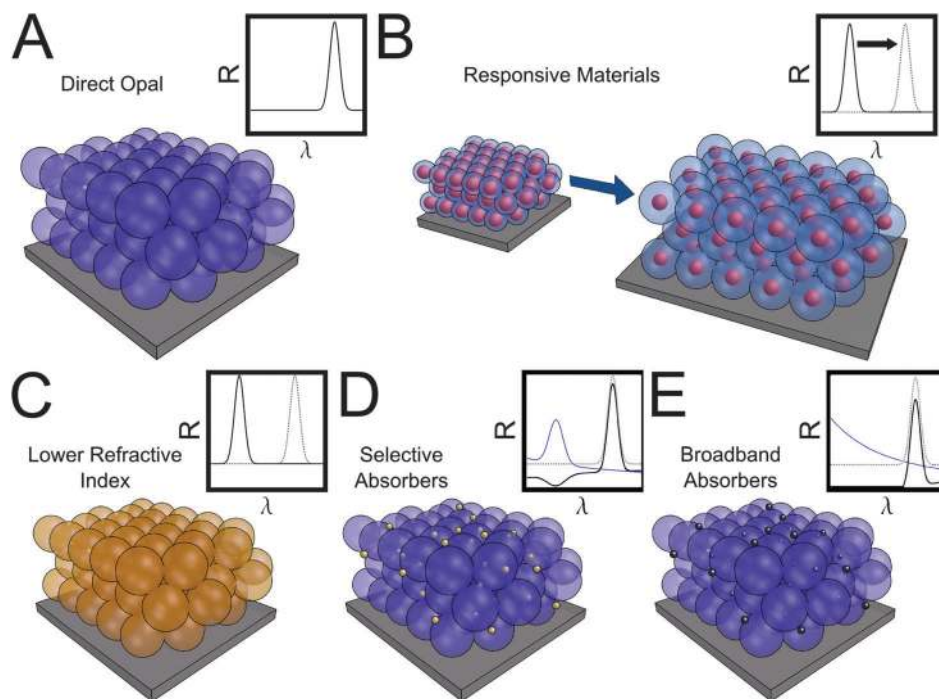
Fig. 6 Schematic of the influence of materials properties on the photonic peak of an opal. (A) A direct opal. (B and C) Direct opals formed from different types of colloids: (B) core–shell colloids, which can change size (and color) in response to a stimulus, and (C) colloids made of a material with a lower refractive index than in (A), resulting in a blue shifted spectrum. (D and E) Direct opals with (D) selective and (E) broadband absorbers. Insets show schematics of the reflected Bragg peak of the structure (black line, A–E), the reflected Bragg peak of the reference structure shown in part A (gray line, B–E), and the absorption spectra of the absorbers added to the material (blue line, D and E).
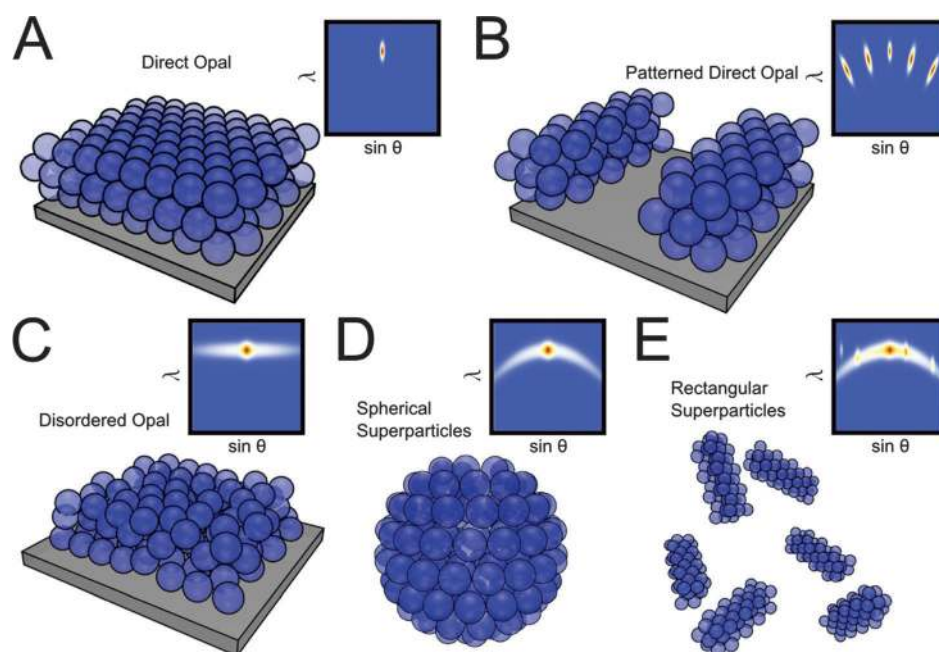


Fig. 7 Schematic of various methods for changing the angular dispersion of structural color in CBPM. (A) A direct opal. (B–E) Direct opals in various geometries: (B) patterned, (C) disordered, and (D and E) assembled in confinement—both (D) spherical and (E) rectangular. Insets show schematics of the reflected spectra for various detection angles, assuming normal incidence illumination.

noted that this equation ignores the effects of color saturation that can be modified by changing the number of layers in the structure or adding in absorptive elements. Additionally, this equation assumes a close-packed, ordered lattice; changing either of these properties also affects the optical properties of the material.

Overall, several parameters of the CBPM can be varied combinatorially to tune the optical appearance of hierarchical porous colloidal materials. The position of the Bragg peak can be controlled by the periodicity of the structure, the refractive index of the constituent materials, the presence or absence of absorption in the material, and the number of periods of the structure. Other properties of the material can affect the angular dispersion of the structural color, such as the degree of order of the structure or the inclusion of hierarchical geometries in the structure (Fig. 7). Below, we discuss in detail how these multi-faceted approaches can lead to a diversity of advanced optical behaviors across a broad range of applications.

### 3.1 Factors affecting optical applications

**Composition and additives.** Structural colors are not suscep-tible to photobleaching, so there is a large drive in the field to generate rich and varied colors for use as photonic pigments for paints and cosmetics. Historically, many different types of thin films of opals, inverse opals, and other colloid-derived materi-als have been used for their photonic properties.[82,162] Since scattering can greatly reduce the saturation of a photonic color, adding absorbing elements to the matrix can enhance the color of the structure. Fig. 8A shows examples of different structural colors that can be created from powderized inverse opal films.

More recently, core–shell colloids (typically silica core with polymeric shell) have been used to generate films of opal or inverse opal photonic crystals on different substrates[163,164] using organic shell components that can be annealed to enhance adhesion to the substrate or increase the mechanical durability of the film. Currently, the production of imperfect structures leads to non-negligible scattering that desaturates any structural color produced. Through the incorporation of broad spectrum absorbers[22,60,165] or plasmonic absorbers,[61,103,105,166] this scatter-ing can be reduced, although in the case of the broad spectrum absorbers the photonic peak intensity is also reduced. For example, Stellar's jays have blue feathers due to melanin coupled with disordered colloidal particles.[5] These additives purify the color and enable pigment and coating applications to access a broader color space than would otherwise be possible.

By using responsive materials as the matrix, reversibly tun-able colors can be achieved. The color shift of such materials is caused by a change in either the periodicity of the structure or the refractive index of its constituent materials. For security materials, optical switches, or dynamic display applications, it is important to be able to reversibly switch the structural color of CBPM either in an on/off configuration or by a measurable shift in the photonic stopband location. These responsive CBPM can also be used as sensors, as discussed in more detail below.
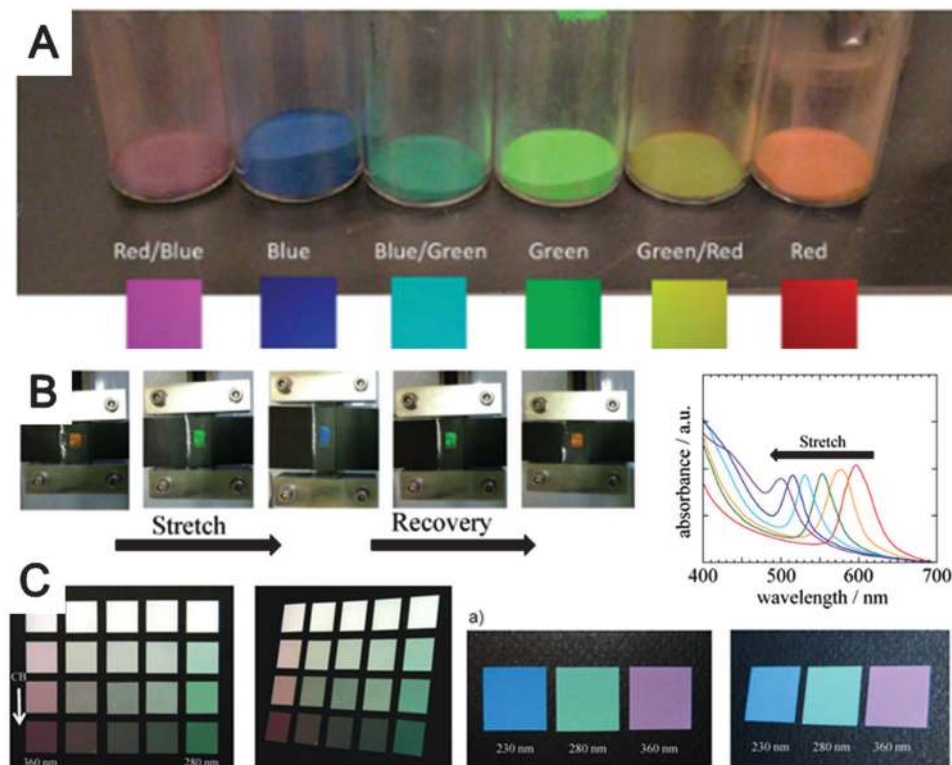


Fig. 8 Structural color created from colloidal photonic crystals. (A) Silica inverse opal powders with various pore sizes (red, 360 nm; green, 336 nm; blue 288 nm; other colors are 1 : 1 mixes of these) with mixed RGB reference images.[22] Reproduced with permission from John Wiley and Sons, copyright 2014. (B) Images of a stretched colloidal crystal elastomer and absorbance spectra showing the position of the Bragg peak for different strain values.[172] Reproduced with permission from the American Chemical Society, copyright 2013. (C) Disordered opal structure generated by spray coating, showing: left, color change by adding different amounts of carbon black to mixtures of two different colloid sizes; right, different colors for different sizes of colloids.[180] Reproduced with permission from John Wiley and Sons, copyright 2013.

There are several mechanisms that can be used to enable this switching, including the incorporation of magnetic particles to switch between ordered and disordered structures,[167–170] the use of elastomeric materials to allow change in the periodicity of the structure upon application of strain,[171–174] the inclusion of light-responsive moieties to change the average refractive index in the material,[24,175] and the implementation of redox-sensitive materials[176] and thermo-responsive materials[24,174,177,178] to change the lattice parameter typically by swelling and deswelling. An example of an elastomeric stretch-tunable structural color can be seen in Fig. 8B, where the periodicity changes upon stretching due to the Poisson ratio of the elastomeric material, causing a reversible blue-shift in the photonic peak of the opal structure. Photonic crystals like these can also be used as the gain media for colloidal crystal lasers as discussed in detail in a recent review.[179]

**Disorder.** While typically order is necessary for photonic structures, disordered colloidal structures—which still exhibit structural coloration—have also been studied.[4,82,180–182] For many color applications, the iridescent structural color of photonic crystal materials is undesirable. Nature has solved this problem by incorporating disorder into its photonic structures in order to increase their angular visibility, for example in the feather shown in Fig. 1A(i and ii)1.[3,5] Similarly, disorder introduced into CBPM can lead to angle-independent structural colors.[180–185] An example of such angle independence can be seen in Fig. 8C. It should be noted that there is a blue tinge to the colors that can be produced using this method. This additional blue coloration is caused by the wavelength-dependent scattering from the photonic materials and may be undesirable for the creation of longer wavelength colors. In order to create high-saturation structural colors, this scattering must be reduced either by incorporating selective absorbers as mentioned above or by creating defect-free materials.[181]

**Monolayers.** In addition to 3D photonic crystals, 2D colloidal monolayers can also be tuned to create many different optical materials and properties. For example, the monolayer can be used for shadow deposition to generate different shapes of deposited materials,[97,120,124,186] used as an etch mask to generate high aspect ratio structures with high order,[166,187,188] inverted/textured to create antireflective coatings for reducing the amount of reflected light from a substrate surface,[95] or deformed to generate structurally colored patterns on a substrate.[112] Interesting coupling effects can be observed between the photonic modes of an opal and the plasmonic modes of thin metals deposited on top of the crystal.[189–193]

Colloids can also be used for antireflective coating applications.[85] In particular, colloidal monolayers have been used to create porous, graded-index materials with low reflectivity by, for example, plasma etching of colloidal monolayers,[194] inverting the monolayer,[95] or using the monolayer as an etching mask to generate pillars.[166,187,195] To reduce the reflection from the top surface of solar cells, many methods are used to generate porous materials with the proper optical thickness and effective index for optimal transmission. A recent perspective discusses many of these methods.[196] Specifically, colloidal materials can generate high porosity, creating the ability to reach the $\sqrt{n}$ effective

refractive index required for perfect transmission at the desired wavelength.[197]

There are several ways to generate the graded effective refractive index profile that causes the antireflective effect of these coatings. Very small colloids (<30 nm), such as organically modified silica (ORMOSIL) particles, can be used to generate uniform antireflective coatings, but typically require the addition of stabilizing elements to make robust films.[198–200] Larger colloids can be used, with or without other materials, to generate hierarchically structured materials with very high transmission values.[188,201,202] Fig. 9 shows an example of such a structure
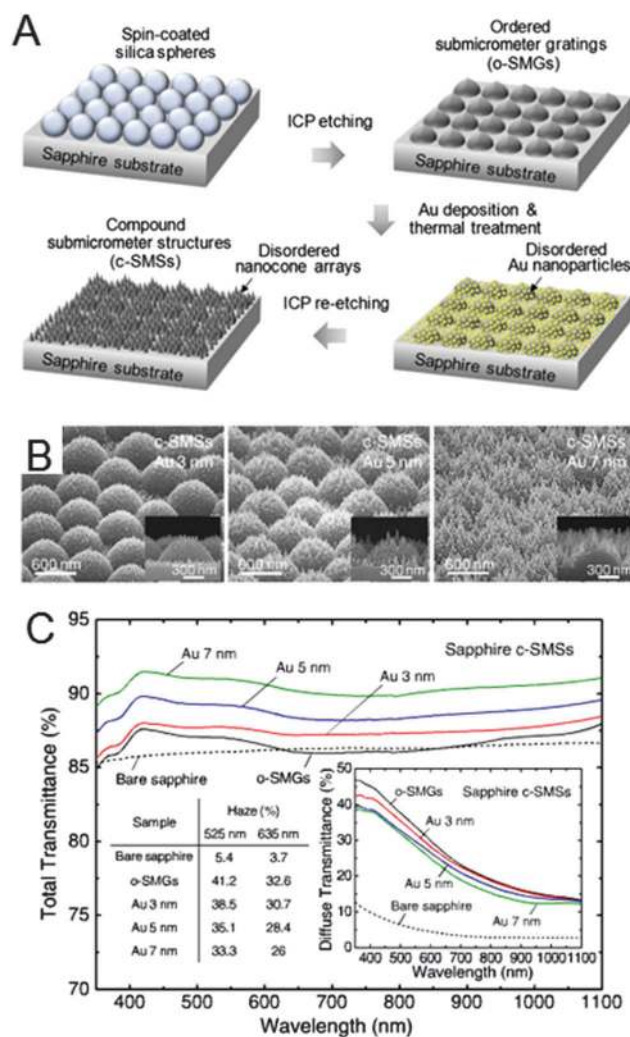


Fig. 9 Antireflective coating based on hierarchical colloidal lithography. (A) Schematic representation of the fabrication of compound submicrometer structures (c-SMSs) and ordered submicrometer gratings (o-SMGs) for use as antireflective coatings. A layer of colloids is first etched to create o-SMG, which is coated with gold and thermally treated to generate nanoparticles on the surface, which is then etched again to generate a c-SMS. (B) Tilted-angle and side-view (inset) SEM images of hierarchical nanostructure antireflective coatings using Au film thicknesses of 3, 5, and 7 nm. (C) Transmittance spectra for the structures shown in A along with the transmittance spectrum for the bare structure (without the additional gold etching step, black line, o-SMGs). Insets show the diffuse transmittance spectra and haze ratio values for two different wavelengths for all samples.[188] Reproduced with permission from OSA publishing, copyright 2013.

created by using a monolayer of colloids as an etch mask to make a grating structure on which a disordered array of gold nanoparticles is created. This array of nanoparticles is then etched to create a hierarchical structure with better antireflective properties than the original structure. The transmittance was found to increase after the surface treatment (Fig. 9C).

Colloidal monolayers can even generate structural color if surface diffraction modes are used as the source of the structural color.[112] This type of material has a much more angle-dependent structural color as compared to fully three-dimensional photonic crystals due to the nature of the surface diffraction.

**Superparticles.** Another way to create angle-independent structural color is *via* modification of the local geometry. By using spherical or hemispherical assemblies of colloids, all viewing directions are normal to some portion of the superparticles. Such assemblies are typically created *via* evaporation of a solvent from a droplet containing colloids. These droplets can be created *via* microfluidics[105,203] or ink-jet printing.[204,205] For more information, a recent review covers many of the aspects of these types of photonic crystals.[158] Fig. 10 shows inkjet-printed photonic hemispheres (Fig. 10A–C) and arrays of buckled-sphere photonic superparticles embedded in a flexible material (Fig. 10D), both of which show angle-independent color. It should be noted that the structural color of these photonic superparticles is only independent of viewing angle in a diffusely lit environment due to the near-normal incidence peaks being brighter than the blue-shifted, higher incidence angle peaks. When viewing the structures in transmission or at an oblique angle to a strong lighting source, different photonic or scattering colors can be seen.[105] The creation of disordered superparticles can also strongly reduce angular-dependence of the reflection color, similar to thin films of disordered colloids.[180,185] Also, when larger colloids are used, diffractive colors become dominant over the Bragg reflectance peak, leading to a much larger variation in color with viewing angle.[105,206]

Another geometry of dispersible photonic particles is created using fragments of inverse opal films, which can be grown directly into sacrificial channels[103] or ground from larger inverse opal samples[22,165] to create structural color "pigments" which can be dispersed in paint bases. Structures created in this way have a different visual appearance compared to dense layers of spherical photonic superparticles due to the obvious angle-dependence of the structural color. Since the particles are typically larger, individual domains can be seen by eye, creating a sparkle effect when changing the viewing and illumination conditions.[103]

**Hierarchy/patterning.** For display applications, the patterning of photonic materials of different stopbands into pixelated arrays is of great interest. Such patterning has historically been achieved *via* top-down processes such as photolithography[100,147,207] or microimprinting,[148] leading to static "pixels" of photonic crystals such as those shown in Fig. 11A. Such pixelation can be used to create near arbitrary patterns (images) from structural color materials, provided the desired colors can be generated. An example of an RGB pixelated array can be seen in Fig. 11B and C. If magnetic materials are used, architectures closer to an actual display are created[170] in which the color of each pixel can
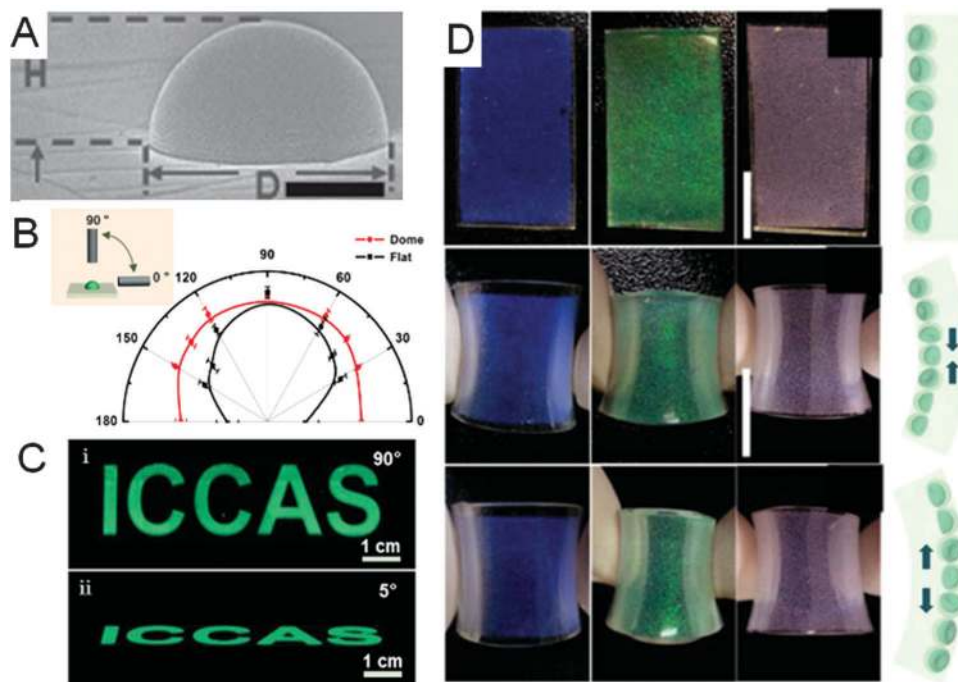


Fig. 10 Colloidal crystal superparticles with little angle-dependence of color. (A–C) Ink-jet printed hemispherical colloidal superparticles. (A) SEM image of a dome (scale bar: 5 μm). (B) Normalized fluorescent intensity of domes (red) and dots (black) for different detection angles. (C) Top and side view images of a pattern of domes showing a wide angular visibility of the color.[205] Reproduced with permission from John Wiley and Sons, copyright 2014. (D) 2.8 cm × 1.5 cm flexible buckled-sphere colloidal superparticle films showing lack of angle dependence of the structural color upon compression and stretching. Colloid sizes: 170 nm (blue), 200 nm (green), 250 nm (red).[203] Reproduced with permission from the Royal Society of Chemistry, copyright 2015.

292 | *Chem. Soc. Rev.*, 2016, **45**, 281–322

This journal is © The Royal Society of Chemistry 2016
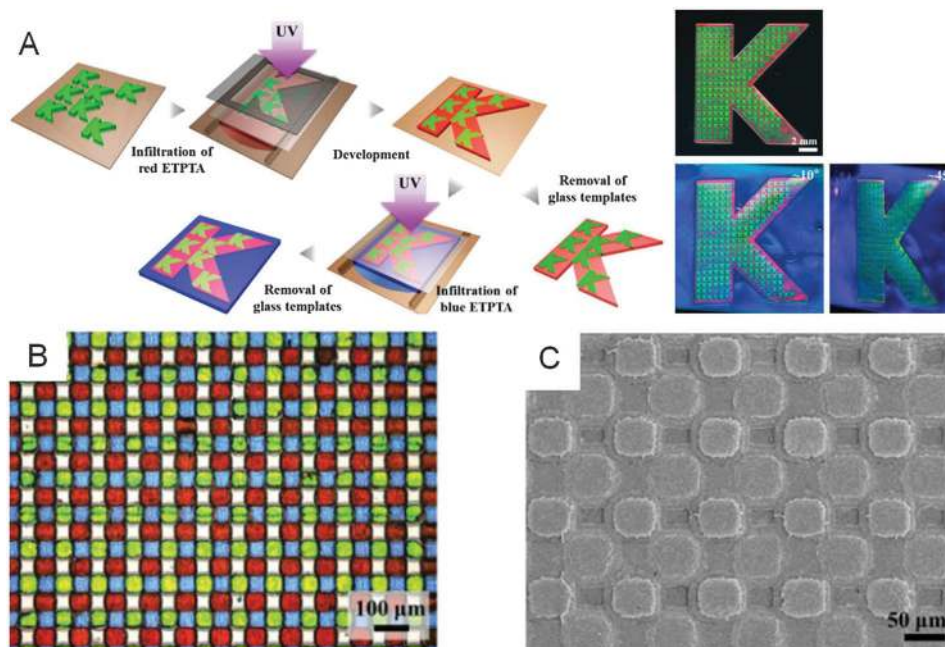
**Fig. 11** Lithographic patterning of colloidal photonic crystals. (A) Left, schematic illustration of patterning method used to make multi-colored colloidal crystals. Right, optical images of films with two and three colors under different viewing angles.[144] Reproduced with permission from the American Chemical Society, copyright 2013. (B and C) Hierarchical "pixelated" inverse opal arrays made from SU-8: (B) optical microscopic image of the hierarchical inverse opal, and (C) SEM of the structure.[207] Reproduced with permission from John Wiley and Sons, copyright 2014.

be reversibly changed in an on/off state. The pixels, in this case, consist of magnetic Janus superparticles with colloids comprising half of the sphere to generate a photonic peak that is visible only when the superparticles are in the correct orientation. Since the particles are magnetic, the orientation of each "pixel" can be reversibly switched allowing for images to be created.

### 3.2 Perspective

CBPM provide a platform for the development of photonic crystal materials due to their relative ease of fabrication, controlled order, and the wide variety of materials from which they can be made. For macroscopic (*i.e.* wafer-scale or larger) 3D photonic crystals, competing methods such as electron beam lithography and two-photon lithography methods are limited to small sizes, and they require long processing times to create the desired photonic structures due to their serial nature. 1D Bragg stacks and 2D nanowire forest photonic crystals have applications that compete with opal and inverse opal photonic crystals, but they typically lack the benefits of self-assembled systems such as low cost and facile fabrication. Still, crystal lattice defects lead to scattering that greatly weakens the signal-to-noise ratio of the optical response in self-assembled CBPM; it remains a great challenge to increase the order of such materials or to allow for controlled disorder to generate high-chromaticity angle-dependent or angle-independent structural colors.

Additionally, the ability of hierarchical CBPM to be made *via* top-down lithographic methods or assembly in confinement allows a greater variety of optical properties to be achieved. Research is still needed into creating CBPM with better long-range order and using colloids with higher refractive index

materials in order to achieve a full photonic bandgap.[208] Longer-range order and higher refractive indices will generate stronger photonic peaks with less scattering noise, reducing the need to integrate absorption into the material. Increases in the sophistication of CBPM with regard to the dynamic coloration *via* shifting the photonic stopband or moving the photonic crystal out of view could lead to electronic ink displays with full color displays in the future and advanced security features in anti-counterfeit applications.

## 4. Wetting applications

The leaves of many plants, water strider legs, duck feathers, butterfly wings, and the coat of the Stenocara beetle in the Namib desert are examples of natures' sophisticated solutions to keeping surfaces clean and dry.[209] Studying these organisms' wetting properties has led to countless approaches to create multifunctional materials with tunable wettability for applications ranging from self-cleaning repellent surfaces to antifogging coatings. Colloids offer a unique platform to understand and control the wetting of liquids on surfaces for various applications because they can systematically modify multiple parameters of the surface with simple methods.

A recent review by Yan *et al.* provides a thorough discussion of specific theoretical models used to describe wetting behavior.[209] There are generally three parameters fundamental to achieving a desired surface wetting state: surface roughness, re-entrant geometry of the roughness features, and surface energy. Colloidal particles assembled on a substrate allow for the direct

control of all three of these parameters. The size of the colloids, material used (*i.e.*, polymers, metals, or metal oxides), surface functionality of the colloids, spacing between particles, filling fraction, and order of the assembly can be used to adjust the three parameters and therefore the surface wetting state of liquids. Due to colloids' large surface area to volume ratio, they can easily be used to generate surface roughness on a variety of different substrates. Depending on the material composition, the surface chemistry, and the final architecture of the colloidal particles, liquids either assume a fully wetted state or a non-wetting state, allowing for ease of use in applications that require either of these wetting behaviors.

Here, we discuss the ordered and disordered colloidal assemblies that are used to study wetting phenomena. In addition to using colloidal assemblies for creating a particular surface wetting property, inverse colloidal assemblies have also been used to study liquid transport as a function of local pore size and chemistry. These studies are particularly useful for membrane and sensing applications, and are related to the diffusion through the pores that is necessary for catalytic and

electrode applications. CBPM have also been used in other transport applications such as for cell culture,[210,211] for drug delivery,[212,213] and as membranes and filters,[214] applications we do not cover in this review.

### 4.1 Factors affecting wetting applications

**Surface roughness.** One of the obvious benefits of using colloidal particles for wetting applications is the inherent increase in surface roughness provided by both ordered and disordered assemblies. Models such as the Wenzel and Cassie–Baxter states are commonly used to predict the wetting state of a liquid on a surface. Both models recognize that the presence of surface roughness alters the contact angle of a liquid droplet when compared to a smooth surface with the same surface energy. Liquids infiltrate the structure in the Wenzel model,[218] as shown in Fig. 12A, and complete wetting in this state is beneficial in some instances such as when designing an anti-fogging coating. For example, water condensate spreads on a hydrophilic anti-fogging coating on glass containing roughness features instead of forming droplets as it does on an untreated
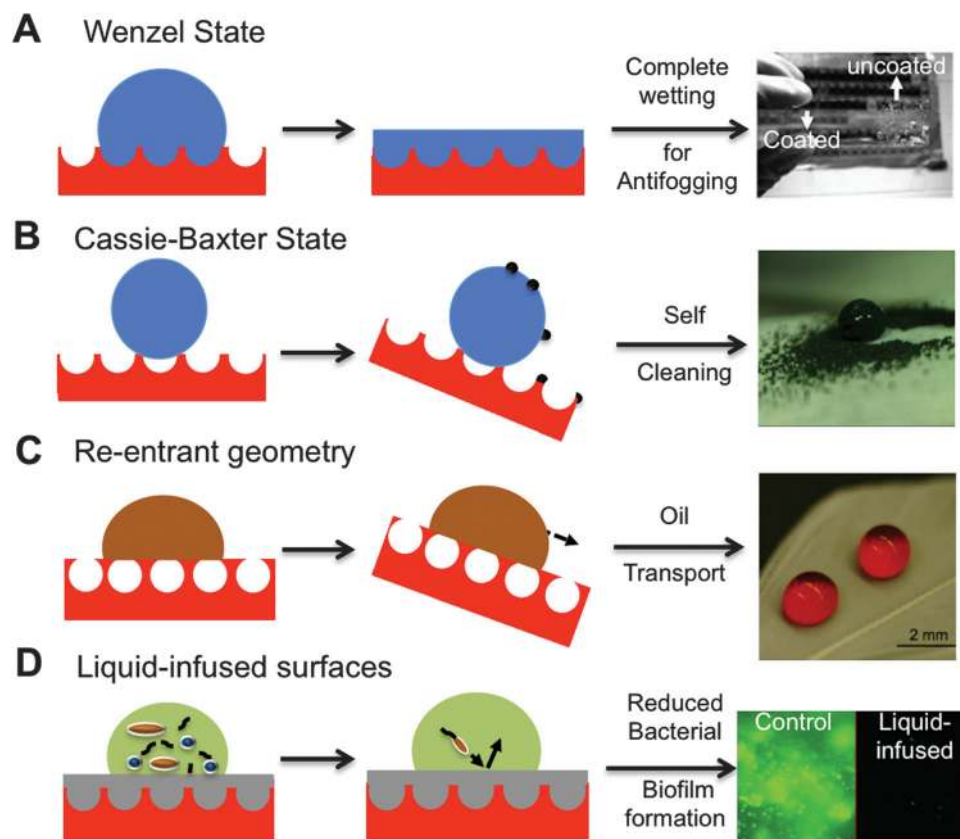


Fig. 12 Overview of different wetting states of liquids on surfaces and resulting macroscopic properties. (A) Wenzel state for antifogging coatings. The uncoated region of the glass slide shows droplet formation while the coated region appears transparent.[86] Reproduced with permission from the American Chemical Society, copyright 2006. (B) Cassie–Baxter state for superhydrophobic self-cleaning surfaces.[215] Reproduced with permission from the American Association for the Advancement of Science, copyright 2015. (C) Re-entrant geometry for superoleophobic surfaces, such as for oil transport. The red droplets are dyed rapeseed oil on a duck feather modified to be superoleophobic.[216] Reproduced with permission from the National Academy of Science, copyright 2008. (D) Liquid-infused surfaces capable of preventing bacterial attachment and thus preventing bacterial biofilms. The fluorescent control image indicates bacterial biofilm formation on a flat polytetrafluoroethylene substrate after incubation in bacterial culture, while the lack of fluorescence on the lubricant-infused roughened polytetrafluoroethylene surface indicates that the surface contains no bacteria after incubation.[217] Reproduced with permission from the National Academy of Science, copyright 2012.

flat glass substrate, decreasing light scattering and maintaining transparency (Fig. 12A).[86] However, such behavior is not suited for applications where repellency is desired, since it would result in liquid pinning, high contact angle hysteresis, and failure of the coating.

On the other hand, the Cassie–Baxter model, shown in Fig. 12B, describes the state where liquid repellency is attainable. The model suggests that liquid droplets can be supported by the composite air/solid interface of a rough surface to form apparent contact angles greater than 90° without wetting the air pockets within the rough surface.[219] An ideal Cassie–Baxter state results in minimal pinning and is suited for applications such as self-cleaning surfaces where liquid droplets are shed from the surface at low tilt angles, collecting solid particles within the droplets (Fig. 12B). By introducing roughness, the hydrophobicity (for Cassie–Baxter) or hydrophilicity (for Wenzel) of the surface chemistry can be enhanced.

In direct colloidal assemblies, the selected size of the particles and the spacing between them can be tuned, enabling precise control over the wetting state (Fig. 13A(i and ii)).
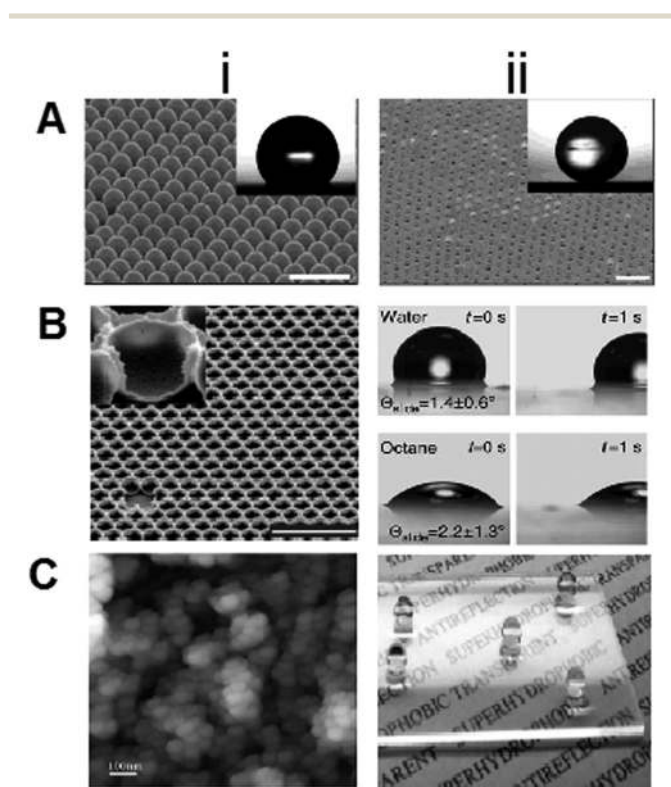


Fig. 13 Various types of roughness formed from CBPM. (A) Longer plasma treatment times etch away at close-packed polystyrene particles, increasing the interparticle spacing. This surface modification leads to increased surface roughness and therefore increased superhydrophobicity, as shown (i) before, and (ii) after plasma treatment.[23] Reproduced with permission from the American Chemical Society, copyright 2004. (B) Inverse colloidal monolayers infused with lubricant repel both low and high surface tension liquids such as octane and water. (i) SEM of structure; (ii) sliding angle of water and octane.[95] Reproduced with permission from Nature Publishing Group, copyright 2013. (C) Layer-by-layer assembly of silica nanoparticles creates superhydrophobic surfaces after modification with a fluorinated silane. (i) SEM of the structure; (ii) photograph demonstrating the resulting high contact angle.[85] Reproduced with permission from the American Chemical Society, copyright 2007.

Techniques such as reactive ion etching[220] or oxygen plasma treatment[23] can provide control over these parameters. The resulting topographies of the substrate surface, such as pillars and cones, support a specific wetting state.[122,221] By introducing the appropriate surface chemistry, a superhydrophilic or superhydrophobic state can be achieved. For example, surfaces after plasma etching are generally rendered superhydrophilic, where water wets the surface structures in a Wenzel state at an angle close to 0°. Conversely, functionalization with a hydrophobic fluoroalkylsilane renders the surface superhydrophobic, where water wets the surface in a metastable Cassie–Baxter state at an angle greater than 150° (Fig. 13A(ii)).[23]

The concave structures produced by inverse opal assemblies provide ideal rough substrates to satisfy the Wenzel or Cassie–Baxter state of wetting.[222–224] Inverse opals have been used to template soft materials to create superhydrophobicity;[225] however, the concave structures shown in Fig. 12A and B have not been used to create superoleophobic surfaces, which instead require a feature known as re-entrant geometry, shown in Fig. 12C and discussed below.

Surfaces that rely on the Cassie–Baxter wetting state for repellency often face some disadvantages, such as reduced stability at high pressures and the formation of pinning points for the liquid in the presence of defects. Another type of repellent surface circumvents these issues by using low surface energy lubricant oil infiltrated into a roughened surface (Fig. 12D).[95] Through capillary forces and matching chemistry between the oil and solid surface, the liquid forms a thermodynamically stable wetted state. A second immiscible liquid slides off the surface with ease. These liquid-infused surfaces repel both low and high surface tension liquids without the need for re-entrant geometries. They also do not fail under pressure, can be made optically transparent, and to a certain extent self heal after mechanical damage.[226–228] These omniphobic coatings not only repel complex liquids such as blood and crude oil, but they can also prevent bacterial biofilm formation, for example in catheters where patients are at risk for hospital-acquired infections.[217]

Inverse opals can be infiltrated with a lubricant to create these liquid-infused surfaces. For example, Vogel et al. templated silica using colloidal monolayers on a glass surface (Fig. 13B). Following fluorosilanization with a fluoroalkyl trichlorosilane, a fluorinated lubricant was infiltrated into the structure and was stably trapped within the inverse assembly such that a second immiscible liquid slid off the surface at tilt angles below 2°.[95] In this case, the surface roughness combined with the low surface energy functionalization is responsible for stably trapping the lubricant in a Wenzel state while the lubricant imparts repellency. The molecular-scale, dynamic nature of the liquid layer prevents organisms such as bacteria from forming contact points with the underlying solid structure, resulting in poor biofilm formation on these types of surfaces,[217] with the promise to create anti-bacterial surfaces. In addition, the regular, closed cell porosity of the inverse colloidal monolayer provides strong mechanical durability of the coating.[95]

Similar to ordered assemblies, disordered systems contain innate surface roughness that enhances the hydrophilic or

hydrophobic nature of the surface. Layer-by-layer assembly and spray deposition are commonly used techniques to cover a substrate with disordered colloids for superhydrophilic/phobic coatings (Fig. 13C).[229–231] Metal oxide colloids, especially silica, are typically used in layer-by-layer assemblies because they contain surface charges that can be employed for electrostatic binding to a substrate and can be readily functionalized after assembly. When the sizes of these metal oxide particles are below the wavelength of visible light, they form transparent coatings.[85,86] The particles can also be sintered to improve the mechanical robustness of the coating.[232] However, the sintering process may limit substrates to those that can withstand high temperature treatments. While the dry coatings without further modification are generally not omniphobic, disordered rough surfaces can be functionalized and infiltrated with a lubricant to form a liquid infused repellent coating capable of repelling both high- and low-surface-tension liquids on a variety of curved and other types of surfaces.[233]

**Re-entrant geometry.** In general, low-surface-tension liquids with contact angles much lower than 90° assume the Wenzel state as opposed to the Cassie–Baxter state. Therefore, it is very difficult to create surfaces that can repel low-surface tension liquids. Tuteja *et al.*[234] and Krupenkin *et al.*[235] discovered a way to create a highly non-wetting surface for low-surface-tension liquids using an additional parameter called re-entrant geometry.[234,235] Introducing geometry that contains an overhang, or re-entrant curvature, to the roughness features enables these low-surface-tension liquids to remain suspended rather than infiltrating the structures. If the overhang makes an angle smaller than 90° to the flat substrate, low-surface-tension liquids with a larger wetting angle than the overhang angle will de-wet from the structures,[77,216] as shown schematically in Fig. 12C. The overhang changes the angle the liquid makes with the roughness features, creating a convex meniscus shape. This convex meniscus changes the advancing force of the liquid upward against gravity, allowing a metastable Cassie–Baxter state to form. These surfaces are referred to as superoleophobic, and they are well suited for oil transport pipelines where oil repellency from the surface of the pipeline reduces the required pressure for transport and thus the energy costs associated with transport.

Re-entrant curvature is not easily fabricated and typically involves multiple process steps or hierarchical architectures to provide overhanging elements in the structure. Colloids can be used to build such elements, provided they are attached to a suitable support, such as in pillars created *via* plasma etching (Fig. 14A).[236] More robust superomniphobicity can be created from hierarchical assemblies: Deng *et al.* used candle soot to create a coating composed of 30–40 nm carbon particles, which were subsequently coated with a thin silica shell. Upon calcination, the carbon combusts, leaving behind a transparent superomniphobic mechanically robust coating (Fig. 14B).[237] A simple spray coating of metal oxide colloids combined with a perfluoroacrylic polymer emulsion or fluorosilane has recently been used to easily create superoleophobic coatings as well (Fig. 14C).[84,215,238] These methods are promising candidates for omniphobic coatings for applications where transparency is not a design criterion, such as for drag reduction in pipelines.
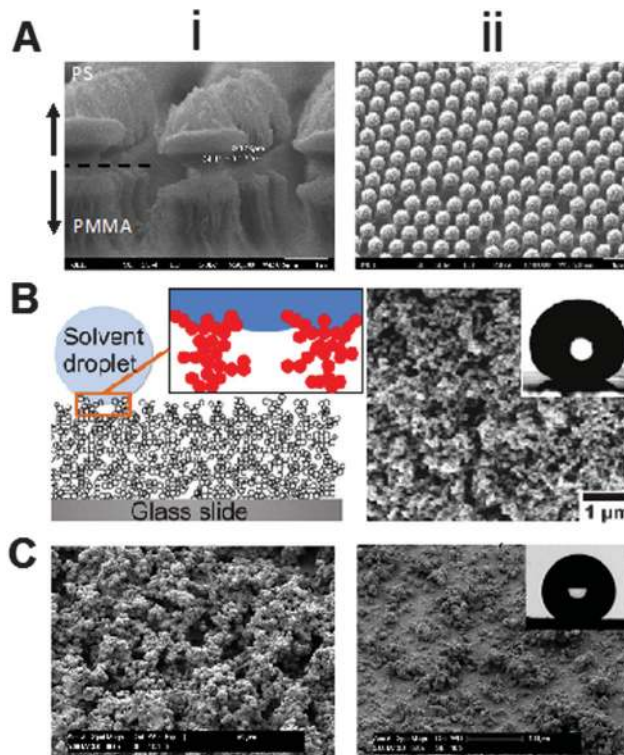


Fig. 14 Examples of re-entrant geometries created using ordered and disordered colloidal assemblies. (A) (i) Side view, and (ii) top view of re-entrant geometry created with plasma etching and colloidal lithography, where the mushroom caps are composed of polystyrene (PS) and the stems are composed of polymethylmethacrylate (PMMA).[236] Reproduced with permission from the American Chemical Society, copyright 2011. (B) A superamphiphobic coating created using hollow silica particles. (i) Schematic of re-entrant curvature supporting a low surface tension solvent droplet, and (ii) SEM image of the coating, with an inset of a hexadecane droplet on the surface (CA = 156°).[237] Reproduced with permission from the American Association for the Advancement of Sciences, copyright 2012. (C) An omniphobic coating: (i) SEM of ZnO particles sprayed with perfluoroacrylic polymer emulsion, and (ii) the resulting high oil contact angle.[238] Reproduced with permission from the American Chemical Society, copyright 2009.

Discussions of re-entrant curvature are usually made in the context of repelling low-surface-tension liquids. However, re-entrant curvature is also present within inverse opals and can guide the wettability and direction of wetting within the nanoporous structures. Interconnected pores in an inverse opal assembly meet at an angle referred to as the neck angle $\theta_N$ (Fig. 15A(ii)). A liquid droplet forms an angle $\theta_C$ with a flat substrate (Fig. 15A(i)), and this angle is determined by the surface energies of the liquid, solid surface, and liquid/solid interface. The same liquid will only wet an inverse opal structure composed of the same material if $\theta_C < \theta_N$, enabling one to define the wetting characteristics by adjusting the surface chemistry of the inverse opal pores.[77,78] Sintering an inverse opal assembly attached to a solid substrate results in anisotropy of the opals to varying degrees depending on the temperature used.[239] The pore anisotropy results in the ability to control the neck angle of the pores resulting in a difference between the in-plane and out-of-plane neck angles. Liquids can only infiltrate

296 | Chem. Soc. Rev., 2016, 45, 281–322

This journal is © The Royal Society of Chemistry 2016
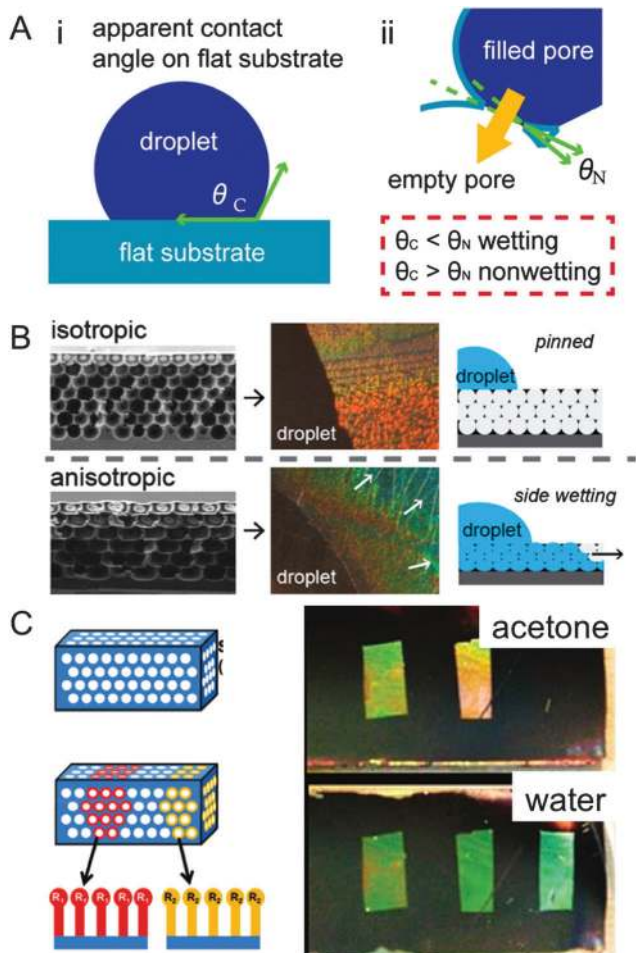
Fig. 15 Controlling bulk wettability in inverse opals. (A) Wetting conditions for inverse opals. (i) Liquids form a contact angle $\theta_C$ on a flat substrate. (ii) Two adjacent pores are separated by re-entrant geometry characterized by an angle, $\theta_N$. Liquids will infiltrate an inverse opal assembly of a given material composed of pores connected at some angle $\theta_N$ if $\theta_C < \theta_N$.[239] Reproduced with permission from the American Chemical Society, copyright 2014. (B) Inverse opals attached to a solid support are isotropic upon assembly, but after high temperature treatments they form anisotropic pores, causing liquids to wet only from the side.[239] Reproduced with permission from the American Chemical Society, copyright 2014. (C) Chemical patterning of an inverse opal structure leads to varying degrees of bulk wettability depending on the liquid used, the neck angle of the pore, and the chemistry of the pores.[78] Reproduced with permission from the American Chemical Society, copyright 2011.

and wet the structure if the contact angle of the liquid is below the neck angle of the pore, so the anisotropy in pore shape results in certain liquids only infiltrating within the plane (Fig. 15B).[239] This unique tunability of the neck angle of colloidal structures adds an extra parameter that can be used when designing coatings where directional liquid wetting may be desired.[240,241]

**Surface energy.** In addition to roughness, colloidal particles allow for easy control of surface functionality either by employing particles that possess a particular surface chemistry or by modifying the particles or templated structure after assembly. As mentioned above, roughness enhances the inherent surface chemistry of the surface (whether the surface is hydrophobic

or hydrophilic). The ease with which surface chemistry can be tuned lends itself to producing intricate wettability patterns on a single substrate. Because the contact angle (CA, or $\theta_C$) influences filling of inverse opal pores along with the structure (neck angle), surface chemistry can be used to adjust the contact angle and thus the wetting properties. Indeed, inverse opal assemblies have been patterned with varying chemical functional groups so that immersion of the substrate in a particular liquid will result in liquid infiltration only in select regions.[78] Fig. 15C shows an example of an inverse opal assembly that was functionalized with multiple distinct surface functionalities. Selective liquid infiltration will occur in this structure depending on the criteria discussed above and described in Fig. 15A. Clearly, both pore geometry and surface chemistry are important for bulk liquid wetting. These types of surfaces are useful for encryption or sensing applications, as discussed in more detail in the following section.

Chemical patterning techniques can also be used in liquid infused surfaces. After chemical patterning, infusion with a lubricant leads to lubricant spreading in all the regions in a metastable state. However, the addition of a second immiscible liquid displaces the lubricant in regions where it has no chemical affinity to the underlying solid structure leading to a clear spatial confinement of the test liquid.[95]

The surface energy can also be controlled based on the material itself. Assembly conditions such as temperature[242] and pH[243] can determine the final wetting state of the surface. For example, particles with a hydrophobic core of polystyrene (PS) and a hydrophilic shell of poly($n$-butyl acrylate–acrylic acid) (PBA–PAA) assembled at temperatures close to 20 °C have been shown to form a superhydrophilic surface, while an assembly temperature of 90 °C produces a superhydrophobic film.[242] This has been attributed to phase separation of the polymer segments at varying assembly temperatures.[244] Wetting states can also be modulated using stimuli-responsive materials such as polypyrrole[245] and azobenzene[244] incorporated into the colloidal assemblies. This type of selective wettability is useful for applications such as window treatments where environmental triggers such as heat or UV from sunlight can modulate whether surfaces repel liquids or are wetted by them.

### 4.2 Perspective

Colloids are capable of creating a diverse array of coatings despite their simplicity. These coatings can be made transparent using subwavelength colloids, while the use of larger colloidal particles can result in "colored" wetting behaviors. Creating the underlying geometry or surface roughness to support non-wetting states for various liquids can be achieved using conventional fabrication methods such as photolithography, electrochemical deposition, electrospinning, etc.;[209] however, these methods often require expensive equipment, time consuming processes, limited substrate choice, and a feature size limit. CBPM have the potential to overcome these drawbacks: they do not generally require expensive instruments, they allow diverse materials and topographies to be coated, and they are inherently very small in dimension.

A one-size-fits-all coating method is not possible due to the abundance of wetting applications that exist with competing demands.

This journal is © The Royal Society of Chemistry 2016

Chem. Soc. Rev., 2016, 45, 281–322 | 297

Therefore, choosing a method that satisfies the design criteria for a specific application is critical. For example, an anti-fogging coating must be transparent, but a self-cleaning surface may not need to be. For most of the applications that require repellency, mechanical robustness is one of the most important criteria. Improvements have been made recently in this regard. The honeycomb inverse opal assemblies on glass are particularly robust, but these structures don't easily coat variable geometries or large surface areas without the presence of defects.[95] Disordered colloidal assemblies can be sintered to improve mechanical strength.[232] However, a colloid-based coating that can survive the wear and tear of daily use or hostile cleaning procedures remains elusive and could be the subject of future research.

Ordered colloidal assemblies are extremely useful for the precise control of structures on a wide variety of substrates. In addition to being low cost and easy to fabricate, the resulting assemblies are straightforward to model, and therefore it is possible to understand, predict, and systematically tailor the wetting behavior on these surfaces. Researchers have made significant strides to overcome the challenges of creating these coatings on multiple substrates and shapes, making progress to extend their use to applications such as anti-fogging, anti-icing, self-cleaning, or anti-microbial surfaces that was previously not possible. From an industrial standpoint, the techniques employed to create disordered coatings for selective wetting are far more scalable than ordered colloidal coatings. Coatings spanning large areas on windows and long pipelines are possible.

These coatings can be transparent, can cover different materials, and can uniformly coat varying geometries. They can also be multi-functional and combine both wetting and sensing applications.

## 5. Sensing applications

The demand for reliable, simple, and inexpensive sensors stems from the need to monitor and record a broad range of conditions and analytes, including light intensity, temperature, pressure, pH, and humidity, as well as the presence of various chemicals and microorganisms in water, in food, and *in vivo*. As described in the Optics section above, CBPM with lattice dimensions on the length-scale of visible light can form a photonic crystal with structural color. This structural color allows them to be used as colorimetric sensors. In addition to photonic properties, CBPM can also have unique phononic properties that are useful for sensing applications.[246] Colorimetric sensors are the most common type of CBPM sensors, and thus they are the focus of this part of the review.

A distinct optical response of a CBPM sensor can originate from dynamic variation of its different components, as shown in Fig. 16, namely from changes in the lattice constant, each constituent's refractive index, or additional components' spectral characteristics. A number of existing reviews cover various aspects of CBPM sensors, such as materials,[247] fabrication,[248–250] degree of order,[251] and specific applications.[57,252] Here, we
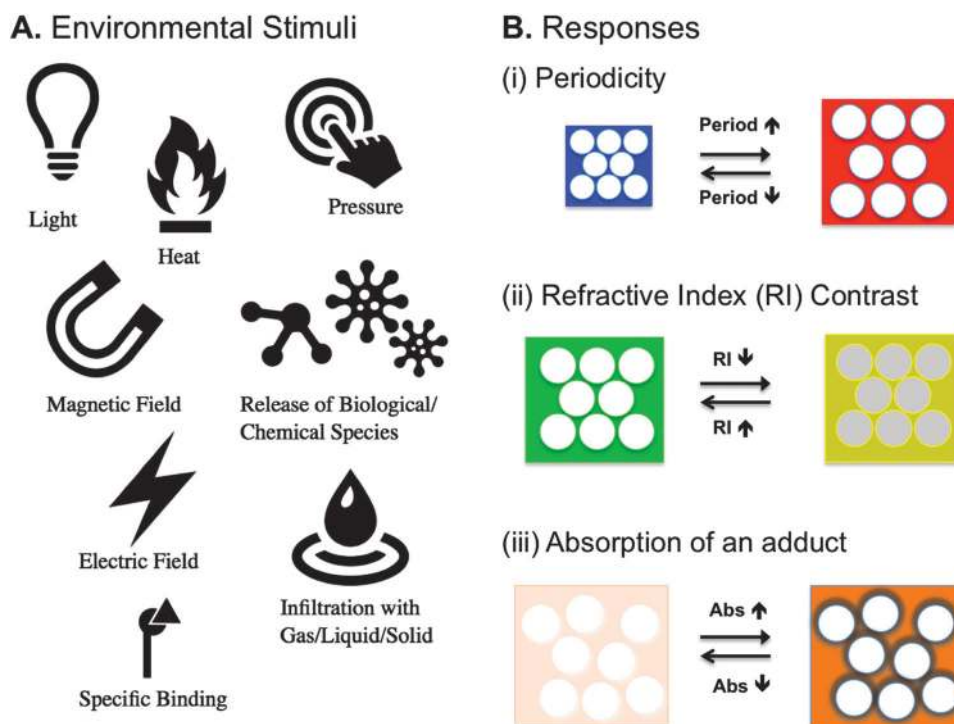


**Fig. 16** Overview of sensing parameters. (A) Possible physical, chemical, and biological stimuli. (B) Response mechanisms include: (i) change in the periodicity, where an increase in the lattice constant results in a red shift in the CBPM stopband; (ii) change in the refractive index contrast between the pores and the filler, where a decrease in refractive index contrast, accompanied by positive change in the average refractive index, results in a decrease in the intensity of the reflectance and a red shift in the peak; and (iii) change in the absorption intensity of an additive incorporated into the CBPM, where higher absorption intensity can result in an increase in the saturation of the observed color.
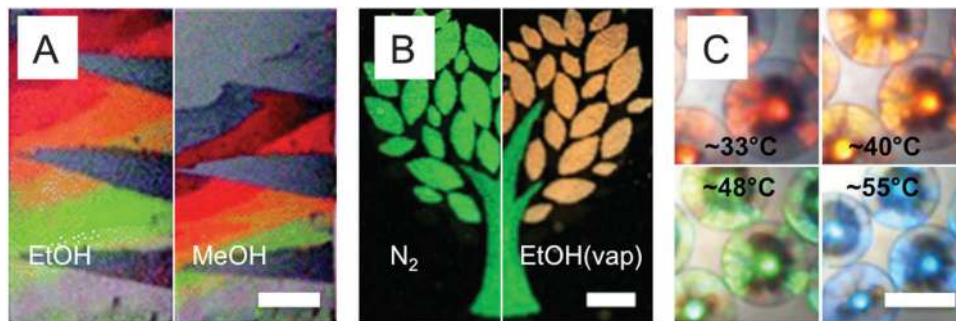
**Fig. 17** CBPM colorimetric sensors with varying degrees of hierarchy designed to respond to various types of stimuli. (A) Spatially and chemically patterned silica inverse opal film for identification of liquids.[77] The sample is shown wetted with ethanol (left), and methanol (right). Scale bar 5 mm. Reproduced with permission from the American Chemical Society, copyright 2012. (B) Spatially patterned CBPM with direct opal structure for sensing of vapors, formed by inkjet printing of solid silica colloids (the trunk) and mesoporous silica colloids (the leaves).[260] The sample is shown (left) before, and (right) after exposure to ethanol vapors. Scale bar 5 mm. Reproduced with permission from the American Chemical Society, copyright 2014. (C) Temperature responsive spherical superparticles with inverse opal structure made of poly($n$-isopropylacrylamide) hydrogel.[267] Scale bar 200 μm. Reproduced with permission from the Royal Society of Chemistry, copyright 2015.

discuss how CBPM provide control over the composition, surface chemistry, and structural hierarchy, which are all beneficial for sensing applications.

Photonic effects can influence the photoinduced performance of entrapped functional components such as plasmonic nanoparticles. Indeed, efficient surface enhanced Raman scattering (SERS) substrates[253] have been made from colloidal templating for enhancement of plasmonic photoexcitation within the partial photonic bandgap. In this section, we focus on sensing applications that rely on structural and chemical changes in CBPM. The design of substrates for localized surface plasmon resonance (LSPR) applications such as SERS has been discussed extensively elsewhere[254–256] and is beyond the focus of the current review.

Colloid-templated sensors can take many forms. They can be confined in a thin film or formed as discrete superparticles, both of which can be spatially, chemically, and structurally patterned (as shown in Fig. 17). Because of these different forms, CBPM sensors can be made as standalone indicators or integrated within a complex device, such as an electrochemical cell,[257,258] microfluidic device,[259] or miniaturized spectrometer.[143] Their sensing mechanism can be tailored through chemical functionalization to achieve a response to various environmental stimuli. In addition, CBPM sensors can be structurally patterned in order to obtain an explicit visual readout[260] (Fig. 17A and B) or be molecularly imprinted to target specific molecules.[261–266] The high surface area inherent to CBPM can lead to higher analyte–surface interactions with advantageous signal-to-noise ratios. Furthermore, the presence of macropores and stimuli-responsiveness allows the use of CBPM superparticles for multiple functions, for example to combine optical reporting with self-monitored drug release.[267]

**5.1 Factors influencing sensing applications**

**Composition.** Materials used for the fabrication of colorimetric CBPM sensors define their appearance, response mechanism, and ultimately possible applications. Changing the average refractive index, refractive index contrast, and spectral properties

of adducts in a photonic crystal results in a color shift, as shown in Fig. 16 and discussed in the Optics section. The color shift induced by infiltration of liquids into the pores can be used for the identification of liquids.[268,269] Infiltration of the pores with a material capable of changing its refractive index in a stimuli-responsive manner can be used as a strategy to design CBPM sensors. For example, hexaphenylsilole (HPS) can be reversibly transformed from crystalline to an amorphous solid upon exposure to vapors of volatile organic compounds (VOCs).[270] This transformation is accompanied by an increase in the refractive index from 1.243 to 1.373 in the case of diethyl ether vapors. Infiltration of a silica inverse opal with HPS molecules thus enables a colorimetric response to the presence of VOCs, as shown in Fig. 18. The sensitivity of this system to
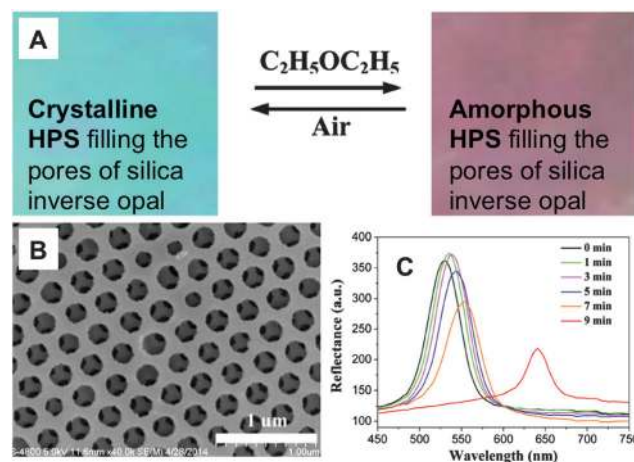


**Fig. 18** Silica inverse opals infiltrated with hexaphenylsilole (HPS) change color upon exposure to vapors of diethyl ether due to a change in refractive index stemming from a crystalline to amorphous transition of HPS within the matrix.[270] (A) Optical images of a sample upon exposure to air and diethyl ether vapor. (B) SEM image of a silica inverse opal film before infiltration with HPS. (C) Optical reflectance spectra obtained during exposure of the HPS-infiltrated inverse opal film to the vapors of diethyl ether for different amounts of time. Reused with permission from the Royal Society of Chemistry, copyright 2014.

the presence of VOCs is on the level of ~1000 ppm. Similarly, a titania inverse opal infiltrated with polyaniline, which has a refractive index sensitive to its protonation state,[271] creates a colorimetric indicator that responds to the presence of acidic or basic vapors (HCl and NH$_3$).

As discussed in the Optics section, a broadband or selective absorber incorporated into the structure of CBPM can greatly influence its visual properties by decreasing the amount of incoherently scattered light or suppressing certain unwanted diffraction peaks.[22,103] Moreover, the contrast-enhancing material can have stimuli-responsive absorption properties, which can be used for modulations of the appearance of a CBPM sensor. In the example shown in Fig. 19, an amorphous array of silica colloids incorporating silver ions and a small amount of titania nanoparticles can show different degrees of color saturation based on the oxidation state of silver.[272] Photo-induced electron transfer between titania nanoparticles and silver ions was used to modulate the color saturation. The direction of the electron transfer is wavelength dependent, allowing the formation (under UV) or oxidation/decomposition (under visible light) of silver nanoparticles.

The colorimetric response of CBPM sensors based on soft stimuli-responsive materials can originate from changes in both the periodicity and the refractive indices of its constituents, as shown in Fig. 16B. Examples of soft materials used for CBPM sensors include hydrogels,[178,261–265,273–280] electroactive polymers,[176,281,282] elastomers,[24,174,283] natural polymers,[189,284–286] poly(ionic liquids),[287–289] and metal–organic frameworks.[290,291] Stimuli-induced shifts in the periodicity of these types of CBPM sensors can be induced by swelling or deformation that in turn results in the shift in the photonic stopband (Fig. 16B(i)) and can be detected visually or using a spectrometer.

Stimuli responsive hydrogels are among the most frequently used materials for the formation of photonic crystal-based sensors. Upon application of various stimuli, the hydrogel network can undergo a phase transition resulting in a volume change.[292] Hydrogel CBPM are often formed by infiltration of a direct opal colloidal array with a predesigned mixture of monomers followed by a polymerization step (e.g. light exposure) and subsequent dissolution/etching of the colloidal template.[292] In fact, the dissolution is not a necessary requirement for forming structural color sensors. Colloidal crystals embedded in hydrogels have been extensively developed during the last two decades with diverse chemistry and functions.[293–306] These systems were well covered in a number of recent reviews;[307,308] in the current discussion we focus on systems that benefit from colloid-templated interconnected pores. Among the advantages of porous structures over the embedded colloids are facile diffusion and shorter response times to various stimuli.[274,309,310]

Specific functional groups can be incorporated into the gel by premixing the corresponding co-monomers before polymerization or by modification of the CBPM after its formation.[311,312] Hydrogel CBPM sensors based on such monomers as acrylamides and carboxylic acids are capable of detecting changes in pH, ion concentration, and heat.[178,274,313] Moreover, incorporation of specific target molecules and enzymes allows label-free detection of glucose,[310] enzymatic activity,[279] and antibodies[276] with remarkable sensitivity. For example, the level of detection that was achieved using a CBPM assay for acetylcholinesterase is of 5 mU mL$^{-1}$ (U = "enzyme units").[279] This level is comparable to other existing highly sensitive methods such as those based on gold nanoparticles,[314] but the CBPM indicator is more reliable, particularly in complex solutions.[279] An example of a pH-responsive inverse opal hydrogel sensor with high selectivity and sensitivity to mercury ions is shown in Fig. 20.[278]

An additional method to introduce binding specificity to hydrogel materials is molecular imprinting.[261–266] To generate an imprinted CBPM sensor matrix, the template molecule is pre-complexed to the monomer before the polymerization step. In the next step, the template molecule is removed, exposing a highly selective recognition site. Using this method, highly sensitive and selective label-free colorimetric assays were demonstrated for applications such as amino-acid chiral recognition,[266] as well as detection of vanillin,[315] various antibiotics,[262] and toxins[263] at sub-micromolar concentrations.

Incorporation of multiple elements in a single CBPM sensor can result in multi-responsiveness, multiple reporting mechanisms, and multi-functionality. For example, incorporation of glucose oxidase and a conductive polymer into an inverse opal hydrogel resulted in a glucose sensitive system with both optical



Fig. 19 Photoinduced saturation changes in silica amorphous colloidal arrays.[272] (A) Schematic representation of the photoinduced formation (under UV) or oxidation/decomposition (under visible light) of silver nanoparticles in the presence of titania nanoparticles leading to visual changes in the saturation of the structural color. (B) Changes in the intensity of absorption at 500 nm of the Ag/TiO$_2$ composite film exposed to alternating UV (313 nm) and visible (>420 nm) light. (C) Samples after exposure to light: (left) the changes in the reflection spectra and the corresponding optical images of the colloidal amorphous array exposed to UV light of varying intensity; (right) the same samples after exposure to visible light for 12 hours. Reproduced with permission from the Royal Society of Chemistry, copyright 2014.
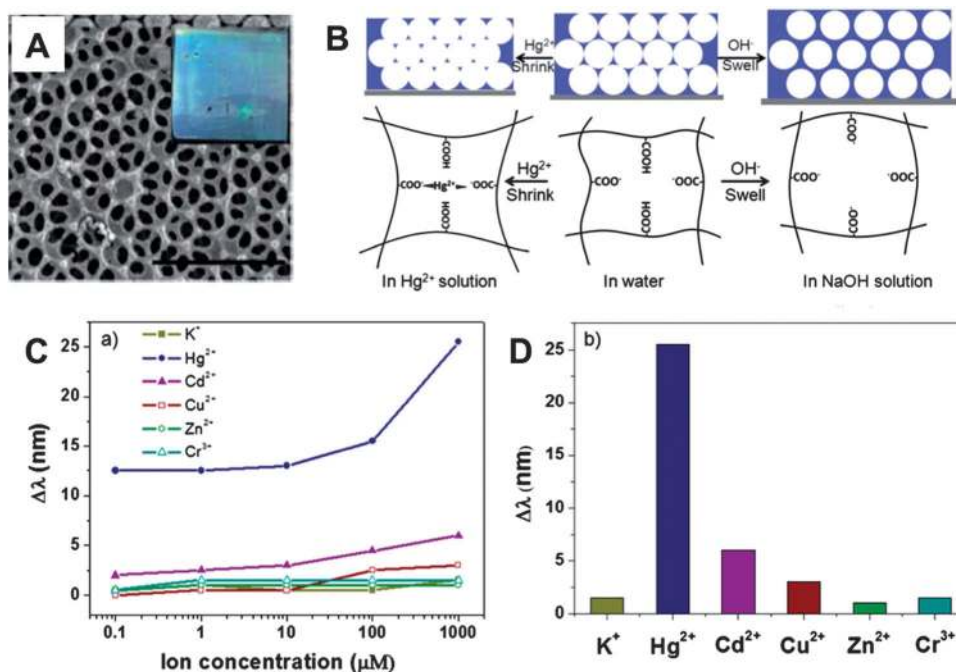
**Fig. 20** Hydrogel inverse opal for pH and mercury ion sensing.[278] (A) SEM image of the structure. An optical image of the sample is shown in the inset. (B) Schematic diagram of the pH and $Hg^{2+}$ sensing mechanism. (C) The diffraction wavelength shift as a function of the ion concentration for various ions in aqueous solution. (D) Comparison of the diffraction wavelength shifts for various ions at 1 mM concentration, showing selectivity for $Hg^{2+}$. Reproduced with permission from the Royal Society of Chemistry, copyright 2014.

and electric readouts.[258] Similarly, systems responsive to both temperature and acids/bases can be obtained, for example by copolymerizing *N*-isopropylacrylamide and methacrylic acid.[313] Moreover, these systems can be further modified with light responsive (*e.g.* azobenzene) or magnetic field responsive (*e.g.* iron oxide nanoparticles) functions.[178]

CBPM sensors can also be made of natural materials such as proteins and polysaccharides, for example silk fibroin,[284,285] chitosan,[286] and cellulose.[316] The colorimetric changes in these systems were shown to result from changes in the refractive index contrast, average refractive index contrast, and swelling. Thus, silk inverse opals have been made that are sensitive to infiltration with water,[285] various concentrations of glucose in aqueous solutions, and to humidity.[284] Chitosan inverse opals[286] were made that are sensitive to various organic solvents, pH values, and ionic strengths. For example, the reflectance peak of the chitosan inverse opal shifts almost linearly with increasing concentration of various alcohols in water, in the entire range from pure water to pure alcohol, with an overall shift of ~100 nm. Due to their biocompatibility and eco-friendly character, CBPM sensors made of natural materials can be beneficial for biomedical applications and fabrication of disposable sensors.

**Porosity.** High surface area and interconnectivity of the pores are important properties of CBPM for sensing applications. The high surface area allows enhanced interaction of the matrix with analytes resulting in an enhanced signal. The interconnectivity of macropores allows facile diffusion within the structure, even of large analytes,[317] and shortens the response time. For example, the equilibration time of inverse opal hydrogel based

sensors can be considerably shortened (seconds *vs.* minutes) compared to their nonporous analogs based on direct colloidal structures embedded into hydrogels.[318]

Infiltration of liquids into the pores of CBPM changes the refractive index contrast and the average refractive index and thus results in a change in the appearance of the photonic structure.[77,78,269] This property can be used for measurements of the refractive index of the liquids and their identification, for example for $WO_3$ inverse opals.[269] However, since the refractive index of common liquids is in a narrow range between ~1.33–1.50, the change in color and the intensity of the reflection spectrum is not always large enough to be easily observable by the naked eye. As discussed in the Wetting section, the geometry of the pores of the structure and the intrinsic contact angle of the liquids with the surface material together control liquid infiltration into silica inverse opal pores. Therefore, modification of the surface of the pores with functional molecules can result in selective infiltration of various liquids, as shown in Fig. 15C. The high uniformity of the pores originates from co-assembling the colloids and matrix material, and it results in a narrow threshold for infiltration. In addition, the surface chemistry can be patterned to achieve a combinatorial wetting sensor[319] with an easy-to-read colorimetric response (as shown on Fig. 17A). Stimuli-responsive functional groups, such as Disperse Red 1 acrylate, can reveal the history of the sensor's exposure to light. Such a system has high potential for use as forgery-resistant and age-reporting labeling.[320] Another way to record the history of exposure of the sensor to a stimulus is to cause a deformation in the CBPM structure. For example, exposure of silica inverse opals to high temperatures can lead to

anisotropic structures, resulting in a predictable color change and complex wetting properties.[99,239]

Incorporation of mesopores into CBPM can result in a system that responds colorimetrically to infiltration with gases due to changes in the average refractive index of the photonic crystal. For example, Fig. 17B shows spatially patterned CBPM sensors made with mesoporous silicon dioxide colloids fabricated through inkjet printing for visual detection of vapors of organic solvents.[260] The tree trunk and the leaves are made of solid and mesoporous silica colloids, respectively. The size of the colloids was chosen so that they appear similar in the absence of vapors but develop different colors upon exposure to organic vapors such as ethanol.[260] Furthermore, mesopores produced through molecular imprinting of CBPM made of stimuli-responsive hydrogels, as discussed earlier, can result in a label-free colorimetric sensor to various analytes with high specificity.[261–266]

**Degree of order.** In addition to directly generating color from their structure, photonic CBPM sensors can substantially enhance the fluorescence signal of organic molecules incorporated inside the pores when the absorption spectrum of the chromophore is aligned with the stopband of the structure. Consequently, the signal-to-noise ratio is increased in the presence of fluorescently labeled analytes[321] or those capable of quenching a fluorescence signal.[322,323] For example, quenching of the fluorescence signal in the presence of vapors of nitroaromatics can be detected with enhanced sensitivity.[322,323]

As discussed in the Optics and fabrication sections, the design of colored CBPM classically assumes crystalline arrangements of colloids with long-range order, analogous to the naturally iridescent opal gemstone. Amorphous arrays generally exhibit lower saturation; however, when a broadband absorber, such as melanin,[5] silver nanoparticles,[180] or iron oxide,[183] is incorporated into these systems, bright angle-independent colors can be achieved.[180,182] Consequently, stimuli-responsive structurally-colored amorphous arrays have become a popular topic in recent years. One recent example of a light-responsive amorphous array is shown in Fig. 19.[272] Additional examples include colorimetric indicators that respond to temperature,[183] electric field,[183] and osmotic pressure.[185] Due to their angle-independent color, disordered CBPM colorimetric sensors simplify the readout step and thus are advantageous when the sensors are being used as stand-alone indicators.

**Hierarchy and patterning.** CBPM sensors can be designed at many length scales and can adopt different architectural features. The ability to control the organization of CBPM architectures at many hierarchical levels is important for obtaining systems with dimensions appropriate for specific applications (*i.e.* films or superparticles), with explicit reporting signals (for example in Fig. 17A and B),[260] and with multi-analyte sensing capability.[324] Multi-analyte cross-reactive arrays combining CBPM elements, for example based on molecularly imprinted hydrogels, can be used for colorimetric detection of trace amounts of toxins and pollutants in complex mixtures even with high background signal from the other components.[263,324] An array sensitive to brominated flame-retardants, commonly used as additives in consumer products, is shown in Fig. 21.[324] Monitoring of brominated flame-retardants at low levels normally requires
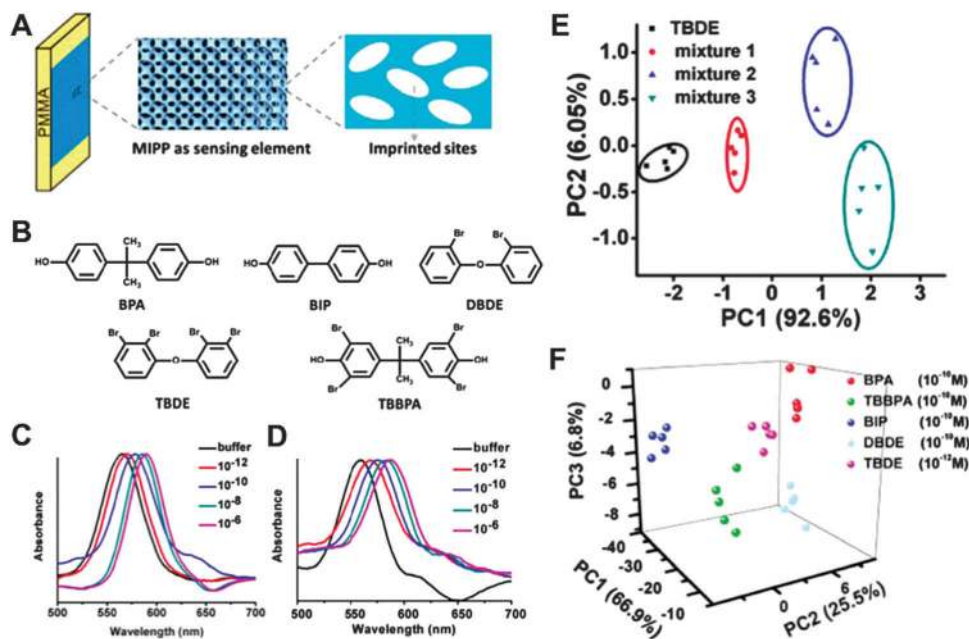


Fig. 21 Spatially patterned molecularly-imprinted inverse opal array for the detection of poly-brominated diphenylethers.[324] (A) Schematic illustration of the preparation of the array. (B) Molecular structures of the analytes used (BPA, BIP, DBDE, TBDE, and TBBPA). (C) Optical response of the BIP-imprinted sensor to DBDE. (D) Optical response of TBBPA-imprinted sensor to TBDE. (E) 2D principal component analysis plot for the identification of TBDE and three different mixtures by the molecularly-imprinted sensor array, where mixture 1 is TBDE and BPA, mixture 2 is TBDE, BPA, and TBBPA, and mixture 3 is TBDE, BPA, TBBPA and BIP. (D) 3D principal component analysis plots for the identification of each analyte (TBDE: $1 \times 10^{-12}$ M, BPA: $1 \times 10^{-10}$ M, TBBPA: $1 \times 10^{-10}$ M, BIP: $1 \times 10^{-10}$ M and DBDE: $1 \times 10^{-10}$ M) by the MIPPs sensor array. PC1, PC2, and PC3 represent the principal components calculated. Reproduced with permission from the Royal Society of Chemistry, copyright 2014.
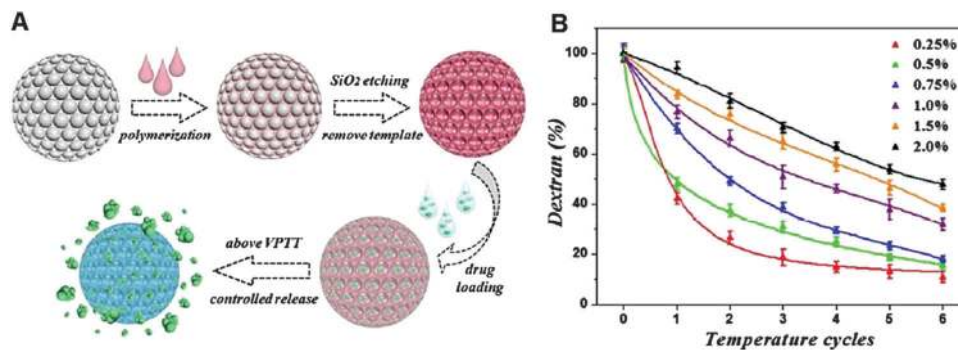
**Fig. 22** Temperature-responsive hydrogel inverse opal superparticle sensors with controlled drug release.[267] (A) Schematic illustration of the fabrication and controlled drug release of the particles. (B) Release profiles of fluorescently-labelled dextran from the particles under different temperature cycles. Reproduced with permission from the Royal Society of Chemistry, copyright 2015.

relatively complex chromatographic analyses. The use of molecularly-imprinted spatially patterned inverse opal arrays combines low-cost fabrication of the sensors, simple and fast analysis of the results, and the ability to detect picomolar amounts, comparable to chromatographic methods. As discussed earlier, the hierarchical network of interconnected macropores in the CBPM allows facile diffusion of the analytes resulting in enhanced signal and quick response.

In addition to multiple analyte sensing, hierarchy can be achieved using superparticles, which have been used as dispersible indicators for various stimuli. For example, spherical inverse opal superparticles based on poly(ionic liquids) were used for recognition of various ions and solvents,[288,289] and protein-modified silica superparticles were used as coding carriers in multiplex immunoassays.[325] Additionally, the high surface area of the pores can be used for adsorption and triggered release of drugs in addition to sensing.[267] As shown in Fig. 17C, temperature responsive spherical inverse opal superparticles change their color due to a change in the periodicity of their lattice when exposed to different temperatures. Preloaded with fluorescently labeled dextran molecules, these superparticles can be used for self-monitored temperature-triggered drug release based on a temperature-induced shrinkage. The formation of the superparticles and the kinetic profile of the release of the fluorescently-labeled dextran is shown in Fig. 22. CBPM superparticles can also be used as a dispersible cell culture substrate capable of reporting on the interaction of cells with biomaterials in a single culture environment.[326] Because their color originates from their structure, the signal from CBPM microcarriers is stable.

### 5.2 Perspective

Colloidal templating is the most facile and developed up-to-date approach for obtaining photonic crystal arrays capable of providing a colorimetric response while using simple, colorless, inexpensive, inert, and non-toxic stimuli-responsive materials. The state of the art CBPM sensor can compete with considerably more sophisticated analytical instruments in providing specific responses to various physical, chemical, or biological stimuli. A key advantage of CBPM sensors is their modularity of

design, allowing combinations of various architectures, structural materials, surface chemistries, and degrees of order. CBPM sensors can have very small physical dimensions, be remotely monitored, and in principle do not require any additional optical, chemical, or electronic modules, which improves their reliability and security. Compared to their 1D and 2D analogs, such as Bragg stacks, gratings, and crystal fibers, CBPM sensors have greater sensitivity due to their higher surface area available for interaction with analytes and shorter response time due to facile diffusion through the pores. Finally, the response of CBPM-based sensors can be designed to be reversible or irreversible, capable of monitoring and/or recording the history of their environment.

CBPM sensors have technological potential as easy-to-use and inexpensive sensing devices, which has motivated intense research in the last few decades. On a fundamental level, a better understanding of the processes governing the self-assembly of colloidal particles on substrates and in droplets is still necessary, particularly as the field moves to larger scale production. On a more applied level, a great variety of sensing approaches utilizing CBPM sensors are being explored, fostering their novel applications with additional stimuli responses, as well as improved sensitivity, specificity, reproducibility, and longevity.

## 6. Catalytic applications

Heterogeneous catalysis is of paramount importance in many areas of the chemical and energy industries including coal, oil and gas refining; polymer production; environmental pollutant degradation; and manufacturing of fine chemicals and pharmaceuticals.[327] Having a solid-phase catalyst improves catalyst recovery and product separation. The great majority of practical heterogeneous catalysts consist of metal oxides serving as solid catalyst or catalyst support, and their design for optimum performance for a given process requires a consideration of a combination of chemical, structural, and mechanical properties. CBPM can be made with high surface area, interconnected porosity, and control over material composition, all of which are important for developing catalysts having high activity and selectivity, thermal stability, and superior mass transport (Fig. 23).[58,79]
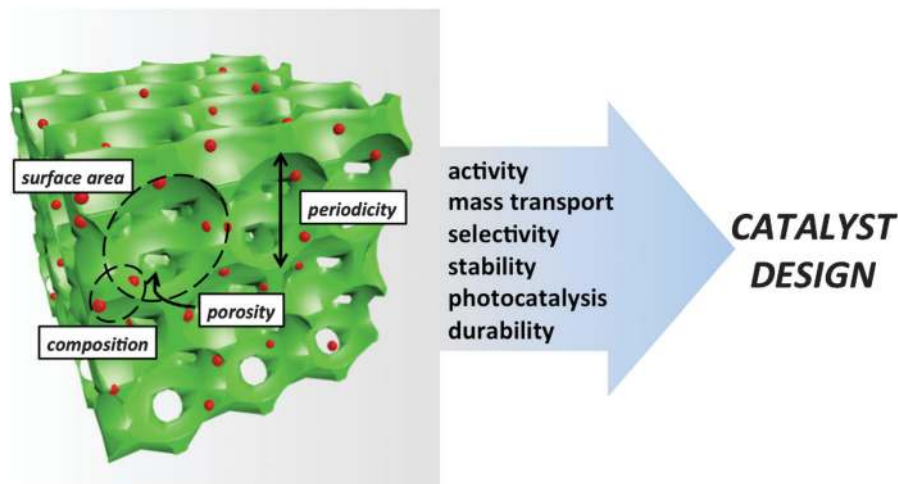
**Fig. 23** Schematic summarizing the advantageous properties provided by CBPM for the design of an efficient heterogeneous catalyst.

CBPM possess many advantageous characteristics and degrees of freedom that enable them to be designed for a wide range of catalytic applications (Fig. 23). They exhibit architectural tunability easily achievable *via* hierarchical templating and characterized by a porous network where many factors can be controlled, including wall thickness, pore size, pore interconnectivity, and shape. The incorporation of hierarchical porosity using colloidal-crystal templating in combination with soft templates (*e.g.* surfactants) offers minimal diffusive limitations to mass transport by macropores (pore diameter $\geq \sim 30$ nm), and high surface area for active site dispersion over micro and/or mesopores (pore diameter $\leq 1.5$ nm and 1.5–30 nm, respectively).[79] Additionally, templated structures are used almost exclusively in order to increase the macroporosity and decrease the amount of material used. CBPM assembly methods allow good control over the composition and incorporation of functional materials (*e.g.* metal nanoparticles), important for achieving improved catalytic activity, selectivity, and stability of the resulting catalyst.

During the last decade, much effort has been put into developing CBPM for various catalytic processes including oxidation and reduction of industrial and automotive harmful byproducts, chemical fuels catalysis, biomass upgrading, photocatalysis, and water splitting.[58,64,79] For example, CBPM have been used in such environmentally important catalytic processes as removal of CO, uncombusted hydrocarbons (*e.g.* soot), and volatile organic compounds (VOCs) emitted from transportation and industrial activities.[58,79,328] Various supported noble metals and single or mixed metal oxides have been used for this purpose. Interconnected porosity on multiple length scales and low tortuosity are both especially important for liquid phase catalysis involving large bulky molecules in processes such as chemical fuel catalysis (including crude oil cracking, isomerization, and reforming), photocatalytic degradation of organic compounds, and biomass upgrading.[64,79,329] The importance of structural order (periodicity) varies for the different types of catalytic reactions. For example, ordered CBPM, widely referred to in the literature as three-dimensionally ordered macroporous materials (3DOM) or inverse opals, are of particular interest in

photocatalysis due to their photonic properties as well as their superior mass transfer through interconnected pore channels.[67,330]

This section will focus on the application of CBPM to distinct catalytic reactions, with emphasis on the advantages of CBPM structural parameters for catalyst systems, namely the ability to control the composition, porosity, and periodicity of the structure. Table 1 lists specific examples of colloid-based porous catalysts that have been fabricated and studied, focusing on the past four years. While the material composition is an inherent characteristic of any type of catalyst, the additional advantages achieved with CBPM such as mass transport and periodicity can play a significant role in specific catalytic reactions and will be discussed in separate sections below. We summarize how the challenges and limitations of specific catalytic reactions can be addressed using CBPM, discussing both highly ordered 3D architectures and low periodicity/irregular systems generated from colloidal templating.

### 6.1 Factors influencing CBPM catalysts

**Surface area and composition.** The composition and active surface area of a catalyst are crucial to its performance, particularly for the removal of industrial and automotive byproducts (*e.g.* CO, soot, NOx, VOCs). Controlling composition provides thermal stability and chemical reactivity (*e.g.* selectivity, large oxygen storage capacity), while high surface area ensures catalytic efficiency. Colloidal templating creates porous materials with facile control in composition and morphology with wide suitability for many metal precursors, allowing their use in a variety of catalytic reactions.

The intrinsic catalytic activity of metal oxides can be enhanced by incorporation of noble metal nanoparticles (*e.g.* Au, Pt, Pd).[398] Because the composition and additives can be controlled independently in CBPM structures, a variety of materials have been investigated (see Table 1). For example, Wei *et al.* fabricated hierarchical macro/meso porous catalysts for soot combustion from platinum nanoparticles (NPs) supported on various transition metal oxides (with M = Mn, Fe, Co, Ni, Cu).[337] The resulting materials possessed a well-defined macroporous structure with

**304** | *Chem. Soc. Rev.*, 2016, **45**, 281–322

This journal is © The Royal Society of Chemistry 2016

**Table 1** Recent reports describing diverse CBPM-based catalysts used in various types of catalytic reactions

| Catalytic transformations | Active catalyst and support in colloid-based catalytic systems |
|---|---|
| **Environmental catalysis** CO and toluene oxidation | $CeO_2$;[331] $Au/Mn_2O_3$;[332] $Pr_6O_{11}$;[333] $Tb_4O_7$;[333] $Au/Co_3O_4$;[334] $Au/Mn_2O_3/La_{0.6}Sr_{0.4}MnO_3$;[328] $Co_3O_4/Eu_{0.6}Sr_{0.4}FeO_3$;[335] $Au/La_{0.6}Sr_{0.4}MnO_3$[336] |
| Soot combustion | $Pt/MO$ (M = Mn, Co, Fe, Ni, Cu);[337] $Pt@CeO_2/CeO_2$;[338] $Au@Pt/Ce_{0.8}Zr_{0.2}O_2$;[339] $Au/LaFeO_3$;[340,341] $Au/CeO_2$;[342] $Au–Pt/Ce_{0.8}Zr_{0.2}O_2$;[343] $Pt/MnCeO$;[344] $Al_2O_3/CeO_2$;[345] $Au/LaFeO_3$[340,341] |
| NOx reduction | $Ce_{0.75}Zr_{0.2}M_{0.05}O_{2-\delta}$ (M = Fe, Cu, Mn, Co);[346] $CeO_2/TiO_2$[347] |
| Methane oxidation | $Pt/Ce_{0.6}Zr_{0.3}Y_{0.1}O_2$;[348] $Pd/LaMnO_3$;[349] $Ag/La_{0.6}Sr_{0.4}MnO_3$[350] |
| **Chemical fuel synthesis** Isomerization | $Pt/SiO_2$, $Al_2O_3$, $TiO_2$, $Nb_2O_5$, $Ta_2O_5$, $ZrO_2$[351] |
| Cracking (oil) | $Al_2O_3/SiO_2$[342] |
| Fischer–Tropsch | $Co@Cu/SiO_2–La_2O_2$;[352] $Fe_2O_3$[353] |
| Biodiesel production | Mg–Al hydrotalcites;[354] $Al_2O_3$-hydrotalcites/$SiO_2$[355] |
| **Selective organic transformations** Selective oxidation | $Pd/SiO_2$;[356] $Al/SiO_2$;[357] $VO/SiO_2$[358] |
| Suzuki cross-coupling | $Pd/SnO_2$[359] |
| **Photocatalysis** $CO_2$ reduction | $CeO_2/TiO_2$;[360] $Au/TiO_2$;[361] |
| Oxidation of organics | $TiO_2$;[362–366] $TiO_2/SiO_2$;[367] $Fe^{3+}/TiO_2$;[368] $Ti^{3+}/TiO_2$;[369] $N/TiO_2$;[370] $C/TiO_2$;[371] $K_5[Co(H_2O)PW_{11}O_{39}]/TiO_2$;[372] $CuO/TiO_2$;[373] $ZrO_2/TiO_2$;[374] $SnO_2/TiO_2$;[375] $Au/TiO_2$;[98,376] $Ag/TiO_2$;[377,378] $Ag/Bi_2O_3–TiO_2$;[379] $ZnO$;[378,380] $BiFeO_3$;[381] $Bi_2WO_6$;[382] $W_{10}O_{34}/Mg_2Al$;[383] $BiVO_4$;[384] Au, Pt, $Pd/AgBr/BiVO_4$;[385] $InVO_4$;[386] $Cr_xO_yTiO_2/SiO_2$[387] |
| Water splitting | $\alpha$-$Fe_2O_3$;[388] $TiO_2$;[70] $Au/TiO_2$;[389] $TaON$;[390] $WO_3/BiVO_4$;[391] $WO_3$;[392,393] graphene/$Fe_2O_3$;[394] $Cu_2O_3$;[395] quantum dot/$TiO_2$;[396,397] $Mo/BiVO_4$[25] |

mesopores of ∼6 nm and Pt NPs (2.9–3.5 nm) highly dispersed on the inner walls of the macropores. The strong metal–support interactions and unique porous architecture in these systems improved the contact efficiency between catalyst and soot leading to higher catalytic activity for diesel soot combustion.

The incorporation of metal NPs into inverse opal scaffolds can also be used to enhance photocatalytic properties. The plasmonic properties of metal NPs can couple with the semiconductor properties of the support. Under visible-light illumination, plasmon-excited hot electrons in noble metal NPs can transfer to the conduction band of an adjacent semiconductor, leading to charge transfer/separation and subsequent chemical reactions.[63,399] For example, $TiO_2$ inverse opals incorporating Au[98,361,376,400] and Ag[377,378] NPs have shown improved photocatalytic dye degradation and $CO_2$ reduction.[361] This effect can be strongly enhanced by engineering periodicity at the right wavelength through colloidal templating, and it will be discussed in more detail below.

$TiO_2$ photocatalysts also benefit from other aspects of control over the composition. Titania suffers from a high rate of charge carrier recombination and a relatively wide band gap (3.2 eV), limiting the light absorption to UV irradiation, which accounts for less than 5% of the total energy of the solar spectrum. To overcome these drawbacks and improve photocatalytic activity, multiple components are often incorporated to tune the band structures and electron–hole separation and

transportation.[330,401] Many studies have attempted to introduce metal-ions[368,369] or nonmetals[370] as dopants; and dyes,[402] quantum dots,[396] or carbon[371] as sensitizers or for surface modification.[372] Coupling $TiO_2$ with other transition metal oxides can enhance the photocatalytic performance via improving the charge separation of photogenerated charges and extending the photoresponse region, thus facilitating the degradation of organic dyes and $CO_2$ reduction (Table 1).[360,373–375] For example, Li et al. demonstrated excellent activity for the photocatalytic degradation of crystal violet using a composite $Ag/Bi_2O_3–TiO_2$ macroporous inverse opal with mesoporous walls by employing different radiation sources such as UV, simulated solar light, and microwave-assisted irradiation.[379] Compared to $TiO_2$, the light absorption edge of ordered macro/meso porous $Ag/Bi_2O_3–TiO_2$ structures was red-shifted by about 100 nm into the visible region. The catalytic activity of this ordered composite structure was significantly higher than that of $TiO_2$ nanopowder (P25), $Bi_2O_3$, and disordered $Ag/Bi_2O_3–TiO_2$ and was retained after three cycles. In addition to $TiO_2$-based inverse opal photocatalysts, novel visible-light-responsive materials have been reported including both single semiconductor materials[378–382,384,386] and heterostructured systems (Table 1).[333,383]

In the past few years, several authors developed rare earth oxide-based catalysts for CO, toluene, and soot oxidation.[333] Among the rare earth metal oxides, ceria ($CeO_2$) is one of the most extensively investigated as an environmental catalyst due

This journal is © The Royal Society of Chemistry 2016

Chem. Soc. Rev., 2016, 45, 281–322 | 305
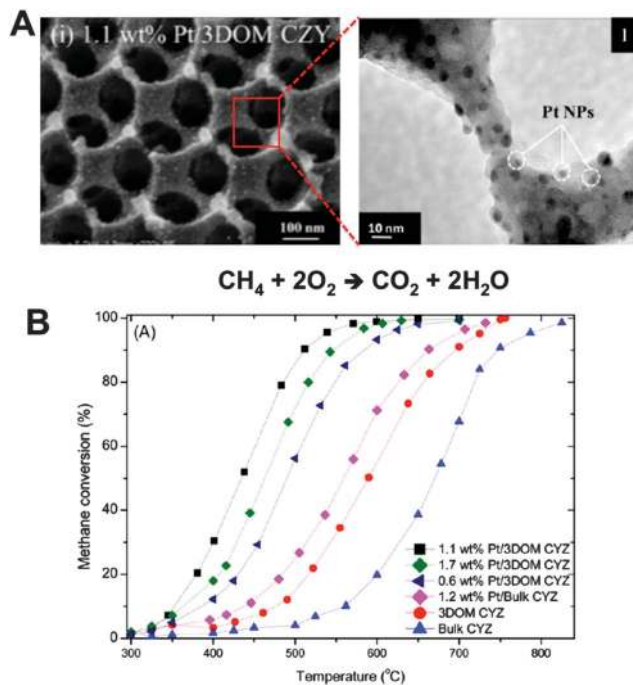
$$CH_4 + 2O_2 \rightarrow CO_2 + 2H_2O$$

**Fig. 24** Fabrication of colloid-based hierarchically porous catalysts incorporating metal NP for oxidation of methane. (A) Representative SEM image of 3D ordered macro/mesoporous $Ce_{0.6}Zr_{0.3}Y_{0.1}O_2$ (CZY) embedded with PtNP (1.1 wt%). (B) Methane conversion *versus* temperature over the macroporous CZY, *x* wt% Pt/CZY, and Bulk CZY catalysts.[348] Reused with permission from the American Chemical Society, copyright 2015.

to its high oxygen storage capacity, good sulfur-resistance, and excellent redox properties.[403] However, a major drawback of pure $CeO_2$ is low thermal stability causing sintering and loss of its redox and oxygen storage properties. Various ceria-based mixed metal oxides including Al–Ce,[345] Ce–Ti,[347] and Ce–Zr[346] have been used as active catalysts for the oxidation of CO, methane, soot, and NOx. Among these binary compounds, $Ce_{1-x}Zr_xO_2$ ($x$ = 0.1–0.9) is considered to be one of the key components in auto-exhaust treatment catalysts due to its high oxygen storage/release capacity and good thermal stability. Recent studies have produced a variety of colloid-based porous Ce–Zr binary oxides and composite structures incorporating metal NPs.[339,343,344] For example, Arandiyam *et al.* fabricated 3D ordered macro/mesoporous $Pt/Ce_{0.6}Zr_{0.3}Y_{0.1}O_2$ (CZY) catalysts for methane combustion using PMMA as hard template and pluronic (P123) as surfactant (Fig. 24A and B).[348] The excellent catalytic activity of Pt/CZY was ascribed to an increase in surface area due to its unique macro/mesoporous structure as well as its high concentration of adsorbed oxygen, good low-temperature reducibility, and strong catalyst-support interaction due to composition.

In addition, the colloid-based templating approach has been used to prepare high-surface area perovskite-type oxides ($ABO_3$) with porous architectures.[340,341] It was reported that doping with rare earth metals (*e.g.* La, Eu) and/or loading a certain amount of transition metal oxides onto colloid-based $ABO_3$ supports can enhance the catalytic performance for toluene oxidation.[328,333,335]

In addition, the loading of noble metal NPs on $ABO_3$ generates catalysts with higher catalytic oxidation activity.[328,331,349,350] For example, Au NPs supported on colloid-based porous $La_{0.6}Sr_{0.4}MnO_3$ (LSMO) outperformed undoped LSMO structures in the oxidation of CO and toluene.[336] Similarly, Pd NP supported $LaMnO_3$[349] and Ag NP supported $LaSrMnO_3$[350] demonstrated improved catalytic activity toward methane oxidation.

**Mass transport/porosity.** Poor mass transfer of bulky molecules and pore blockage represent significant challenges for liquid phase heterogeneous catalysts, particularly for crude oil cracking, selective organic transformations, and biomass upgrading. For example, catalytic cracking of crude oil is vital for the large-scale generation of commodity compounds. The design of hydrothermally stable materials with an interconnected macro-meso-micropore system remains a great challenge.[342]

Implementation of catalytic materials exhibiting hierarchical and interconnected macro-mesoporous networks such as CBPM can enhance both internal mass and heat transfer and active site dispersion and accessibility, particularly for such low temperature, liquid phase chemistry as selective transformations of organic molecules. Higher catalytic activity of CBPM systems over their purely mesoporous counterparts has been demonstrated in selective oxidation,[356–358] Suzuki coupling,[359] and epoxidation reactions.[404] For example, Parlett *et al.* investigated the effect of support architecture on Pd-catalyzed aerobic selective oxidation of sterically challenging allylic alcohols over hierarchically ordered macro/mesoporous silica systems fabricated using pluronic (P123) and polystyrene (PS) colloids as respective meso- and macropore directing agents (Fig. 25).[356] The hierarchically porous Pd NP/macro-meso-$SiO_2$ structures outperformed mesoporous analogues by dramatically improving in-pore diffusion and access to active sites containing well-stabilized palladium oxide NP.

Mass transport within CBPM is particularly useful for biomass conversion. Biomass conversion into fuel and chemicals is becoming increasingly popular as a way to diversify energy sources. It is estimated that biomass could provide about 25% of global energy requirements.[329,405,406] Agricultural crops, waste from food processing, litter from animal feedlots and many other sources of biomass can be converted into fuel gas, bio-alcohol, or biodiesel, or into a syngas from which chemicals and fuels can be synthesized. Biodiesel in particular has emerged as one of the best potential renewable energy sources to replace current petroleum-based transportation fuel.[329] Although recent studies have proven the environmental and economical benefits of biodiesel production *via* heterogeneous catalysis, it remains challenging to develop suitable heterogeneous catalyst architectures that will facilitate the diffusion of viscous bio-oil feedstock during catalytic conversion. Most materials described to date exhibit micro and/or mesoporosity, which are not optimal for accommodating bulky triglyceride derivatives. In this respect, colloid-templated hierarchical macro/mesoporous materials are good candidates. For example, hydrotalcites (HTs) have been used in the fabrication of colloid-based macroporous structures for the transesterification of triglycerides with methanol.[354] HTs are a class of naturally occurring, solid base catalyst materials

**306** | *Chem. Soc. Rev.*, 2016, **45**, 281–322

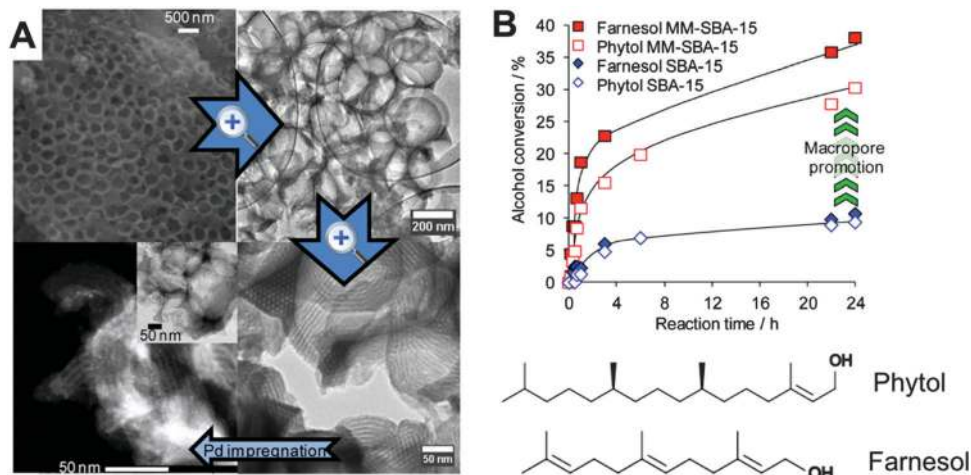This journal is © The Royal Society of Chemistry 2016

**Fig. 25** Hierarchically ordered colloid-based macro/mesoporous (MM) silica (SBA-15) structures loaded with Pd NP (Pd/MM-SBA-15) demonstrate enhanced catalytic activity in the aerobic selective oxidation of bulky allylic alcohols to their aldehydes. (A) SEM and TEM images of MM-SBA-15 and corresponding 0.78 wt% Pd/MM-SBA-15. (B) Impact of interconnected macroporosity on the oxidation of farnesol and phytol over Pd/MM-SBA-15 *versus* Pd/SBA-15.[356] Reused with permission from the American Chemical Society, copyright 2013.

possessing layered double hydroxide structures, with the general formula $[[M(II)_{1-x}M(III)_x(OH)_2]^{x+}(A^{n-}_{x/n})mH_2O]^{x+}$, where $0.17 < x < 0.33$. These materials are considered good candidates for biodiesel formation under mild conditions due to their high activity and robustness in the presence of water and fatty acids.[407] It was demonstrated that HTs with a macroporous–mesoporous architecture have superior mass-transport characteristics leading to exceptional performance.[355]

**Order and periodicity.** Depending on the specific catalytic reaction, the degree of structural perfection and long-range order can have varying importance. While structural order and photonic aspects were found to play a significant role in the enhancement of photocatalytic efficiency, the requirements for structural perfection are much less strict for other catalytic systems. Nevertheless, the regularity of the structures can improve catalytic properties and contribute to better quantitative modeling of catalytic behavior.

Compared to disordered porous structures, inverse opal-based photocatalyst systems provide not only high surface area, but also exhibit many optical properties desirable for photocatalytic enhancement, such as a photonic stopband, light scattering, and slow photon effects. Harvesting and conversion of solar energy into chemical energy using photocatalysts is one of the most promising strategies toward the development of renewable energy technologies, environmental protection, and remediation.[330,408] Two key requirements of efficient photocatalysts are: (i) effective harvesting of solar energy, and (ii) facile separation and transportation of charge carriers. Inverse opal structures have been extensively investigated for photocatalytic applications in recent years and a number of reviews have been published;[64,330,346,401] most studies have focused on semiconductor photocatalysts for water splitting, degradation or oxidation of organic contaminants, and $CO_2$ conversion (Table 1).

Among semiconductor metal-oxide photocatalysts, titania ($TiO_2$) has been the most investigated photocatalytic material due to its high reactivity, low cost, chemical stability and non-toxicity.[408] The enhanced photocatalytic activity in $TiO_2$ inverse opals has been demonstrated for efficient photodegradation of various organic compounds[362,364–366] and stems from enhanced absorption due to the "slow photon" effect, where certain wavelengths of light near the photonic peak spend more time in the structure. In addition, the synergy of the slow photon effect and the hierarchically porous structure of the inverse opal itself results in even higher photocatalytic activity due to enhanced surface area.[363,409] Recently, enhanced photocatalytic activity for degradation of organic compounds has been demonstrated in highly ordered meso/macroporous silica inverse opals impregnated with $TiO_2$ nanoparticles.[367]

Ordered macroporous structures for photo-induced solar fuel production, such as hydrogen from water splitting, have received much attention in recent years (Table 1). Typically, the semiconductor is incorporated into a photoelectrochemical cell or used as a powder suspended in solution. Many studies demonstrated that the inverse opal morphology has a profound effect on photoelectrocatalytic performance. Various semiconductor photoanode materials with inverse opal structures have been used (Table 1). For example, Zhou *et al.* demonstrated enhancement in the photocurrent density and photoelectrochemical water splitting efficiency for 3D ordered macroporous $Mo:BiVO_4$ inverse opal structures as compared to the porous but disordered counterpart (Fig. 26).[25] This enhancement was attributed to the synergistic effects of compositional and structural optimization, leading to an improvement in charge transport properties.

### 6.2 Perspective

Regardless of the specific catalytic application, CBPM architecture is an important but somewhat unexplored parameter in the field of heterogeneous catalysis. In general, much better catalytic performance was demonstrated for ordered CBPM, inverse opals, than for their disordered macroporous, mesoporous and bulk counterparts in various catalytic reactions,
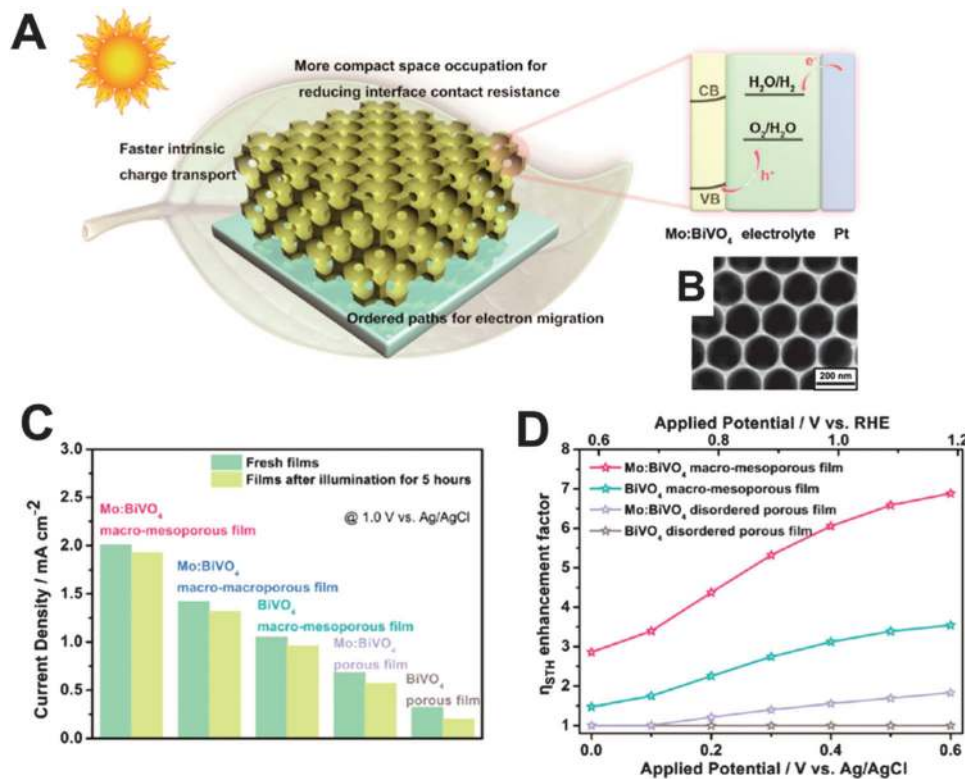
This journal is © The Royal Society of Chemistry 2016

*Chem. Soc. Rev.*, 2016, **45**, 281–322 | **307**

Fig. 26  Inverse opals for electrochemical water splitting. (A) Ideal schematic representation of the expected advantages of integrative Mo:BiVO$_4$ macro-mesoporous photoelectrodes. (B) SEM image (top view) of Mo:BiVO$_4$ inverse opal. (C) Photocurrent density stability of various films at 1.0 V vs. Ag/AgCl. The films for measurement are before illumination, and after illumination for 5 h, respectively. (D) Enhancement factors of solar-to-hydrogen conversion efficiencies ($\eta_{STH}$).[25] Reproduced with permission from the American Chemical Society, copyright 2014.

especially in the liquid phase. The use of the unique properties of CBPM in different areas of catalysis is somewhat uneven. Hundreds of reports have been published on their photocatalytic applications in the past few years, while only a few reports exist on their utilization as catalytic supports in biomass upgrading. Given their superior structural properties for mass transport, it is surprising that the use of CBPM as catalyst supports is not more widespread in liquid phase catalytic processes involving bulky molecules. For example, in biomass transformation, the design of pore networks with interconnecting macro and mesoporous channels has clear beneficial effects on reaction rates by improving in-pore diffusional properties and therefore should be further pursued. Moreover, the surface functionalization of CBPM using enzymes to improve selectivity is a largely unexplored area.[410–412]

Practical applications of CBPM and their more widespread use will require more systematic studies and optimization of fabrication processes to address challenges in large-scale fabrication. The conventional synthesis of CBPM involves the infiltration of a matrix material, typically a sol–gel solution of a metal-oxide precursor, into a sacrificial colloidal crystal template, followed by its removal to produce an inverse inorganic porous material. This conventional infiltration method does produce highly ordered structures at small scales, but also generates a number of defects such as cracks, domain boundaries and over-layer coatings at larger length scales. While for

some catalytic applications long-range order is less important for efficient performance, the fabrication of crack-free, ordered domains over significantly large areas is crucial for photocatalytic applications. Vapor phase deposition (such as atomic layer deposition) avoids the problems of liquid infiltration, but is time consuming and expensive. Some efforts have been made to control the cracking and domain orientation of colloidal crystal films through control of the evaporative deposition conditions, co-assembly methods,[59] and pre-sintering of the particles. However, the fabrication of crack-free inverse opals of arbitrary composition remains a challenge, and further studies should be done to expand the materials space of highly ordered structures.

Regardless of the importance of structural perfection, low quality, disordered CBPM can complicate their quantitative comparison with non-structured or mesoporous/microporous analogues. In addition, fabrication of dispersible CBPM (*e.g.* spherical photonic micro-particles) can be beneficial for many catalytic applications and is largely unexplored.[363,401,413]

The control over metal NP size, distribution, and stability using a simple synthetic approach represents an additional challenge. Non-uniform distribution of functional particles can result in the formation of hot spots and compromise the uniform distribution of temperature and concentration profiles in the reactor channel. Loosely bound metal NPs will reduce catalyst durability. Different strategies of metal NP immobilization have

308 | *Chem. Soc. Rev.*, 2016, **45**, 281–322

This journal is © The Royal Society of Chemistry 2016

been developed including impregnation, adsorption based on electrostatic interaction, *in situ* synthesis, or co-assembly with metal oxide precursors. The post-modification methods, such as impregnation or adsorption of preformed metal NPs, generates structures with uniform, high accessibility metal NPs. However, they are not very stable and are prone to sintering, especially in high-temperature catalytic reactions. In addition, the presence of capping ligands used for metal NP stabilization is undesirable for catalytic applications, and they often must be removed by annealing treatments, which generally results in loss of diameter control due to particle agglomeration. Oxidative removal (ozone treatment) can lead to changes in the surface chemistry of the metal. In addition, to achieve high loading, pre-immobilization treatment is required (*e.g.* oxidative or thermal activation or surface functionalization to introduce a chemical linker group). Co-assembly and *in situ* methods produce much more stable metal NP systems, but suffer from non-uniform size and low accessibility.

Nevertheless, these results highlight the significance of colloid-based ordered macro-mesoporous architectures as promising catalytic systems. In particular, the compositional and morphological control of CBPM provides the ability to create more purpose-designed catalysts with highly efficient performance.

# 7. Electrode applications

Electrochemical processes are fundamental to a vast range of applications, particularly for energy storage and conversion. Because electrochemistry occurs at the interface of an electrode and an electrolyte, the electrode geometry has a large influence on rates and capacities. Using CBPM, the geometry and composition can be controlled across multiple length scales, providing an excellent handle over electrode geometry for various electrode applications such as capacitors, batteries, fuel cells, and solar cells.

Capacitors and batteries both store electrical energy. Capacitors or supercapacitors rapidly store and release energy by separating charge across a dielectric or electrolyte. Higher energy storage is possible with higher capacitance values, but the capacitance is dependent on the two electrodes having large surface area and short separation distances between them. Batteries also store energy, by moving electrons from the negative electrode to the positive electrode; however, in batteries, the energy is stored in chemical bonds rather than in the electric field. Thus, a chemical change is incorporated, such as $Li^+$ intercalating into transition metal compounds in Li-ion batteries. During discharge, this chemical energy is released, reforming the initial compounds and producing a current.

While capacitors and batteries store electric energy, fuel cells and solar cells instead generate electric current by converting other forms of energy. In a fuel cell, a chemical fuel is consumed to produce the current, much like during discharge of a primary (non-rechargeable) battery. In solar cells, absorbed light is converted into electric current; in dye-sensitized solar cells (DSSC), light absorption is enhanced by adding a photosensitizer such as a dye molecule to the semiconductor surface. Photoelectrochemical cells, a type of catalyst system, take this one step further by converting the incident light energy into chemical bonds for storage.

All of these applications are summarized in Table 2. Because they are based on electrochemical processes, they necessitate the need for control over the electrode structure on the 10 nm and 100 nm scale,[414] making CBPM ideal candidates.

There are three key advantages of CBPM for making electrodes for applications: high surface area, interconnected porosity, and visible light control. These factors apply to all CBPM and are shown schematically in Fig. 27 for inverse opals in particular. For example, with a high surface area (Fig. 27A) with controlled composition, high charging rates can be maintained in capacitors, and short charge transport distances are possible.[458] The macroporosity (Fig. 27B) is useful for ion diffusion through the structure, especially in batteries.[458] Additionally, because active battery materials can undergo large volume changes, macropores allow the material to expand without breaking the structure. Finally, the length scale is commensurate with the wavelength of visible light, allowing these colloidal materials to be used for increasing photon absorption in solar cells. Enhanced absorption can stem from the photonic nature of an ordered structure (Fig. 27C) or from increased scattering in a disordered structure. Additionally, these features can all be combined in hierarchical structures using colloids. These advantages will be discussed in more detail below.

While Fig. 27 shows inverse, ordered structures, disordered and direct structures have also been investigated. Colloid-based

**Table 2** Comparison of various electrodes that can be made with CBPM

| Electrode type | Surface area?[a] | Porosity?[a] | Order?[a] | Energy input | Energy output | Critical factor | Ref. |
|---|---|---|---|---|---|---|---|
| Capacitor | ✔✔ | ✔ | ✘ | Electrical | Electrical | Surface area | 58, 73, 415, 417, 418 |
| Battery | ✔ | ✔✔ | ✘ | Chemical (discharge) | Electrical (discharge) | Diffusion | 26, 62, 68, 74, 420–431, 464–466 |
| Fuel cell | ✔✔ | ✔✔ | ✘ | Chemical | Electrical | Diffusion | 58, 433, 434 |
| Solar cell | ✔✔ | ✔ | ✔ | Light | Electrical | Charge separation | 58, 65–67, 71, 72, 201, 393, 432, 435–439, 441–447, 449–457, 462 |

[a] For each type, the importance of various attributes of CBPM are noted as either very important (✔✔), important (✔), or not important (✘). Additionally, the energy input and output for each type is listed as well as their function.

This journal is © The Royal Society of Chemistry 2016

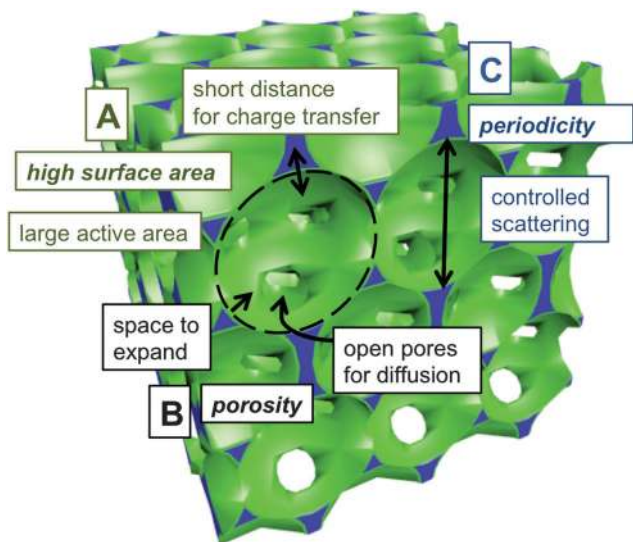*Chem. Soc. Rev.*, 2016, 45, 281–322 | 309

Fig. 27 Schematic of double-layer inverse opal illustrating the key advantages of CBPM in electrode applications: (A) high surface area, (B) porosity, and (C) periodicity.

electrodes are generally templated (*i.e.* inverse structures) because inverse structures have larger pores, better pore interconnectivity, and improved mechanical stability. Using block copolymers to make mesoporous materials,[429,430] the surface area can be further increased. Charge transport generally occurs across 1–10 nm, so the structure on the 100 nm scale less important; however, ordered structures ensure that the pores are fully interconnected for ion diffusion. Additionally, ordered structures provide a good model system to study different properties (*e.g.* diffusion),[459,460] and can provide additional photon management for solar cells.[448,461] The pore size can be another handle on controlling the properties, especially for diffusion. Due to the nature of electrodes, primarily three-dimensional structures are grown on supports rather than making free-standing superparticles.

One final advantage that underpins the desirable macroporous structure is the high degree of compositional tunability of colloid-based structures. Electrochemical cells rely on different material compositions for their conductivity, insulating nature, or electroactivity (for catalysis or intercalation). Indeed, the electrode composition determines its use as an electrode, with a vast materials space possible spanning transition metal oxide intercalation compounds,[428,430] metals,[65] other conductors,[441,462] polymers,[420,436] and semiconductors.[76,442,452] Hierarchical structures can be also made, for example with a conducting matrix and either conformal growth of an active layer[71,74,419,425,426] or embedded additives such as functional catalysts[433] or electroactive[62] nanoparticles.

### 7.1 Factors influencing electrode applications

**Composition and surface area.** One of the primary reasons hierarchical CBPM are used as electrodes is their high surface area, with a higher active area for a given volume of material. High surface area allows for easy access to active materials in

batteries[421,423,426,428–431] and fuel cells,[433] improving energy density. It also leads to higher dye loading, and thus increased light absorption and higher rates, in dye-sensitized solar cells.[65,440] The surface area was further taken advantage of by Ergang *et al.* in their fabrication of an electrode consisting of a conducting matrix with a conformal electrolyte layer.[426] Because the cathode consisted of a gel, it could then be infiltrated into the structure, forming an interpenetrating cell with high surface area and extremely short diffusion distance between the anode and cathode. Mesoporous structures have been used as well, either in a hierarchical meso–macroporous architecture,[463] or a mesoporous–macroporous bilayer,[67,452] to achieve even higher surface area.

High surface area structures generally have long charge transport distances, leading to increased recombination. CBPM can also achieve short electron transport distances even in high surface area structures,[341] particularly with inverse structures, by controlling the hierarchical composition. Generally, high surface area structures have large separation between where charge is collected and where it is generated, as well as many grain boundaries, making recombination more likely to occur. For example, high surface area in solar cells can improve the rate, but it can also lead to increased recombination.[438] The simple fabrication methods of CBPM allow one to make mixed structures, for example a conducting matrix with embedded active particles,[62,464] as shown in Fig. 28. Because the nanoparticles are fully embedded in the matrix, they do not dislodge from the structure, and the efficiency is stable even after hundreds of cycles (Fig. 28B).[62] Alternatively, active electrode materials can easily be grown on conducting supports to produce a layered structure,[26,415,416,425,465] as shown in Fig. 29. With hierarchical structures, the charge can quickly travel from the active site to the conducting matrix, where it can be collected before recombination. Small transport distances have been found to decrease charge recombination in solar cells,[450,451] enhancing current output.

**Macroporosity.** While the composition of CBPM can provide control over electron transfer processes, the porosity can allow for the simultaneous control of ion diffusion.[341,458] Much like for catalysis, the macroporous structure of CBPM provides for easier diffusion to the active surface; in electrodes, fast ion diffusion means faster charging and reaction rates.[430] Ordered, inverse structures have been particularly well investigated as a means of controlling ion transport, for example in Li-ion batteries,[26,428,466] Li-air batteries,[431] dye-sensitized solar cells (DSSC),[450] and fuel cells.[433] These colloid-templated structures have also been used as separators in batteries[420] and fuel cells[434] due to their ability to control ion diffusion. Capacitors also benefit from the control over diffusion, because high surface area increases the capacitance, but it can also cause very high charging times. Inverse opal capacitors can be made with a controllable balance between accessible high surface area and charging time.[73,417] In addition to specific applications, inverse opal structures have been used as a model system for studying diffusion in nano-to-micro pores,[459,460] which will undoubtedly be important when designing future CBPM-based electrodes. When considering this control over diffusion, the amount of cracks is also important since they can introduce other diffusion pathways.
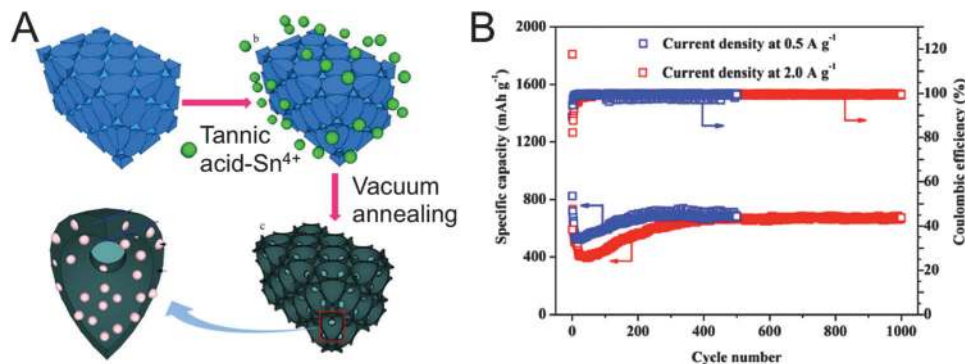
310 | *Chem. Soc. Rev.*, 2016, **45**, 281–322

This journal is © The Royal Society of Chemistry 2016

**Fig. 28** Nanoparticle additives lead to close contact between the electroactive material and the conductor. (A) Schematic illustrating the fabrication of a carbon inverse opal with embedded electroactive $SnO_2$ nanoparticles for Li-ion batteries, and (B) their specific capacity and coulombic efficiency, which remain stable after hundreds of cycles.[62] Reproduced with permission from Nature Publishing Group, copyright 2013.
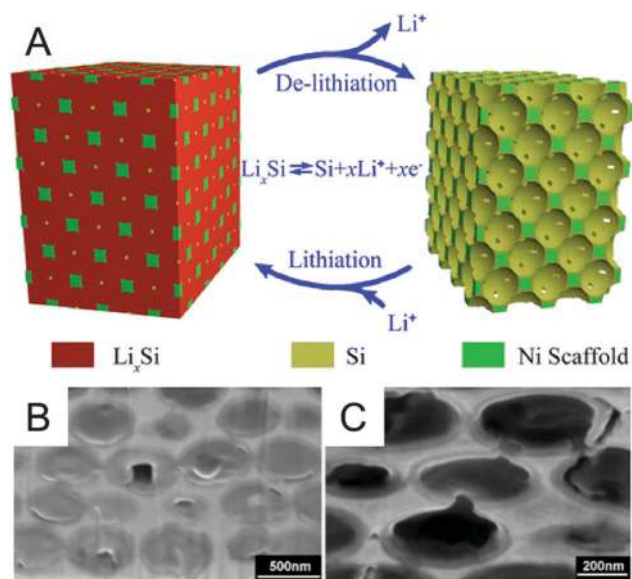


**Fig. 29** Swelling of an electroactive coating material does not lead to disruption of the macroporous structure of an inverse opal. (A) A nickel inverse opal with a conformal silicon layer shown schematically; (B and C) SEM images showing that (B) upon lithiation, the $Li_xSi$ fills the pores but the structure remains intact, and (C) after delithiation, the structure remains.[425] Reproduced with permission from the American Chemical Society, copyright 2012.

Beyond diffusion, the macroporosity has an added benefit for battery electrode stability because the structure can undergo large volume changes without degradation. In lithium-based batteries in particular, large volume changes are associated with the lithiation and delithiation of the electrode materials.[68,74,427] Swelling and shrinking can lead to loss of structural integrity and battery failure. Several groups have investigated using inverse opals to avoid this degradation, especially for $MnO_2$[465] and $MnSiO_4$[464] positive electrodes and silicon negative electrodes[74,425,427] in Li-ion batteries, as well as for sulfur in Li–S batteries.[68] These studies describe hierarchical structures, where a conducting matrix is covered with an active material. This active material can then swell into the pores without deforming the contact to the rest of the battery. For example, in Fig. 29, a nickel matrix is coated with an electroactive silicon layer. During lithiation, the silicon

swells and fills the pores; when $Li^+$ is released during discharge, silicon shrinks back and the structure reappears. Inverse structures are used due to their macroporosity, but the effects of parameters such as pore size and degree of order have not been investigated and would yield important insights into the ideal structure.

**Order and periodicity.** The 100 nm length scale of colloidal materials provides a handle for controlling visible light absorption in solar cells and for photoelectrochemistry.[75,365,448,461,463] For example, several groups have investigated using photonic enhancement from ordered inverse opal structures in both semiconductor and dye-sensitized solar cells (DSSC).[65,436,442,443,452,456,457] In a photonic crystal such as an inverse or direct opal, light near the photonic bandgap has increased absorption due to a longer lifetime in the structure.[467] This additional absorption can improve the efficiency. For example, it accounted for a >50% increase in the efficiency of a DSSC,[447] and can be seen clearly in Fig. 30 for a photoanode made from $WO_3$, where the efficiency varies as a function of wavelength depending on the periodicity of the structure.[393] There is a clear efficiency enhancement for the structure made with 200 nm colloids, which has a photonic bandgap overlapping with the electronic absorption of $WO_3$. In addition to ordered structures for increased absorption of certain wavelengths, disordered structures can be used to increase scattering of all wavelengths,[71] which also improves absorption by increasing the path length in the structure.

**Patterning and hierarchical structures.** Using colloidal patterning techniques, more complicated electrode structures can be made. For example, interdigitated microbatteries are possible where the anode and cathode alternate on the scale of tens of microns (Fig. 31).[26] Using patterning, Pikul *et al.* achieved Li-ion batteries with extraordinary energy and power densities. CBPM have also been used as separators in batteries[420] and fuel cells,[434] where they were grown within the confines of the other layers of the cells.

The vast majority of studies of CBPM electrodes have focused on controlling the 10–100 nm scale since electrochemical phenomena such as charge transfer and diffusion generally occur on this scale. However, in actual cells, the proximity of the anode and cathode are important. Patterning CBPM electrodes
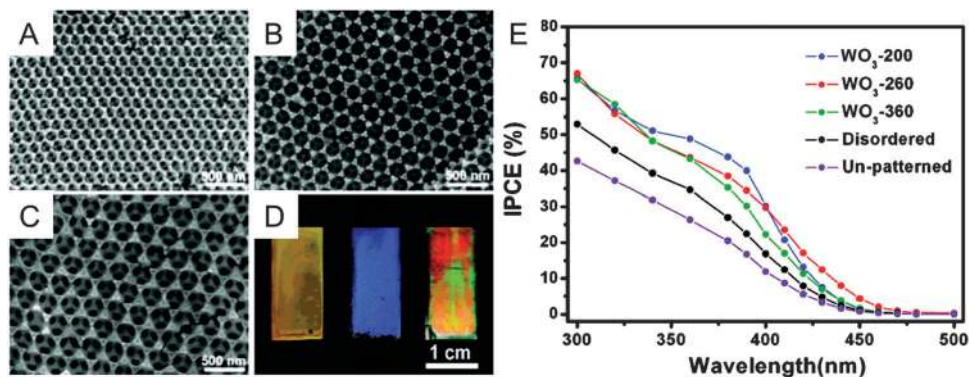
**Fig. 30** Photonic crystal effects enhance efficiency in photoanodes. (A–C) SEM images of $WO_3$ inverse opals made from different sizes of colloids. (D) Optical image of the inverse opals shown in (A–C). (E) Incident photon-to-electron conversion efficiency (IPCE) of the inverse opals, compared to disordered and unpatterned structures. $WO_3$-200, $WO_3$-260, and $WO_3$-360 correspond to $WO_3$ inverse opals made from 200 nm, 260 nm, and 360 nm colloids, respectively.[393] Reproduced with permission from the American Chemical Society, copyright 2011.
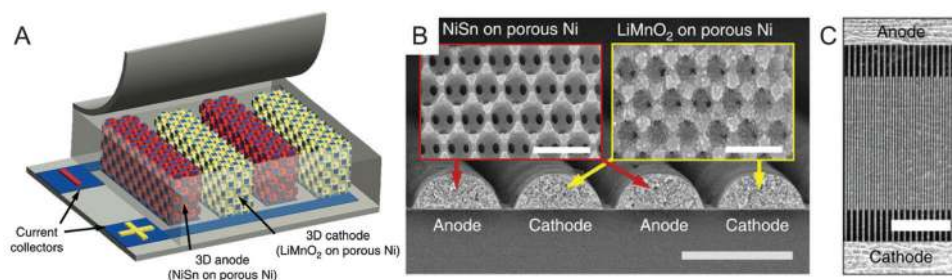


**Fig. 31** Patterning of interdigitated inverse opal electrodes. (A) Schematic, and (B) SEM image of interdigitated microbattery electrode structure with alternating materials (scale bar 50 μm; inset scale bars 1 μm). (C) Larger scale SEM image showing a top-down view of the structure (scale bar 500 μm).[26] Reproduced with permission from Nature Publishing Group, copyright 2013.

are a promising and relatively unexplored area; for example, superparticles could be used to make even more complex patterns with easy transport between the two electrodes.

## 7.2  Perspective

CBPM not only have both high surface area and porosity, but their unique structure combining the two allows for both fast ion diffusion and fast electron transport.[26,62,427] High charging and discharging rates stem from the high surface area and short distance between the active area and the conducting support. With limited tortuosity, ion diffusion is facile and controllable, with the added benefit of being able to undergo volume changes without loss of structural integrity. For solar cells, scattering and photonic effects also improve the efficiency. Furthermore, the tailorability of colloid-based materials allows complicated structures to be made fairly easily, whether with electrodeposition or additives. Multiple parameters can be controlled simultaneously, across the material composition as well as the structure. These factors are especially important in electrodes, where the composition and hierarchical composite structure are integral to the function. For these reasons, CBPM have been investigated for many electrochemical energy storage and conversion applications, with much success; however, good comparisons are challenging because adequate controls are often not included, for example to compare the benefits of a

specific structure or hierarchical composition to a similar, flat substrate, or to a similar structure missing one aspect of the composition. One area that hasn't been fully developed is to pattern CBPM for electrode applications, which opens up a variety of interesting possibilities for hierarchical electrochemical cells, for example microbattery architectures.[468]

Compared to hierarchical colloid-based materials, most other methods are either more expensive or offer less control. Much of this text has described the advantages of porous, high surface area structures in general; for example, nanostructured DSSC electrodes not based on colloids can have very high surface area. However, many of these high surface area architectures generally suffer from high recombination rates. Comparing to other porous structures not based on colloids, the benefits are less clear. For battery electrodes, there are many other porous materials in use for electrodes, such as porous carbon and nanoporous gold, which can easily achieve hierarchical compositions using electrodeposition. However, the "pore" size of these structures is fixed and functionalization with nanoparticles requires a second step. Nanoporous gold is also more expensive.

In order for CBPM to compete with existing porous materials, improvements in the fabrication methods must be considered. Most of these electrode applications would require inexpensive fabrication methods to be cost-effectively scaled up to the necessary scale. Certain fabrication methods, such as electrodeposition, are

easy to scale up, whereas others, such as ALD, are not. Disordered structures are faster and easier to make, but most basic research to date has centered on ordered structures. These ordered structures are ideal for model studies, for example to investigate the effect of the size scale of porosity on different aspects of performance; understanding the underlying chemistry and physics will allow us to target a specific size for scaled-up versions. However, a better understanding of phenomena such as ion diffusion in disordered structures will also be critical.

Because composition is so important for electrode function, expanding the materials space will allow for new applications. New electrode materials for Li-ion batteries are constantly emerging, for example $ZnCo_2O_4$.[469] New battery types are also being investigated such as Li–air and Zn–air,[470] and new compositions are necessary to be used in these applications. Assembly strategies for making crack-free structures of arbitrary composition with hierarchical architecture will require a better understanding of the underlying mechanisms of crack-free structure formation. Crack-free structures can be made by co-assembling a silica matrix with the colloidal crystal,[59] but this method remains to be adequately expanded to other materials. Future electrodes will have a porous structure and hierarchical composition with good reproducibility and durability; the benefits of CBPM for introducing these characteristics are a huge advantage if various compositions can be made reliably.

## 8. Conclusions

Biology uses structuration on the nano to the macroscale to achieve functions beyond the inherent properties of its limited materials scope. Using colloids, similar structural features can be made synthetically, with a variety of assembly methods producing structures beyond those found in nature. These structures give rise to a variety of functionalities not present in the individual colloidal particles, rendering such self-assembled materials attractive for a diverse range of applications, in particular optics, wetting, sensing, catalysis, and electrodes.

CBPM can be made for many applications with controlled composition, porosity, periodicity, order, and hierarchy. Different application fields vary in their desired properties, but the modularity of the assembly process provides a high degree of tunability and tailorability in the composition and structure, opening the door for many potential commercial products. In terms of composition, functional particles can easily be added at various locations in the CBPM structure due to the modularity of the fabrication methods. These particles can act as optical absorbers, catalysts, or electroactive materials. Additionally, the surface can be modified with various functionalities, which is particularly useful for wetting and sensing applications. The degree of order and periodicity determine most optical effects, which can subsequently be used as sensors that rely on a colorimetric readout. Moreover, the order is intimately connected to the porosity, as the degree of order can affect the tortuosity and interconnection of the porous network. The interconnection is especially important for

diffusion in heterogeneous catalysis and electrodes. The porosity also influences fluid transport, whether within the structure or on the surface for repellency. CBPM allow for precise control over these aspects, but comparative studies highlighting advantages over other types of porous structures are still rare.

Using hierarchical and patterned structures, complex features can be created for advanced applications. For example, multiple sensing responses can occur on a single chip,[260] or complete microbatteries can be assembled.[26] Complex optical effects can be achieved by combining features on different length scales, for example if stopband effects were combined with grating diffraction, all in a patterned structure. With many patterning techniques, the hierarchy can be tailored to the specific application.

Colloids can be used in a variety of areas, but scaling up the fabrication process is a major roadblock to commercialization, particularly of ordered structures. At a lab-scale, colloidal assemblies are unchallenged in their ability to provide precise model systems to develop design guidelines for the optimization of a desired macroscopic property. Future work should focus on scaling up methods of producing high quality structures of various types, including both superparticles and crack-free templated structures of arbitrary composition, on an industrial scale beyond typical "large scale" assembly methods. Superparticles are already showing promise to solve the scale-up problem, and they are particularly useful for their ability to be transported as a powder and dispersed in a variety of media.

Finally, many biological colloidal structures achieve multifunctionality, optimizing for multiple properties simultaneously, for example optical effects, wetting characteristics, and mechanical stability.[12] To date, there are limited synthetic multifunctional structures, but we expect that this research area will provide a variety of novel materials in the future.

## Acknowledgements

## References

1 R. O. Prum, R. Torres, S. Williamson and J. Dyck, *Proc. R. Soc. B*, 1999, **266**, 13–22.
2 Q. Li, K.-Q. Gao, J. Vinther, M. D. Shawkey, J. A. Clarke, L. D'Alba, Q. Meng, D. E. G. Briggs and R. O. Prum, *Science*, 2010, **327**, 1369–1372.

This journal is © The Royal Society of Chemistry 2016

*Chem. Soc. Rev.*, 2016, **45**, 281–322 | 313

3   E. R. Dufresne, H. Noh, V. Saranathan, S. G. J. Mochrie, H. Cao and R. O. Prum, *Soft Matter*, 2009, **5**, 1792.

4   J. D. Forster, H. Noh, S. F. Liew, V. Saranathan, C. F. Schreck, L. Yang, J. G. Park, R. O. Prum, S. G. Mochrie, C. S. O'Hern, H. Cao and E. R. Dufresne, *Adv. Mater.*, 2010, **22**, 2939–2944.

5   M. D. Shawkey and G. E. Hill, *J. Exp. Biol.*, 2006, **209**, 1245–1250.

6   J. Teyssier, S. V. Saenko, D. van der Marel and M. C. Milinkovitch, *Nat. Commun.*, 2015, **6**, 6368.

7   J. Zhang, J. Wang, Y. Zhao, L. Xu, X. Gao, Y. Zheng and L. Jiang, *Soft Matter*, 2008, **4**, 2232.

8   J. Zhang, X. Sheng and L. Jiang, *Langmuir*, 2009, **25**, 1371–1376.

9   K. Liu, X. Yao and L. Jiang, *Chem. Soc. Rev.*, 2010, **39**, 3240–3255.

10  W. Barthlott and C. Neinhuis, *Planta*, 1997, **202**, 1–8.

11  S. Vignolini, P. J. Rudall, A. V. Rowland, A. Reed, E. Moyroud, R. B. Faden, J. J. Baumberg, B. J. Glover and U. Steiner, *Proc. Natl. Acad. Sci. U. S. A.*, 2012, **109**, 15712–15715.

12  L. Li, S. Kolle, J. C. Weaver, C. Ortiz, J. Aizenberg and M. Kolle, *Nat. Commun.*, 2015, **6**, 6322.

13  M. Kolle, P. M. Salgard-Cunha, M. R. J. Scherer, F. Huang, P. Vukusic, S. Mahajan, J. J. Baumberg and U. Steiner, *Nat. Nanotechnol.*, 2010, **5**, 511–515.

14  P. Vukusic, J. R. Sambles, C. R. Lawrence and R. J. Wootton, *Proc. R. Soc. B*, 1999, **266**, 1403–1411.

15  K. Chung, S. Yu, C. J. Heo, J. W. Shim, S. M. Yang, M. G. Han, H. S. Lee, Y. Jin, S. Y. Lee, N. Park and J. H. Shin, *Adv. Mater.*, 2012, **24**, 2375–2379.

16  G. England, M. Kolle, P. Kim, M. Khan, P. Munoz, E. Mazur and J. Aizenberg, *Proc. Natl. Acad. Sci. U. S. A.*, 2014, **111**, 15630–15634.

17  F. Barthelat, H. Tang, P. Zavattieri, C. Li and H. Espinosa, *J. Mech. Phys. Solids*, 2007, **55**, 306–337.

18  X. Li, Z. H. Xu and R. Wang, *Nano Lett.*, 2006, **6**, 2301–2304.

19  G. M. Whitesides and B. Grzybowski, *Science*, 2002, **295**, 2418–2421.

20  M. J. Robb, S. Y. Ku and C. J. Hawker, *Adv. Mater.*, 2013, **25**, 5686–5700.

21  M. Stefik, S. Guldin, S. Vignolini, U. Wiesner and U. Steiner, *Chem. Soc. Rev.*, 2015, **44**, 5076–5091.

22  D. P. Josephson, M. Miller and A. Stein, *Z. Anorg. Allg. Chem.*, 2014, **640**, 655–662.

23  J.-Y. Shiu, C.-W. Kuo, P. Chen and C.-Y. Mou, *Chem. Mater.*, 2004, **16**, 561–564.

24  C. G. Schafer, D. A. Smolin, G. P. Hellmann and M. Gallei, *Langmuir*, 2013, **29**, 11275–11283.

25  M. Zhou, J. Bao, Y. Xu, J. Zhang, J. Xie, M. Guan, C. Wang, L. Wen, Y. Lei and Y. Xie, *ACS Nano*, 2014, **8**, 7088–7098.

26  J. H. Pikul, H. Gang Zhang, J. Cho, P. V. Braun and W. P. King, *Nat. Commun.*, 2013, **4**, 1732.

27  Y. N. Xia, B. Gates, Y. D. Yin and Y. Lu, *Adv. Mater.*, 2000, **12**, 693–713.

28  W. D. Harkins, *J. Am. Chem. Soc.*, 1947, **69**, 1428–1444.

29  J. W. Goodwin, J. Hearn, C. C. Ho and R. H. Ottewill, *Colloid Polym. Sci.*, 1974, **252**, 464–471.

30  S. Jiang, E. D. Sudol, V. L. Dimonie and M. S. El-Aasser, *J. Appl. Polym. Sci.*, 2008, **108**, 4096–4107.

31  C. M. Tseng, Y. Y. Lu, M. S. El-Aasser and J. W. Vanderhoff, *J. Polym. Sci., Part A: Polym. Chem.*, 1986, **24**, 2995–3007.

32  K. D. Hartlen, A. P. Athanasopoulos and V. Kitaev, *Langmuir*, 2008, **24**, 1714–1720.

33  W. Stöber, A. Fink and E. Bohn, *J. Colloid Interface Sci.*, 1968, **26**, 62–69.

34  Q. Chen, S. C. Bae and S. Granick, *Nature*, 2011, **469**, 381–384.

35  F. Wurm and A. F. Kilbinger, *Angew. Chem., Int. Ed.*, 2009, **48**, 8412–8421.

36  H. Bao, W. Peukert and R. Klupp Taylor, *Adv. Mater.*, 2011, **23**, 2644–2649.

37  H. Bao, T. Bihr, A. S. Smith and R. N. Klupp Taylor, *Nanoscale*, 2014, **6**, 3954–3966.

38  Y. Wang, Y. Wang, D. R. Breed, V. N. Manoharan, L. Feng, A. D. Hollingsworth, M. Weck and D. J. Pine, *Nature*, 2012, **491**, 51–55.

39  G. R. Yi, D. J. Pine and S. Sacanna, *J. Phys.: Condens. Matter*, 2013, **25**, 193101.

40  R. Contreras-Cáceres, J. Pacifico, I. Pastoriza-Santos, J. Pérez-Juste, A. Fernández-Barbero and L. M. Liz-Marzán, *Adv. Funct. Mater.*, 2009, **19**, 3070–3076.

41  A. Guerrero-Martinez, J. Perez-Juste and L. M. Liz-Marzan, *Adv. Mater.*, 2010, **22**, 1182–1195.

42  N. Vogel, C. Fernandez-Lopez, J. Perez-Juste, L. M. Liz-Marzan, K. Landfester and C. K. Weiss, *Langmuir*, 2012, **28**, 8985–8993.

43  A. H. Groschel, F. H. Schacher, H. Schmalz, O. V. Borisov, E. B. Zhulina, A. Walther and A. H. Muller, *Nat. Commun.*, 2012, **3**, 710.

44  A. H. Groschel, A. Walther, T. I. Lobling, F. H. Schacher, H. Schmalz and A. H. Muller, *Nature*, 2013, **503**, 247–251.

45  D. Klinger, C. X. Wang, L. A. Connal, D. J. Audus, S. G. Jang, S. Kraemer, K. L. Killops, G. H. Fredrickson, E. J. Kramer and C. J. Hawker, *Angew. Chem., Int. Ed.*, 2014, **53**, 7018–7022.

46  A. Sanchez-Iglesias, M. Grzelczak, J. Perez-Juste and L. M. Liz-Marzan, *Angew. Chem., Int. Ed.*, 2010, **49**, 9985–9989.

47  A. Dong, J. Chen, P. M. Vora, J. M. Kikkawa and C. B. Murray, *Nature*, 2010, **466**, 474–477.

48  C. B. Murray, C. R. Kagan and M. G. Bawendi, *Annu. Rev. Mater. Sci.*, 2000, **30**, 545–610.

49  U. Jeong, X. Teng, Y. Wang, H. Yang and Y. Xia, *Adv. Mater.*, 2007, **19**, 33–60.

50  B. L. Cushing, V. L. Kolesnichenko and C. J. O'Connor, *Chem. Rev.*, 2004, **104**, 3893–3946.

51  L. M. Liz-Marzan, *Langmuir*, 2006, **22**, 32–41.

52  N. Vogel, C. K. Weiss and K. Landfester, *Soft Matter*, 2012, **8**, 4044–4061.

53  K. Landfester, *Angew. Chem., Int. Ed.*, 2009, **48**, 4488–4507.

54  F. Li, D. P. Josephson and A. Stein, *Angew. Chem., Int. Ed.*, 2011, **50**, 360–388.

55  N. Vogel, M. Retsch, C. A. Fustin, A. Del Campo and U. Jonas, *Chem. Rev.*, 2015, **115**, 6265–6311.

56 O. D. Velev and S. Gupta, *Adv. Mater.*, 2009, **21**, 1897–1905.

57 A. Stein, F. Li and N. R. Denny, *Chem. Mater.*, 2008, **20**, 649–666.

58 A. Stein, B. E. Wilson and S. G. Rudisill, *Chem. Soc. Rev.*, 2013, **42**, 2763–2803.

59 B. Hatton, L. Mishchenko, S. Davis, K. H. Sandhage and J. Aizenberg, *Proc. Natl. Acad. Sci. U. S. A.*, 2010, **107**, 10354–10359.

60 C. I. Aguirre, E. Reguera and A. Stein, *ACS Appl. Mater. Interfaces*, 2010, **2**, 3257–3262.

61 Y. Vasquez, M. Kolle, L. Mishchenko, B. D. Hatton and J. Aizenberg, *ACS Photonics*, 2014, **1**, 53–60.

62 X. Huang, J. Chen, Z. Lu, H. Yu, Q. Yan and H. H. Hng, *Sci. Rep.*, 2013, **3**, 2317.

63 S. T. Kochuveedu, Y. H. Jang and D. H. Kim, *Chem. Soc. Rev.*, 2013, **42**, 8467–8493.

64 T.-D. Nguyen, C.-T. Dinh and T.-O. Do, *Chem. Commun.*, 2015, **51**, 624–635.

65 W. L. Hoffeditz, M. J. Katz, P. Deria, A. B. Martinson, M. J. Pellin, O. K. Farha and J. T. Hupp, *ACS Appl. Mater. Interfaces*, 2014, **6**, 8646–8650.

66 J. W. Lee, J. Lee, C. Kim, C. Y. Cho and J. H. Moon, *Sci. Rep.*, 2014, **4**, 6804.

67 J. W. Lee and J. H. Moon, *Nanoscale*, 2015, **7**, 5164–5168.

68 Z. Liang, G. Zheng, W. Li, Z. W. Seh, H. Yao, K. Yan, D. Kong and Y. Cui, *ACS Nano*, 2014, **8**, 5249–5256.

69 Q. Peng, B. Kalanyan, P. G. Hoertz, A. Miller, H. Kim do, K. Hanson, L. Alibabaei, J. Liu, T. J. Meyer, G. N. Parsons and J. T. Glass, *Nano Lett.*, 2013, **13**, 1481–1488.

70 W. Ren, H. Zhang, D. Kong, B. Liu, Y. Yang and C. Cheng, *Phys. Chem. Chem. Phys.*, 2014, **16**, 22953–22957.

71 N. Tetreault, E. Arsenault, L. P. Heiniger, N. Soheilnia, J. Brillet, T. Moehl, S. Zakeeruddin, G. A. Ozin and M. Gratzel, *Nano Lett.*, 2011, **11**, 4579–4584.

72 V. O. Williams, E. J. DeMarco, M. J. Katz, J. A. Libera, S. C. Riha, D. W. Kim, J. R. Avila, A. B. F. Martinson, J. W. Elam, M. J. Pellin, O. K. Farha and J. T. Hupp, *ACS Appl. Mater. Interfaces*, 2014, **6**, 12290–12294.

73 W. S. Chae, D. V. Gough, S. K. Ham, D. B. Robinson and P. V. Braun, *ACS Appl. Mater. Interfaces*, 2012, **4**, 3973–3979.

74 H. Liu, H. M. Cho, Y. S. Meng and Q. Li, *ACS Appl. Mater. Interfaces*, 2014, **6**, 9842–9849.

75 X. Shi, K. Zhang, K. Shin, J. H. Moon, T. W. Lee and J. H. Park, *Phys. Chem. Chem. Phys.*, 2013, **15**, 11717–11722.

76 J.-P. Zhang and L.-P. Yu, *J. Mater. Sci.: Mater. Electron.*, 2014, **25**, 5646–5651.

77 I. B. Burgess, N. Koay, K. P. Raymond, M. Kolle, M. Loncar and J. Aizenberg, *ACS Nano*, 2012, **6**, 1427–1437.

78 I. B. Burgess, L. Mishchenko, B. D. Hatton, M. Kolle, M. Loncar and J. Aizenberg, *J. Am. Chem. Soc.*, 2011, **133**, 12430–12432.

79 C. M. Parlett, K. Wilson and A. F. Lee, *Chem. Soc. Rev.*, 2013, **42**, 3876–3893.

80 S. Wong, V. Kitaev and G. A. Ozin, *J. Am. Chem. Soc.*, 2003, **125**, 15589–15598.

81 J. Dhainaut, J.-P. Dacquin, A. F. Lee and K. Wilson, *Green Chem.*, 2010, **12**, 296–303.

82 J. F. Galisteo-Lopez, M. Ibisate, R. Sapienza, L. S. Froufe-Perez, A. Blanco and C. Lopez, *Adv. Mater.*, 2011, **23**, 30–69.

83 A. Steele, I. Bayer and E. Loth, *Nano Lett.*, 2009, **9**, 501–505.

84 R. Campos, A. J. Guenthner, A. J. Meuler, A. Tuteja, R. E. Cohen, G. H. McKinley, T. S. Haddad and J. M. Mabry, *Langmuir*, 2012, **28**, 9834–9841.

85 J. Bravo, L. Zhai, Z. Wu, R. E. Cohen and M. F. Rubner, *Langmuir*, 2007, **23**, 7293–7298.

86 F. C. Cebeci, Z. Wu, L. Zhai, R. E. Cohen and M. F. Rubner, *Langmuir*, 2006, **22**, 2856–2862.

87 J. Wang, Q. Li, W. Knoll and U. Jonas, *J. Am. Chem. Soc.*, 2006, **128**, 15606–15607.

88 M. Retsch and U. Jonas, *Adv. Funct. Mater.*, 2013, **23**, 5381–5389.

89 A. R. Hemsley and N. I. Gabarayeva, *Plant Syst. Evol.*, 2006, **263**, 25–49.

90 A. R. Hemsley and P. C. Griffiths, *Philos. Trans. R. Soc., A*, 2000, **358**, 547–564.

91 H. J. Butt, K. Graf and M. Kappl, *Physics and Chemistry of Interfaces*, Wiley-VCH, Weinheim, 2006.

92 D. J. Norris, E. G. Arlinghaus, L. Meng, R. Heiny and L. E. Scriven, *Adv. Mater.*, 2004, **16**, 1393–1399.

93 Q. Li, U. Jonas, X. S. Zhao and M. Kappl, *Asia-Pac. J. Chem. Eng.*, 2008, **3**, 255–268.

94 J. Israelachvili, *Intermolecular and Surface Forces*, Academic Press, New York, 3 edn, 2010.

95 N. Vogel, R. A. Belisle, B. Hatton, T. S. Wong and J. Aizenberg, *Nat. Commun.*, 2013, **4**, 2167.

96 X. Zhang, J. Zhang, Z. Ren, X. Li, X. Zhang, D. Zhu, T. Wang, T. Tian and B. Yang, *Langmuir*, 2009, **25**, 7375.

97 N. Vogel, J. Fischer, R. Mohammadi, M. Retsch, H. J. Butt, K. Landfester, C. K. Weiss and M. Kreiter, *Nano Lett.*, 2011, **11**, 446–454.

98 Y. Lu, H. Yu, S. Chen, X. Quan and H. Zhao, *Environ. Sci. Technol.*, 2012, **46**, 1724–1730.

99 K. R. Phillips, N. Vogel, Y. Hu, M. Kolle, C. C. Perry and J. Aizenberg, *Chem. Mater.*, 2014, **26**, 1622–1628.

100 M. Schaffner, G. England, M. Kolle, J. Aizenberg and N. Vogel, *Small*, 2015, **11**, 4334–4340.

101 Y. Yin, Y. Lu, B. Gates and Y. Xia, *J. Am. Chem. Soc.*, 2001, **123**, 8718–8729.

102 J. Park, J. Moon, H. Shin, D. Wang and M. Park, *J. Colloid Interface Sci.*, 2006, **298**, 713–719.

103 N. Koay, I. B. Burgess, T. M. Kay, B. A. Nerger, M. Miles-Rossouw, T. Shirman, T. L. Vu, G. England, K. R. Phillips, S. Utech, N. Vogel, M. Kolle and J. Aizenberg, *Opt. Express*, 2014, **22**, 27750–27768.

104 F. Li, X. Badel, J. Linnros and J. B. Wiley, *J. Am. Chem. Soc.*, 2005, **127**, 3268–3269.

105 N. Vogel, S. Utech, G. T. England, T. Shirman, K. R. Phillips, N. Koay, I. B. Burgess, M. Kolle, D. A. Weitz and J. Aizenberg, *Proc. Natl. Acad. Sci. U. S. A.*, 2015, **112**, 10845–10850.

106 P. Born, A. Munoz, C. Cavelius and T. Kraus, *Langmuir*, 2012, **28**, 8300–8308.

107 A. S. Dimitrov and K. Nagayama, *Langmuir*, 1996, **12**, 1303–1311.

108  L. Malaquin, T. Kraus, H. Schmid, E. Delamarche and H. Wolf, *Langmuir*, 2007, **23**, 11513–11521.

109  P. Jiang, T. Prasad, M. J. McFarland and V. L. Colvin, *Appl. Phys. Lett.*, 2006, **89**, 011908.

110  M. Giersig and P. Mulvaney, *Langmuir*, 1993, **9**, 3408–3413.

111  C. Park, T. Lee, Y. Xia, T. J. Shin, J. Myoung and U. Jeong, *Adv. Mater.*, 2014, **26**, 4633–4638.

112  C. Park, K. Koh and U. Jeong, *Sci. Rep.*, 2015, **5**, 8340.

113  M. Retsch, Z. Zhou, S. Rivera, M. Kappl, X. S. Zhao, U. Jonas and Q. Li, *Macromol. Chem. Phys.*, 2009, **210**, 230–241.

114  E. Sirotkin, J. D. Apweiler and F. Y. Ogrin, *Langmuir*, 2010, **26**, 10677–10683.

115  N. Vogel, L. de Viguerie, U. Jonas, C. Weiss and K. Landfester, *Adv. Funct. Mater.*, 2011, **21**, 3064.

116  N. Vogel, S. Goerres, C. K. Weiss and K. Landfester, *Macromol. Chem. Phys.*, 2011, **212**, 1719.

117  X. Ye and L. Qi, *Nano Today*, 2011, **6**, 608–631.

118  T. Kraus, D. Brodoceanu, N. Pazos-Perez and A. Fery, *Adv. Funct. Mater.*, 2013, **23**, 4529.

119  Y. Li, W. Cai and G. Duan, *Chem. Mater.*, 2008, **20**, 615–624.

120  J. Zhang, Y. Li, X. Zhang and B. Yang, *Adv. Mater.*, 2010, **22**, 4249–4269.

121  L.-S. Wan, L.-W. Zhu, Y. Ou and Z.-K. Xu, *Chem. Commun.*, 2014, **50**, 4024.

122  W.-L. Min, B. Jiang and P. Jiang, *Adv. Mater.*, 2008, **20**, 3914–3918.

123  X. Zhang, A. V. Whitney, J. Zhao, E. M. Hicks and R. P. Van Duyne, *J. Nanosci. Nanotechnol.*, 2006, **6**, 1920–1934.

124  A. Nemiroski, M. Gonidec, J. M. Fox, P. Jean-Remy, E. Turnage and G. M. Whitesides, *ACS Nano*, 2014, **8**, 11061–11070.

125  M. Retsch, M. Tamm, N. Bocchio, N. Horn, R. Forch, U. Jonas and M. Kreiter, *Small*, 2009, **5**, 2105–2110.

126  A. Manzke, N. Vogel, C. K. Weiss, U. Ziener, A. Plettl, K. Landfester and P. Ziemann, *Nanoscale*, 2011, **3**, 2523–2528.

127  A. Manzke, A. Plettl, U. Wiedwald, L. Han, P. Ziemann, E. Schreiber, U. Ziener, N. Vogel, C. K. Weiss, K. Landfester, K. Fauth, J. Biskupek and U. Kaiser, *Chem. Mater.*, 2012, **24**, 1048–1054.

128  J. Chen, W. S. Liao, X. Chen, T. Yang, S. E. Wark, D. H. Son, J. D. Batteas and P. S. Cremer, *ACS Nano*, 2009, **3**, 173–180.

129  A. F. Routh, *Rep. Prog. Phys.*, 2013, **76**, 046603.

130  Y. Y. Diao and X. Y. Liu, *Adv. Funct. Mater.*, 2012, **22**, 1354–1375.

131  W. L. Vos, M. Megens, C. M. vanKats and P. Bösecke, *Langmuir*, 1997, **13**, 6004–6008.

132  K. E. Davis, W. B. Russel and W. J. Glantschnig, *J. Chem. Soc., Faraday Trans.*, 1991, **87**, 411–424.

133  M. Bardosova, M. E. Pemble, I. M. Povey and R. H. Tredgold, *Adv. Mater.*, 2010, **22**, 3104–3124.

134  A. Mihi, M. Ocaña and H. Míguez, *Adv. Mater.*, 2006, **18**, 2244–2249.

135  O. L. J. Pursiainen, J. J. Baumberg, H. Winkler, B. Viel, P. Spahn and T. Ruhl, *Adv. Mater.*, 2008, **20**, 1484–1487.

136  T. Ruhl, P. Spahn and G. P. Hellmann, *Polymer*, 2003, **44**, 7625–7634.

137  A. van Blaaderen, R. Ruel and P. Wiltzius, *Nature*, 1997, **385**, 321–324.

138  J. P. Hoogenboom, A. K. Van Langen-Suurling, J. Romijn and A. Van Blaaderen, *Phys. Rev. Lett.*, 2003, **90**, 138301.

139  K. E. Jensen, D. Pennachio, D. Recht, D. A. Weitz and F. Spaepen, *Soft Matter*, 2013, **9**, 320–328.

140  C. Y. Cho and J. H. Moon, *Adv. Mater.*, 2011, **23**, 2971–2975.

141  J. Zhou, J. Wang, Y. Huang, G. Liu, L. Wang, S. Chen, X. Li, D. Wang, Y. Song and L. Jiang, *NPG Asia Mater.*, 2012, **4**, e21.

142  S.-H. Kim, J.-M. Lim, W. C. Jeong, D.-G. Choi and S.-M. Yang, *Adv. Mater.*, 2008, **20**, 3211–3217.

143  S. H. Kim, H. S. Park, J. H. Choi, J. W. Shim and S. M. Yang, *Adv. Mater.*, 2010, **22**, 946–950.

144  H. S. Lee, T. S. Shim, H. Hwang, S.-M. Yang and S.-H. Kim, *Chem. Mater.*, 2013, **25**, 2684–2690.

145  S. Y. Lee, S.-H. Kim, H. Hwang, J. Y. Sim and S.-M. Yang, *Adv. Mater.*, 2014, **26**, 2391.

146  T. Ding, S. K. Smoukov and J. J. Baumberg, *Nanoscale*, 2015, **7**, 1857–1863.

147  H. S. Lee, T. S. Shim, H. Hwang, S. M. Yang and S. H. Kim, *Chem. Mater.*, 2013, **25**, 26842690.

148  T. Ding, Q. Zhao, S. K. Smoukov and J. J. Baumberg, *Adv. Opt. Mater.*, 2014, **2**, 1098–1104.

149  M. Allard, E. H. Sargent, P. C. Lewis and E. Kumacheva, *Adv. Mater.*, 2004, **16**, 1360–1364.

150  G. A. Ozin and S. M. Yang, *Adv. Funct. Mater.*, 2001, **11**, 95–104.

151  A. Schweikart, A. Fortini, A. Wittemann, M. Schmidt and A. Fery, *Soft Matter*, 2010, **6**, 5860.

152  A. van Blaaderen, R. Ruel and P. Wiltzius, *Nature*, 1997, **385**, 321–324.

153  S. Watanabe, K. Inukai, S. Mizuta and M. T. Miyahara, *Langmuir*, 2009, **25**, 7287–7295.

154  Y. Mino, S. Watanabe and M. T. Miyahara, *Langmuir*, 2011, **27**, 5290–5295.

155  C. A. Fustin, G. Glasser, H. W. Spiess and U. Jonas, *Adv. Mater.*, 2003, **15**, 1025–1028.

156  S. H. Kim, S. Y. Lee, G. R. Yi, D. J. Pine and S. M. Yang, *J. Am. Chem. Soc.*, 2006, **128**, 10897–10904.

157  O. D. Velev, A. M. Lenhoff and E. W. Kaler, *Science*, 2000, **287**, 2240–2243.

158  Y. Zhao, L. Shang, Y. Cheng and Z. Gu, *Acc. Chem. Res.*, 2014, **47**, 3632–3642.

159  P. Jiang and M. J. McFarland, *J. Am. Chem. Soc.*, 2004, **126**, 13778–13786.

160  C. G. Schaefer, B. Viel, G. P. Hellmann, M. Rehahn and M. Gallei, *ACS Appl. Mater. Interfaces*, 2013, **5**, 10623.

161  A. R. Abate and D. A. Weitz, *Lab Chip*, 2011, **11**, 1911.

162  G. von Freymann, V. Kitaev, B. V. Lotsch and G. A. Ozin, *Chem. Soc. Rev.*, 2013, **42**, 2528–2554.

163  L. Zhou, G. Liu, Y. Wu, Q. Fan and J. Shao, *Fibers Polym.*, 2014, **15**, 1112–1122.

164  J.-S. S. Lee, C. H. Lim, S.-M. M. Yang and S.-H. H. Kim, *Langmuir*, 2014, **30**, 2369–2375.

165  D. P. Josephson, E. J. Popczun and A. Stein, *J. Phys. Chem. C*, 2013, **117**, 13585–13592.

316 | *Chem. Soc. Rev.*, 2016, **45**, 281–322

This journal is © The Royal Society of Chemistry 2016

166  J. J. Kim, Y. Lee, H. G. Kim, K. J. Choi, H. S. Kweon, S. Park and K. H. Jeong, *Proc. Natl. Acad. Sci. U. S. A.*, 2012, **109**, 18674–18678.

167  H. Hu, Q.-W. Chen, J. Tang, X.-Y. Hu and X.-H. Zhou, *J. Mater. Chem.*, 2012, **22**, 11048.

168  H. Hu, J. Tang, H. Zhong, Z. Xi, C. Chen and Q. Chen, *Sci. Rep.*, 2013, **3**, 1484.

169  H. Hu, H. Zhong, C. Chen and Q. Chen, *J. Mater. Chem. C*, 2014, **2**, 3695.

170  Z. Yu, C. F. Wang, L. Ling, L. Chen and S. Chen, *Angew. Chem., Int. Ed.*, 2012, **51**, 2375–2378.

171  C. E. Finlayson and J. J. Baumberg, *Polym. Int.*, 2013, **62**, 1403–1407.

172  T. Ito, C. Katsura, H. Sugimoto, E. Nakanishi and K. Inomata, *Langmuir*, 2013, **29**, 13951–13957.

173  Y. Cho, S. Y. Lee, L. Ellerthorpe, G. Feng, G. Lin, G. Wu, J. Yin and S. Yang, *Adv. Funct. Mater.*, 2015, DOI: 10.1002/adfm.201502774.

174  C. G. Schafer, C. Lederle, K. Zentel, B. Stuhn and M. Gallei, *Macromol. Rapid Commun.*, 2014, **35**, 1852–1860.

175  F. Gallego-Gómez, A. Blanco, D. Golmayo and C. López, *Adv. Funct. Mater.*, 2011, **21**, 4109–4119.

176  D. Scheid, C. Lederle, S. Vowinkel, C. G. Schafer, B. Stuhn and M. Gallei, *J. Mater. Chem. C*, 2014, **2**, 2583–2590.

177  F. Gallego-Gomez, A. Blanco and C. Lopez, *Adv. Mater.*, 2012, **24**, 6204–6209.

178  J. Wang, Y. Hu, R. Deng, R. Liang, W. Li, S. Liu and J. Zhu, *Langmuir*, 2013, **29**, 8825–8834.

179  S. Furumi, *J. Mater. Chem. C*, 2013, **1**, 6003.

180  Y. Takeoka, S. Yoshioka, A. Takano, S. Arai, K. Nueangnoraj, H. Nishihara, M. Teshima, Y. Ohtsuka and T. Seki, *Angew. Chem., Int. Ed.*, 2013, **52**, 7261–7265.

181  S. Magkiriadou, J.-G. Park, Y.-S. Kim and V. N. Manoharan, *Opt. Mater. Express*, 2012, **2**, 1343.

182  S. Yoshioka and Y. Takeoka, *ChemPhysChem*, 2014, **15**, 2209–2215.

183  Y. Gotoh, H. Suzuki, N. Kumano, T. Seki, K. Katagiri and Y. Takeoka, *New J. Chem.*, 2012, **36**, 2171.

184  C. H. Lim, H. Kang and S. H. Kim, *Langmuir*, 2014, **30**, 8350–8356.

185  J.-G. G. Park, S.-H. H. Kim, S. Magkiriadou, T. M. Choi, Y.-S. S. Kim and V. N. Manoharan, *Angew. Chem., Int. Ed.*, 2014, **53**, 2899–2903.

186  A. Belardini, A. Benedetti, M. Centini, G. Leahu, F. Mura, S. Sennato, C. Sibilia, V. Robbiano, M. C. Giordano, C. Martella, D. Comoretto and F. B. de Mongeot, *Adv. Opt. Mater.*, 2014, **2**, 208–213.

187  D. Brodoceanu, R. Elnathan, B. Prieto-Simon, B. Delalat, T. Guinan, E. Kroner, N. H. Voelcker and T. Kraus, *ACS Appl. Mater. Interfaces*, 2015, **7**, 1160–1169.

188  J. W. Leem, M. S. Kim and J. S. Yu, *J. Opt. Soc. Am. B*, 2013, **30**, 1665.

189  S. Kim, A. N. Mitropoulos, J. D. Spitzberg, D. L. Kaplan and F. G. Omenetto, *Opt. Express*, 2013, **21**, 8897–8903.

190  V. Robbiano, M. Giordano, C. Martella, F. D. Stasio, D. Chiappe, F. B. de Mongeot and D. Comoretto, *Adv. Opt. Mater.*, 2013, **1**, 389–396.

191  H. R. Míguez, S. G. Romanov, A. V. Korovin, M. Reza Bahrami, U. Peschel, S. G. Romanov, L. C. Andreani and C. Seassal, *Proc. SPIE*, 2012, **8425**, 842514.

192  A. Belardini, *Adv. Opt. Mater.*, 2014, **2**, 208–213.

193  S. Romanov, N. Vogel, K. Bley, K. Landfester, C. K. Weiss, S. Orlov, A. V. Korovin, G. P. Chuiko, A. Regensburger, A. Romanova, A. Kriesch and U. Peschel, *Phys. Rev. B: Condens. Matter Mater. Phys.*, 2012, **86**, 195145.

194  C. Stelling, C. Bernhardt and M. Retsch, *Macromol. Chem. Phys.*, 2015, **216**, 1682–1688.

195  Y. Li, J. Zhang, S. Zhu, H. Dong, F. Jia, Z. Wang, Z. Sun, L. Zhang, Y. Li, H. Li, W. Xu and B. Yang, *Adv. Mater.*, 2009, **21**, 4731–4734.

196  S. Guldin and U. Steiner, *SPIE Proc. Micro- and Nanotechnology Sensors, Systems, and Applications VI*, 2014, **9083**, 908320.

197  H. Macleod, *Thin film optical filters*, Institute of Physics Publishing, 3 edn, 2001.

198  H. Budunoglu, A. Yildirim and M. Bayindir, *J. Mater. Chem.*, 2012, **22**, 9671.

199  U. Tuvshindorj, A. Yildirim, F. E. Ozturk and M. Bayindir, *ACS Appl. Mater. Interfaces*, 2014, **6**, 9680–9688.

200  X.-X. Zhang, B.-B. Xia, H.-P. Ye, Y.-L. Zhang, B. Xiao, L.-H. Yan, H.-B. Lv and B. Jiang, *J. Mater. Chem.*, 2012, **22**, 13132.

201  W.-B. Hung and T.-M. Chen, *Sol. Energy Mater. Sol. Cells*, 2015, **133**, 39–47.

202  Z. Wang, W. Ji, H. Du, X. Li, J. Gong, J. Ma and J. Xu, *J. Sol–Gel Sci. Technol.*, 2014, **72**, 511–517.

203  S. J. Yeo, F. Tu, S. H. Kim, G. R. Yi, P. J. Yoo and D. Lee, *Soft Matter*, 2015, **11**, 1582–1588.

204  E. Sowade, J. Hammerschmidt, T. Blaudeck and R. R. Baumann, *Adv. Eng. Mater.*, 2012, **14**, 98–100.

205  M. Kuang, J. Wang, B. Bao, F. Li, L. Wang, L. Jiang and Y. Song, *Adv. Opt. Mater.*, 2014, **2**, 34–38.

206  V. Rastogi, S. Melle, O. G. Calderón, A. A. García, M. Marquez and O. D. Velev, *Adv. Mater.*, 2008, **20**, 4263–4268.

207  S. Y. Lee, S.-H. H. Kim, H. Hwang, J. Y. Sim and S.-M. M. Yang, *Adv. Mater.*, 2014, **26**, 2391–2397.

208  T. Ding, Y. Long, K. Zhong, K. Song, G. Yang and C.-H. Tung, *J. Mater. Chem. C*, 2014, **2**, 4100.

209  Y. Y. Yan, N. Gao and W. Barthlott, *Adv. Colloid Interface Sci.*, 2011, **169**, 80–105.

210  S. W. Choi, Y. Zhang and Y. Xia, *Langmuir*, 2010, **26**, 19001–19006.

211  C. F. Joao, J. M. Vasconcelos, J. C. Silva and J. P. Borges, *Tissue Eng., Part B*, 2014, **20**, 437–454.

212  M. Sharma, G. I. Waterhouse, S. W. Loader, S. Garg and D. Svirskis, *Int. J. Pharm.*, 2013, **443**, 163–168.

213  B. Zhang, Y. Cheng, H. Wang, B. Ye, L. Shang, Y. Zhao and Z. Gu, *Nanoscale*, 2015, **7**, 10590–10594.

214  K. Rhee do, B. Jung, Y. H. Kim, S. J. Yeo, S. J. Choi, A. Rauf, S. Han, G. R. Yi, D. Lee and P. J. Yoo, *ACS Appl. Mater. Interfaces*, 2014, **6**, 9950–9954.

215  Y. Lu, S. Sathasivam, J. Song, C. R. Crick, C. J. Carmalt and I. P. Parkin, *Science*, 2015, **347**, 1132–1135.

This journal is © The Royal Society of Chemistry 2016

*Chem. Soc. Rev.*, 2016, **45**, 281–322 | 317

216 A. Tuteja, W. Choi, J. M. Mabry, G. H. McKinley and R. E. Cohen, *Proc. Natl. Acad. Sci. U. S. A.*, 2008, **105**, 18200–18205.

217 A. K. Epstein, T. S. Wong, R. A. Belisle, E. M. Boggs and J. Aizenberg, *Proc. Natl. Acad. Sci. U. S. A.*, 2012, **109**, 13182–13187.

218 R. N. Wenzel, *Ind. Eng. Chem.*, 1936, **28**, 988–994.

219 A. B. D. Cassie and S. Baxter, *Trans. Faraday Soc.*, 1944, **40**, 546.

220 A. Plettl, F. Enderle, M. Saitner, A. Manzke, C. Pfahler, S. Wiedemann and P. Ziemann, *Adv. Funct. Mater.*, 2009, **19**, 3279–3284.

221 X. Zhang, J. Zhang, Z. Ren, X. Li, X. Zhang, D. Zhu, T. Wang, T. Tian and B. Yang, *Langmuir*, 2009, **25**, 7375–7382.

222 S.-G. Park, S. Y. Lee, S. G. Jang and S.-M. Yang, *Langmuir*, 2010, **26**, 5295–5299.

223 Y. Wang, M. Wang and X. Ge, *Langmuir*, 2014, **30**, 10804–10808.

224 Z. Z. Gu, H. Uetsuka, K. Takahashi, R. Nakajima, H. Onishi, A. Fujishima and O. Sato, *Angew. Chem., Int. Ed.*, 2003, **42**, 894–897.

225 M. Xu, N. Lu, H. Xu, D. Qi, Y. Wang, S. Shi and L. Chi, *Soft Matter*, 2010, **6**, 1438–1443.

226 A. Lafuma and D. Quéré, *EPL*, 2011, **96**, 56001.

227 J. D. Smith, R. Dhiman, S. Anand, E. Reza-Garduno, R. E. Cohen, G. H. McKinley and K. K. Varanasi, *Soft Matter*, 2013, **9**, 1772–1780.

228 T. S. Wong, S. H. Kang, S. K. Tang, E. J. Smythe, B. D. Hatton, A. Grinthal and J. Aizenberg, *Nature*, 2011, **477**, 443–447.

229 H. J. Tsai and Y. L. Lee, *Langmuir*, 2007, **23**, 12687–12692.

230 H. Ogihara, J. Xie, J. Okagaki and T. Saji, *Langmuir*, 2012, **28**, 4605–4608.

231 D. Lee, M. F. Rubner and R. E. Cohen, *Nano Lett.*, 2006, **6**, 2305–2312.

232 Z. Gemici, H. Shimomura, R. E. Cohen and M.F. Rubner, *Langmuir*, 2008, **24**, 2168–2177.

233 S. Sunny, N. Vogel, C. Howell, T. L. Vu and J. Aizenberg, *Adv. Funct. Mater.*, 2014, **24**, 6658–6667.

234 A. Tuteja, W. Choi, M. Ma, J. M. Mabry, S. A. Mazzella, G. C. Rutledge, G. H. McKinley and R. E. Cohen, *Science*, 2007, **318**, 1618–1622.

235 A. Ahuja, J. A. Taylor, V. Lifton, A. A. Sidorenko, T. R. Salamon, E. J. Lobaton, P. Kolodner and T. N. Krupenkin, *Langmuir*, 2008, **24**, 9–14.

236 K. Ellinas, A. Tserepi and E. Gogolides, *Langmuir*, 2011, **27**, 3960–3969.

237 X. Deng, L. Mammen, H. J. Butt and D. Vollmer, *Science*, 2012, **335**, 67–70.

238 A. Steele, I. Bayer and E. Loth, *Nano Lett.*, 2009, **9**, 501–505.

239 K. R. Phillips, N. Vogel, I. B. Burgess, C. C. Perry and J. Aizenberg, *Langmuir*, 2014, **30**, 7615–7620.

240 C. W. Extrand and S. I. Moon, *Langmuir*, 2008, **24**, 9470–9473.

241 C. W. Extrand and S. I. Moon, *Langmuir*, 2012, **28**, 3503–3509.

242 J. Wang, Y. Wen, J. Hu, Y. Song and L. Jiang, *Adv. Funct. Mater.*, 2007, **17**, 219–225.

243 J. Wang, Y. Wen, X. Feng, Y. Song and L. Jiang, *Macromol. Rapid Commun.*, 2006, **27**, 188–192.

244 H. Ge, G. Wang, Y. He, X. Wang, Y. Song, L. Jiang and D. Zhu, *ChemPhysChem*, 2006, **7**, 575–578.

245 L. Xu, J. Wang, Y. Song and L. Jiang, *Chem. Mater.*, 2008, **20**, 3554–3556.

246 J. H. Lee, C. Y. Koh, J. P. Singer, S. J. Jeon, M. Maldovan, O. Stein and E. L. Thomas, *Adv. Mater.*, 2014, **26**, 532–569.

247 C. I. Aguirre, E. Reguera and A. Stein, *Adv. Funct. Mater.*, 2010, **20**, 2565–2578.

248 Y. Fang, B. M. Phillips, K. Askar, B. Choi, P. Jiang and B. Jiang, *J. Mater. Chem. C*, 2013, **1**, 6031–6047.

249 Q. Li, M. Retsch, J. Wang, W. Knoll and U. Jonas, *Top. Curr. Chem.*, 2009, **287**, 135–180.

250 G. von Freymann, V. Kitaev, B. V. Lotsch and G. A. Ozin, *Chem. Soc. Rev.*, 2013, **42**, 2528.

251 Y. Takeoka, *J. Mater. Chem. C*, 2013, **1**, 6059–6074.

252 A. Stein, B. E. Wilson and S. G. Rudisill, *Chem. Soc. Rev.*, 2013, **42**, 2763–2803.

253 M. J. Banholzer, J. E. Millstone, L. Qin and C. A. Mirkin, *Chem. Soc. Rev.*, 2008, **37**, 885–897.

254 B. Sharma, M. Fernanda Cardinal, S. L. Kleinman, N. G. Greeneltch, R. R. Frontiera, M. G. Blaber, G. C. Schatz and R. P. Van Duyne, *MRS Bull.*, 2013, **38**, 615–624.

255 M. D. Sonntag, J. M. Klingsporn, A. B. Zrimsek, B. Sharma, L. K. Ruvuna and R. P. Duyne, *Chem. Soc. Rev.*, 2014, **43**, 1230–1247.

256 M. Grzelczak and L. M. Liz-Marzan, *Langmuir*, 2013, **29**, 4652–4663.

257 A. C. Arsenault, D. P. Puzzo, I. Manners and G. A. Ozin, *Nat. Photonics*, 2007, **1**, 468–472.

258 L. Jin, Y. Zhao, X. Liu, Y. Wang, B. Ye, Z. Xie and Z. Gu, *Soft Matter*, 2012, **8**, 4911.

259 W. Shen, M. Li, C. Ye, L. Jiang and Y. Song, *Lab Chip*, 2012, **12**, 3089–3095.

260 L. Bai, Z. Xie, W. Wang, C. Yuan, Y. Zhao, Z. Mu, Q. Zhong and Z. Gu, *ACS Nano*, 2014, **8**, 11094–11100.

261 N. Griffete, H. Frederich, A. Maitre, S. Ravaine, M. M. Chehimi and C. Mangeney, *Langmuir*, 2012, **28**, 1005–1012.

262 C. Zhou, T. Wang, J. Liu, C. Guo, Y. Peng, J. Bai, M. Liu, J. Dong, N. Gao, B. A. Ning and Z. Gao, *Analyst*, 2012, **137**, 4469–4474.

263 D. Xu, W. Zhu, C. Wang, T. Tian, J. Cui, J. Li, H. Wang and G. Li, *Chem. – Eur. J.*, 2014, **20**, 16620–16625.

264 Y. Yuan, Z. Li, Y. Liu, J. Gao, Z. Pan and Y. Liu, *Chemistry*, 2012, **18**, 303–309.

265 Y. Zhang, Z. Pan, Y. Yuan, Z. Sun, J. Ma, G. Huang, F. Xing and J. Gao, *Phys. Chem. Chem. Phys.*, 2013, **15**, 17250–17256.

266 X. Hu, Q. An, G. Li, S. Tao and J. Liu, *Angew. Chem., Int. Ed.*, 2006, **45**, 8145–8148.

267 Y. Zhao, B. Zhang, Y. Cheng, H. Wang, B. Ye and L. Shang, *Nanoscale*, 2015, **7**, 10590–10594.

268 H. L. Li, L. X. Chang, J. X. Wang, L. M. Yang and Y. L. Song, *J. Mater. Chem.*, 2008, **18**, 5098–5103.

269 S. Amrehn, X. Wu, C. Schumacher and T. Wagner, *Phys. Status Solidi A*, 2015, **212**, 1266–1272.

270 Y. Zhang, J. Qiu, M. Gao, P. Li, L. Gao, L. Heng, B. Z. Tang and L. Jiang, *J. Mater. Chem. C*, 2014, **2**, 8865–8872.

271 C. Liu, G. Gao, Y. Zhang, L. Wang, J. Wang and Y. Song, *Macromol. Rapid Commun.*, 2012, **33**, 380–385.

272 R. Hirashima, T. Seki, K. Katagiri, Y. Akuzawa, T. Torimoto and Y. Takeoka, *J. Mater. Chem. C*, 2014, **2**, 344–348.

273 N. Griffete, H. Frederich, A. Maître, M. M. Chehimi, S. Ravaine and C. Mangeney, *J. Mater. Chem.*, 2011, **21**, 13052.

274 J. Shin, S. G. Han and W. Lee, *Sens. Actuators, B*, 2012, **168**, 20–26.

275 Z. Pan, J. Ma, J. Yan, M. Zhou and J. Gao, *J. Mater. Chem.*, 2012, **22**, 2018–2025.

276 E. Choi, Y. Choi, Y. H. P. Nejad, K. Shin and J. Park, *Sens. Actuators, B*, 2013, **180**, 107–113.

277 W. Hong, Y. Chen, X. Feng, Y. Yan, X. Hu, B. Zhao, F. Zhang, D. Zhang, Z. Xu and Y. Lai, *Chem. Commun.*, 2013, **49**, 8229–8231.

278 M.-L. Zhang, F. Jin, M.-L. Zheng and X.-M. Duan, *RSC Adv.*, 2014, **4**, 20567.

279 T. Tian, X. Li, J. Cui, J. Li, Y. Lan, C. Wang, M. Zhang, H. Wang and G. Li, *ACS Appl. Mater. Interfaces*, 2014, **6**, 15456–15465.

280 B. Ye, H. Ding, Y. Cheng, H. Gu, Y. Zhao, Z. Xie and Z. Gu, *Adv. Mater.*, 2014, **26**, 3270–3274.

281 D. P. Puzzo, A. C. Arsenault, I. Manners and G. A. Ozin, *Angew. Chem., Int. Ed.*, 2009, **48**, 943–947.

282 K. Ueno, J. Sakamoto, Y. Takeoka and M. Watanabe, *J. Mater. Chem.*, 2009, **19**, 4778.

283 A. C. Arsenault, T. J. Clark, G. von Freymann, L. Cademartiri, R. Sapienza, J. Bertolotti, E. Vekris, S. Wong, V. Kitaev, I. Manners, R. Z. Wang, S. John, D. Wiersma and G. A. Ozin, *Nat. Mater.*, 2006, **5**, 179–184.

284 Y. Y. Diao, X. Y. Liu, G. W. Toh, L. Shi and J. Zi, *Adv. Funct. Mater.*, 2013, **23**, 5373–5380.

285 S. Kim, A. N. Mitropoulos, J. D. Spitzberg, H. Tao, D. L. Kaplan and F. G. Omenetto, *Nat. Photonics*, 2012, **6**, 817–822.

286 G. Huang, Y. Yin, Z. Pan, M. Chen, L. Zhang, Y. Liu, Y. Zhang and J. Gao, *Biomacromolecules*, 2014, **15**, 4396–4402.

287 J. Huang, C. A. Tao, Q. An, W. Zhang, Y. Wu, X. Li, D. Shen and G. Li, *Chem. Commun.*, 2010, **46**, 967–969.

288 X. Hu, J. Huang, W. Zhang, M. Li, C. Tao and G. Li, *Adv. Mater.*, 2008, **20**, 4074–4078.

289 J. Cui, W. Zhu, N. Gao, J. Li, H. Yang, Y. Jiang, P. Seidel, B. J. Ravoo and G. Li, *Angew. Chem., Int. Ed.*, 2014, **53**, 3844–3848.

290 G. Lu, O. K. Farha, L. E. Kreno, P. M. Schoenecker, K. S. Walton, R. P. Van Duyne and J. T. Hupp, *Adv. Mater.*, 2011, **23**, 4449–4452.

291 Y. N. Wu, F. Li, W. Zhu, J. Cui, C. A. Tao, C. Lin, P. M. Hannam and G. Li, *Angew. Chem., Int. Ed.*, 2011, **50**, 12518–12522.

292 G. R. Hendrickson and L. Andrew Lyon, *Soft Matter*, 2009, **5**, 29–35.

293 S. A. Asher, S. F. Peteu, C. E. Reese, X. Lin and D. Finegold, *Anal. Bioanal. Chem.*, 2002, **373**, 632–638.

294 V. L. Alexeev, S. Das, D. N. Finegold and S. A. Asher, *Clin. Chem.*, 2004, **50**, 2353–2360.

295 A. C. Sharma, T. Jana, R. Kesavamoorthy, L. Shi, M. A. Virji, D. N. Finegold and S. A. Asher, *J. Am. Chem. Soc.*, 2004, **126**, 2971–2977.

296 J. P. Walker and S. A. Asher, *Anal. Chem.*, 2005, **77**, 1596–1600.

297 M. Kamenjicki Maurer, I. K. Lednev and S. A. Asher, *Adv. Funct. Mater.*, 2005, **15**, 1401–1406.

298 K. W. Kimble, J. P. Walker, D. N. Finegold and S. A. Asher, *Anal. Bioanal. Chem.*, 2006, **385**, 678–685.

299 J. P. Walker, K. W. Kimble and S. A. Asher, *Anal. Bioanal. Chem.*, 2007, **389**, 2115–2124.

300 M. M. Muscatello and S. A. Asher, *Adv. Funct. Mater.*, 2008, **1186**, 18.

301 Z. Jian-Tao, S. Natasha and A. A. Sanford, *Anal. Chem.*, 2012, **84**, 6416–6420.

302 C. Zhongyu, Z. Jian-Tao, X. Fei, H. Zhenmin, P. David and A. A. Sanford, *Anal. Chem.*, 2014, **86**, 4840–4847.

303 C. Fenzl, S. Wilhelm, T. Hirsch and O. S. Wolfbeis, *ACS Appl. Mater. Interfaces*, 2013, **5**, 173–178.

304 Q. Cui, M. M. Ward Muscatello and S. A. Asher, *Analyst*, 2009, **134**, 875–880.

305 E. T. Tian, J. X. Wang, Y. M. Zheng, Y. L. Song, L. Jiang and D. B. Zhu, *J. Mater. Chem.*, 2008, **18**, 1116–1122.

306 K. I. MacConaghy, C. I. Geary, J. L. Kaar and M. P. Stoykovich, *J. Am. Chem. Soc.*, 2014, **136**, 6896–6899.

307 Z. Cai, N. L. Smith, J. T. Zhang and S. A. Asher, *Anal. Chem.*, 2015, **87**, 5013–5025.

308 Y. Gao, X. Li and M. J. Serpe, *RSC Adv.*, 2015, **5**, 44074–44087.

309 Y. J. Lee and P. V. Braun, *Adv. Mater.*, 2003, **15**, 563–566.

310 D. Nakayama, Y. Takeoka, M. Watanabe and K. Kataoka, *Angew. Chem., Int. Ed.*, 2003, **42**, 4197–4200.

311 H. Yang, X. Li, Y. Lan, T. Tian, J. Cui, T. Zhu, D. Shen and G. Li, *J. Mater. Chem. C*, 2013, **1**, 6120–6128.

312 D. Xu, W. Zhu, Q. An, W. Li, X. Li, H. Yang, J. Yin and G. Li, *Chem. Commun.*, 2012, **48**, 3494–3496.

313 J. Y. Wang, Y. Cao, Y. Feng, F. Yin and J. P. Gao, *Adv. Mater.*, 2007, **19**, 3865–3871.

314 D. Liu, W. Chen, Y. Tian, S. He, W. Zheng, J. Sun, Z. Wang and X. Jiang, *Adv. Healthcare Mater.*, 2012, **1**, 90–95.

315 H. Peng, S. Wang, Z. Zhang, H. Xiong, J. Li, L. Chen and Y. Li, *J. Agric. Food Chem.*, 2012, **60**, 1921–1928.

316 F. Wang, Z. Zhu, M. Xue, F. Xue, Q. Wang, Z. Meng, W. Lu, W. Chen, F. Qi and Z. Yan, *Sens. Actuators, B*, 2015, **220**, 222–226.

317 J. P. Couturier, M. Sutterlin, A. Laschewsky, C. Hettrich and E. Wischerhoff, *Angew. Chem., Int. Ed.*, 2015, **54**, 6641–6644.

318 J. Shin, P. V. Braun and W. Lee, *Sens. Actuators, B*, 2010, **150**, 183–190.

319 K. P. Raymond, I. B. Burgess, M. H. Kinney, M. Loncar and J. Aizenberg, *Lab Chip*, 2012, **12**, 3666–3669.

320 T. A. Singleton, I. B. Burgess, B. A. Nerger, A. Goulet-Hanssens, N. Koay, C. J. Barrett and J. Aizenberg, *Soft Matter*, 2014, **10**, 1325–1328.

321 J. Hou, H. Zhang, Q. Yang, M. Li, Y. Song and L. Jiang, *Angew. Chem., Int. Ed.*, 2014, **53**, 5791–5795.

322 Q. Fang, J. Geng, B. Liu, D. Gao, F. Li, Z. Wang, G. Guan and Z. Zhang, *Chemistry*, 2009, **15**, 11507–11514.

323 H. Li, J. Wang, Z. Pan, L. Cui, L. Xu, R. Wang, Y. Song and L. Jiang, *J. Mater. Chem.*, 2011, **21**, 1730–1735.

324 D. Xu, W. Zhu, C. Wang, T. Tian, J. Li, Y. Lan, G. Zhang, D. Zhang and G. Li, *Chem. Commun.*, 2014, **50**, 14133–14136.

325 Y. Zhao, X. Zhao, C. Sun, J. Li, R. Zhu and Z. Gu, *Anal. Chem.*, 2008, **80**, 1598–1605.

326 W. Liu, L. Shang, F. Zheng, J. Lu, J. Qian, Y. Zhao and Z. Gu, *Small*, 2014, **10**, 88–93.

327 R. Schlögl, *Angew. Chem., Int. Ed.*, 2015, **54**, 3465–3520.

328 Y. Jiang, J. Deng, S. Xie, H. Yang and H. Dai, *Ind. Eng. Chem. Res.*, 2015, **54**, 900–910.

329 A. F. Lee, *Appl. Petrochem. Res.*, 2014, **4**, 11–31.

330 S. Dong, J. Feng, M. Fan, Y. Pi, L. Hu, X. Han, M. Liu, J. Sun and J. Sun, *RSC Adv.*, 2015, **5**, 14610–14630.

331 Y. Liu, H. Dai, J. Deng, L. Zhang, Z. Zhao, X. Li, Y. Wang, S. Xie, H. Yang and G. Guo, *Inorg. Chem.*, 2013, **52**, 8665–8676.

332 S. Xie, H. Dai, J. Deng, H. Yang, W. Han, H. Arandiyan and G. Guo, *J. Hazard. Mater.*, 2014, **279**, 392–401.

333 Y. Zhang, J. Deng, H. Zhang, Y. Liu and H. Dai, *Catal. Today*, 2015, **245**, 28–36.

334 S. Xie, H. Dai, J. Deng, Y. Liu, H. Yang, Y. Jiang, W. Tan, A. Ao and G. Guo, *Nanoscale*, 2013, **5**, 11207–11219.

335 K. Ji, H. Dai, J. Deng, X. Li, Y. Wang, B. Gao, G. Bai and C. T. Au, *Appl. Catal., A*, 2012, **447–448**, 41–48.

336 Y. Liu, H. Dai, J. Deng, X. Li, Y. Wang, H. Arandiyan, S. Xie, H. Yang and G. Guo, *J. Catal.*, 2013, **305**, 146–153.

337 Y. Wei, Z. Zhao, T. Li, J. Liu, A. Duan and G. Jiang, *Appl. Catal., B*, 2014, **146**, 57–70.

338 Y. Wei, Z. Zhao, J. Liu, C. Xu, G. Jiang and A. Duan, *Small*, 2013, **9**, 3957–3963.

339 Y. Wei, Z. Zhao, J. Liu, S. Liu, C. Xu, A. Duan and G. Jiang, *J. Catal.*, 2014, **317**, 62–74.

340 Y. Wei, J. Liu, Z. Zhao, Y. Chen, C. Xu, A. Duan, G. Jiang and H. He, *Angew. Chem., Int. Ed.*, 2011, **50**, 2326–2329.

341 Y. Wei, Z. Zhao, J. Jiao, J. Liu, A. Duan and G. Jiang, *Catal. Today*, 2015, **245**, 37–45.

342 H. Liu, K. Wang, Y. Shi, X. Gao, H. Liu, B. Wang and C. Xu, *RSC Adv.*, 2014, **4**, 29694.

343 Y. Wei, Z. Zhao, B. Jin, X. Yu, J. Jiao, K. Li and J. Liu, *Catal. Today*, 2015, **251**, 103–113.

344 X. Yu, J. Li, Y. Wei, Z. Zhao, J. Liu, B. Jin, A. Duan and G. Jiang, *Ind. Eng. Chem. Res.*, 2014, **53**, 9653–9664.

345 B. Jin, Y. Wei, Z. Zhao, J. Liu, X. Yu, Y. Li and J. Li, *Catal. Today*, 2015, 1–11, DOI: 10.1016/j.cattod.2015.01.021.

346 S. Cai, D. Zhang, L. Zhang, L. Huang, H. Li, R. Gao, L. Shi and J. Zhang, *Catal. Sci. Technol.*, 2014, **4**, 93–101.

347 Y. Xin, P. Jiang, M. Yu, H. Gu, Q. Li and Z. Zhang, *J. Mater. Chem. A*, 2014, **2**, 6419.

348 H. Arandiyan, H. Dai, K. Ji, H. Sun and J. Li, *ACS Catal.*, 2015, **5**, 1781–1793.

349 G. Guo, K. Lian, F. Gu, D. Han and Z. Wang, *Chem. Commun.*, 2014, **50**, 13575–13577.

350 H. Arandiyan, H. Dai, J. Deng, Y. Wang, H. Sun, S. Xie, B. Bai, Y. Liu, K. Ji and J. Li, *J. Phys. Chem. C*, 2014, **118**, 14913–14928.

351 K. An, S. Alayoglu, N. Musselwhite, K. Na and G. A. Somorjai, *J. Am. Chem. Soc.*, 2014, **136**, 6830–6833.

352 G. Liu, T. Niu, D. Pan, F. Liu and Y. Liu, *Appl. Catal., A*, 2014, **483**, 10–18.

353 X. Zhang, R. Hirota, T. Kubota, Y. Yoneyama and N. Tsubaki, *Catal. Commun.*, 2011, **13**, 44–48.

354 J. J. Woodford, J.-P. Dacquin, K. Wilson and A. F. Lee, *Energy Environ. Sci.*, 2012, **5**, 6145.

355 J. J. Creasey, C. M. A. Parlett, J. C. Manayil, M. A. Isaacs, K. Wilson and A. F. Lee, *Green Chem.*, 2015, **17**, 2398–2405.

356 C. M. A. Parlett, P. Keshwalla, S. G. Wainwright, D. W. Bruce, N. S. Hondow, K. Wilson and A. F. Lee, *ACS Catal.*, 2013, **3**, 2122–2129.

357 T. Kamegawa, S. Tanaka, H. Seto, D. Zhou and H. Yamashita, *Phys. Chem. Chem. Phys.*, 2013, **15**, 13323–13328.

358 T. Sen, J. Whittle and M. Howard, *Chem. Commun.*, 2012, **48**, 4232–4234.

359 G. Collins, M. Blömker, M. Osiak, J. D. Holmes, M. Bredol and C. O'Dwyer, *Chem. Mater.*, 2013, **25**, 4312–4320.

360 J. Jiao, Y. Wei, Z. Zhao, J. Liu, J. Li, A. Duan and G. Jiang, *Ind. Eng. Chem. Res.*, 2014, **53**, 17345–17354.

361 J. Jiao, Y. Wei, Z. Zhao, W. Zhong, J. Liu, J. Li, A. Duan and G. Jiang, *Catal. Today*, 2015, 1–8, DOI: 10.1016/j.cattod. 2015.01.030.

362 X. Zheng, S. Meng, J. Chen, J. Wang, J. Xian, Y. Shao, X. Fu and D. Li, *J. Phys. Chem. C*, 2013, **117**, 21263–21273.

363 H. Lee, T. Shim, H. Hwang, S.-M. Yang and S.-H. Kim, *Chem. Mater.*, 2013, **25**, 2684–2690.

364 Z. Cai, J. Teng, Z. Xiong, Y. Li, Q. Li, X. Lu and X. S. Zhao, *Langmuir*, 2011, **27**, 5157–5164.

365 M. Wu, J. Jin, J. Liu, Z. Deng, Y. Li, O. Deparis and B.-L. Su, *J. Mater. Chem. A*, 2013, **1**, 15491.

366 M. Wu, J. Liu, J. Jin, C. Wang, S. Huang, Z. Deng, Y. Li and B.-L. Su, *Appl. Catal., B*, 2014, **150–151**, 411–420.

367 T. Kamegawa, Y. Ishiguro, H. Seto and H. Yamashita, *J. Mater. Chem. A*, 2015, **3**, 2323–2330.

368 W.-Q. Fan, H.-Y. Bai, G.-H. Zhang, Y.-S. Yan, C.-B. Liu and W.-D. Shi, *CrystEngComm*, 2014, **16**, 116–122.

369 D. Qi, L. Lu, Z. Xi, L. Wang and J. Zhang, *Appl. Catal., B*, 2014, **160–161**, 621–628.

370 T. Wang, X. Yan, S. Zhao, B. Lin, C. Xue, G. Yang, S. Ding, B. Yang, C. Ma, G. Yang and G. Yang, *J. Mater. Chem. A*, 2014, **2**, 15611.

371 S. Lee, Y. Lee, D. H. Kim and J. H. Moon, *ACS Appl. Mater. Interfaces*, 2013, **5**, 12526–12532.

372 L. Lu, L. Li, T. Hu, W. Zhang, X. Huang, J. Zhang and X. Liu, *J. Mol. Catal. A: Chem.*, 2014, **394**, 283–294.

373 R. Yang, L. Yang, T. Tao, F. Ma, M. Xu and Z. Zhang, *Appl. Surf. Sci.*, 2013, **288**, 2–7.

374 M. Li, X. Li, G. Jiang and G. He, *Ceram. Int.*, 2015, **41**, 5749–5757.

375 S.-L. Chen, A.-J. Wang, C. Dai, J. B. Benziger and X.-C. Liu, *Chem. Eng. J.*, 2014, **249**, 48–53.

320 | *Chem. Soc. Rev.*, 2016, **45**, 281–322

This journal is © The Royal Society of Chemistry 2016

376 Z. Cai, Z. Xiong, X. Lu and J. Teng, *J. Mater. Chem. A*, 2014, **2**, 545–553.

377 Y. Zhao, B. Yang, J. Xu, Z. Fu, M. Wu and F. Li, *Thin Solid Films*, 2012, **520**, 3515–3522.

378 J. Liu, J. Jin, Y. Li, H.-W. Huang, C. Wang, M. Wu, L.-H. Chen and B.-L. Su, *J. Mater. Chem. A*, 2014, **2**, 5051.

379 L. Li, X. Huang, T. Hu, J. Wang, W. Zhang and J. Zhang, *New J. Chem.*, 2014, **38**, 5293–5302.

380 S. Meng, D. Li, X. Zheng, J. Wang, J. Chen, J. Fang, Y. Shao and X. Fu, *J. Mater. Chem. A*, 2013, **1**, 2744.

381 T. Tan, W. Xie, G. Zhu, J. Shan, P. Xu, L. Li and J. Wang, *J. Porous Mater.*, 2015, **22**, 659–663.

382 S. Sun, W. Wang and L. Zhang, *J. Mater. Chem.*, 2012, **22**, 19244.

383 E. S. Da Silva, V. Prevot, C. Forano, P. Wong-Wah-Chung, H. D. Burrows and M. Sarakha, *Environ. Sci. Pollut. Res. Int.*, 2014, **21**, 11218–11227.

384 Y. Liu, H. Dai, J. Deng, L. Zhang and C. T. Au, *Nanoscale*, 2012, **4**, 2317–2325.

385 K. Ji, H. Dai, J. Deng, H. Zang, H. Arandiyan, S. Xie and H. Yang, *Appl. Catal., B*, 2015, **168–169**, 274–282.

386 H. Wang and K. Q. Zhang, *Sensors*, 2013, **13**, 4192–4213.

387 L. Lu, F. Teng, S. Tapas, D. Qi, L. Wang and J. Zhang, *Appl. Catal., B*, 2015, **163**, 9–15.

388 X. Shi, K. Zhang, K. Shin, J. H. Moon, T.-W. Lee and J. H. Park, *Phys. Chem. Chem. Phys.*, 2013, **15**, 11717–11722.

389 Z. Zhang, L. Zhang, M. N. Hedhili, H. Zhang and P. Wang, *Nano Lett.*, 2013, **13**, 14–20.

390 M. Y. Tsang, N. E. Pridmore, L. J. Gillie, Y. H. Chou, R. Brydson and R. E. Douthwaite, *Adv. Mater.*, 2012, **24**, 3406–3409.

391 M. Ma, J. K. Kim, K. Zhang, X. Shi, S. J. Kim, J. H. Moon and J. H. Park, *Chem. Mater.*, 2014, **26**, 5592–5597.

392 J. K. Kim, J. H. Moon, T.-W. Leec and J. H. Park, *Chem. Commun.*, 2012, **48**, 11939–11941.

393 X. Chen, J. Ye, S. Ouyang, T. Kako, Z. Li and Z. Zou, *ACS Nano*, 2011, **5**, 4310–4318.

394 K. Y. Yoon, J. S. Lee, K. Kim, C. H. Bak, S. I. Kim, J. B. Kim and J. H. Jang, *ACS Appl. Mater. Interfaces*, 2014, **6**, 22634–22639.

395 S. Yoon, M. Kim, I.-S. Kim, J.-H. Lim and B. Yoo, *J. Mater. Chem. A*, 2014, **2**, 11621.

396 C.-Y. Cho, S. Lee, J. Lee, D. C. Lee and J. H. Moon, *J. Mater. Chem. A*, 2014, **2**, 17568–17573.

397 C. Cheng, S. K. Karuturi, L. Liu, J. Liu, H. Li, L. T. Su, A. I. Tok and H. J. Fan, *Small*, 2012, **8**, 37–42.

398 J. Shi, *Chem. Rev.*, 2013, **113**, 2139–2181.

399 A. Primo, A. Corma and H. Garcia, *Phys. Chem. Chem. Phys.*, 2011, **13**, 886–910.

400 C. T. Dinh, H. Yen, F. Kleitz and T. O. Do, *Angew. Chem., Int. Ed.*, 2014, **53**, 6618–6623.

401 L. Chen, L. Xie, M. Wang and X. Ge, *J. Mater. Chem. A*, 2015, **3**, 2991–2998.

402 L. Yuan, Z. Yu, C. Li, J. Li, Y. Shen, H. Zhang, C. Wang and A. Xie, *J. Electrochem. Soc.*, 2014, **161**, H332–H336.

403 Z. Liu, Y. Yang, J. Mi, X. Tan and C. Lv, *Int. J. Hydrogen Energy*, 2013, **38**, 4445–4455.

404 T. Kamegawa, N. Suzuki, M. Che and H. Yamashita, *Langmuir*, 2011, **27**, 2873–2879.

405 C. Briens, J. Piskorz and F. Berruti, *Int.J. Chem. React. Eng.*, 2008, **6**.

406 P. Gallezot, *Chem. Soc. Rev.*, 2012, **41**, 1538–1558.

407 S. Nishimura, A. Takagaki and K. Ebitani, *Green Chem.*, 2013, **15**, 2026.

408 H. Xu, S. Ouyang, L. Liu, P. Reunchan, N. Umezawa and J. Ye, *J. Mater. Chem. A*, 2014, **2**, 12642.

409 W. Liu, A. Wang, J. Tang, S.-l. Chen, G. Yuan, K. Zhao, C. Li and X. Liu, *Microporous Mesoporous Mater.*, 2015, **204**, 143–148.

410 D. B. Gornowich and G. J. Blanchard, *J. Phys. Chem. C*, 2012, **116**, 12165–12171.

411 Y. Jiang, C. Cui, Y. Huang, X. Zhang and J. Gao, *Chem. Commun.*, 2014, **50**, 5490–5493.

412 D. Mersch, C. Y. Lee, J. Z. Zhang, K. Brinkert, J. C. Fontecilla-Camps, A. W. Rutherford and E. Reisner, *J. Am. Chem. Soc.*, 2015, **137**, 8541–8549.

413 O. Arutanti, A. B. Nandiyanto, T. Ogi, T. O. Kim and K. Okuyama, *ACS Appl. Mater. Interfaces*, 2015, **7**, 3009–3017.

414 A. Stein, *Nat. Nanotechnol.*, 2011, **6**, 262–263.

415 Y. Zhang, M. Dong, S. Zhu, C. Liu and Z. Wen, *Mater. Res. Bull.*, 2014, **49**, 448–453.

416 M. Park, Y. Kim, Y. Ko, S. Cheong, S. W. Ryu and J. Cho, *J. Am. Chem. Soc.*, 2014, **136**, 17213–17223.

417 Y. Wang, C. Y. Foo, T. K. Hoo, M. Ng and J. Lin, *Chem. – Eur. J.*, 2010, **16**, 3598–3603.

418 Y. Isshiki, M. Nakamura, S. Tabata, K. Dokko and M. Watanabe, *Polym. Adv. Technol.*, 2011, **22**, 1254–1260.

419 D. Y. Kim, J. Suk, D. W. Kim, Y. Kang, S. H. Im, Y. Yang and O. O. Park, *J. Mater. Chem. A*, 2014, **2**, 6396–6401.

420 J. H. Kim, J. H. Kim, K. H. Choi, H. K. Yu, J. H. Kim, J. S. Lee and S. Y. Lee, *Nano Lett.*, 2014, **14**, 4438–4448.

421 N. D. Petkovich, S. G. Rudisill, B. E. Wilson, A. Mukherjee and A. Stein, *Inorg. Chem.*, 2014, **53**, 1100–1112.

422 Y. Y. Hu, Z. Liu, K. W. Nam, O. J. Borkiewicz, J. Cheng, X. Hua, M. T. Dunstan, X. Yu, K. M. Wiaderek, L. S. Du, K. W. Chapman, P. J. Chupas, X. Q. Yang and C. P. Grey, *Nat. Mater.*, 2013, **12**, 1130–1136.

423 J. Ming, Y. Wu, J. B. Park, J. K. Lee, F. Zhao and Y. K. Sun, *Nanoscale*, 2013, **5**, 10390–10396.

424 M. P. B. Glazer, J. Cho, J. Almer, J. Okasinski, P. V. Braun and D. C. Dunand, *Adv. Energy Mater.*, 2015, **5**, 1500466.

425 H. Zhang and P. V. Braun, *Nano Lett.*, 2012, **12**, 2778–2783.

426 N. S. Ergang, J. C. Lytle, K. T. Lee, S. M. Oh, W. H. Smyrl and A. Stein, *Adv. Mater.*, 2006, **18**, 1750–1753.

427 A. Esmanski and G. A. Ozin, *Adv. Funct. Mater.*, 2009, **19**, 1999–2010.

428 C. M. Doherty, R. A. Caruso, B. M. Smarsly and C. J. Drummond, *Chem. Mater.*, 2009, **21**, 2895–2903.

429 D. Y. Kang, S. O. Kim, Y. J. Chae, J. K. Lee and J. H. Moon, *Langmuir*, 2013, **29**, 1192–1198.

430 M. Osiak, H. Geaney, E. Armstrong and C. O'Dwyer, *J. Mater. Chem. A*, 2014, **2**, 9433.

431 J.-J. Xu, Z.-L. Wang, D. Xu, F.-Z. Meng and X.-B. Zhang, *Energy Environ. Sci.*, 2014, **7**, 2213.

432 C. Y. Cho, H. N. Kim and J. H. Moon, *Phys. Chem. Chem. Phys.*, 2013, **15**, 10835–10840.

433 J. P. Bosco, K. Sasaki, M. Sadakane, W. Ueda and J. G. Chen, *Chem. Mater.*, 2010, **22**, 966–973.

434 H. Munakata, D. Yamamoto and K. Kanamura, *J. Power Sources*, 2008, **178**, 596–602.

435 L. Kong, Q. Dai, C. Miao, L. Xu and H. Song, *J. Colloid Interface Sci.*, 2015, **450**, 196–201.

436 S. Zhang, G.-Y. Dong, B. Lin, J. Qu, N.-Y. Yuan and J.-N. Ding, *J. Power Sources*, 2015, **277**, 52–58.

437 L. N. Quan, Y. H. Jang, Y. J. Jang, J. Kim, W. Lee, J. H. Moon and D. H. Kim, *ChemSusChem*, 2014, **7**, 2590–2596.

438 K. E. Roelofs, T. P. Brennan and S. F. Bent, *J. Phys. Chem. Lett.*, 2014, **5**, 348–360.

439 S.-J. Ha, J. S. Kim, C.-Y. Cho, J. W. Lee, H.-G. Han, T.-H. Kwon and J. H. Moon, *RSC Adv.*, 2014, **4**, 40980–40984.

440 L. Kong, Q. Dai, C. Miao, L. Xu and H. Song, *J. Colloid Interface Sci.*, 2015, **450**, 196–201.

441 Z. Tian and M. A. Snyder, *Langmuir*, 2014, **30**, 9828–9837.

442 L. T. Varghese, Y. Xuan, B. Niu, L. Fan, P. Bermel and M. Qi, *Adv. Opt. Mater.*, 2013, **1**, 692–698.

443 J. T. Park, W. S. Chi, D. K. Roh, S. H. Ahn and J. H. Kim, *Adv. Funct. Mater.*, 2013, **23**, 26–33.

444 N. Yantara, T. T. T. Pham, P. P. Boix and N. Mathews, *Phys. Chem. Chem. Phys.*, 2015, **17**, 21694–21701.

445 Y. Park, J. W. Lee, S.-J. Ha and J. H. Moon, *Nanoscale*, 2014, **6**, 3105–3109.

446 Y. F. Wang, K. N. Li, Y. F. Xu, H. S. Rao, C. Y. Su and D. B. Kuang, *Nanoscale*, 2013, **5**, 5940–5948.

447 C. Y. Cho and J. H. Moon, *Langmuir*, 2012, **28**, 9372–9377.

448 C. Battaglia, C. M. Hsu, K. Soderstrom, J. Escarre, F. J. Haug, M. Charriere, M. Boccard, M. Despeisse, D. T. Alexander, M. Cantoni, Y. Cui and C. Ballif, *ACS Nano*, 2012, **6**, 2790–2797.

449 C. V. Subban, I. C. Smith and F. J. Disalvo, *Small*, 2012, **8**, 2824–2832.

450 J. H. Shin, J. H. Kang, W. M. Jin, J. H. Park, Y. S. Cho and J. H. Moon, *Langmuir*, 2011, **27**, 856–860.

451 E. Arsenault, N. Soheilnia and G. A. Ozin, *ACS Nano*, 2011, **5**, 2984–2988.

452 S. Guldin, S. Huttner, M. Kolle, M. E. Welland, P. Muller-Buschbaum, R. H. Friend, U. Steiner and N. Tetreault, *Nano Lett.*, 2010, **10**, 2303–2309.

453 E. S. Kwak, W. Lee, N.-G. Park, J. Kim and H. Lee, *Adv. Funct. Mater.*, 2009, **19**, 1093–1099.

454 J. Qian, P. Liu, Y. Xiao, Y. Jiang, Y. Cao, X. Ai and H. Yang, *Adv. Mater.*, 2009, **21**, 3663–3667.

455 C. Y. Kuo and S. Y. Lu, *Nanotechnology*, 2008, **19**, 095705.

456 S. H. Lee, N. M. Abrams, P. G. Hoertz, G. D. Barber, L. I. Halaoui and T. E. Mallouk, *J. Phys. Chem. B*, 2008, **112**, 14415–14421.

457 S. Nishimura, N. Abrams, B. A. Lewis, L. I. Halaoui, T. E. Mallouk, K. D. Benkstein, J. van de Lagemaat and A. J. Frank, *J. Am. Chem. Soc.*, 2003, **125**, 6306–6310.

458 Y. Tang, Y. Zhang, W. Li, B. Ma and X. Chen, *Chem. Soc. Rev.*, 2015, **44**, 5926–5940.

459 R. Raccis, A. Nikoubashman, M. Retsch, U. Jonas, K. Koynov, H. J. Butt, C. N. Likos and G. Fytas, *ACS Nano*, 2011, **5**, 4607–4616.

460 T. Cherdhirankorn, M. Retsch, U. Jonas, H. J. Butt and K. Koynov, *Langmuir*, 2010, **26**, 10141–10146.

461 T. A. F. K. M. Karg, M. Retsch, C. Stelling, P. M. Reichstein, T. Honold, M. Thelakkat and A. Fery, *Mater. Today*, 2015, **18**, 185–205.

462 V. O. Williams, E. J. DeMarco, M. J. Katz, J. A. Libera, S. C. Riha, D. W. Kim, J. R. Avila, A. B. Martinson, J. W. Elam, M. J. Pellin, O. K. Farha and J. T. Hupp, *ACS Appl. Mater. Interfaces*, 2014, **6**, 12290–12294.

463 L. N. Quan, Y. H. Jang, K. A. Stoerzinger, K. J. May, Y. J. Jang, S. T. Kochuveedu, Y. Shao-Horn and D. H. Kim, *Phys. Chem. Chem. Phys.*, 2014, **16**, 9023–9030.

464 G. He and A. Manthiram, *Adv. Funct. Mater.*, 2014, **24**, 5277–5283.

465 H. Zhang, X. Yu and P. V. Braun, *Nat. Nanotechnol.*, 2011, **6**, 277–281.

466 N. D. Petkovich, B. E. Wilson, S. G. Rudisill and A. Stein, *ACS Appl. Mater. Interfaces*, 2014, **6**, 18215–18227.

467 J. I. L. Chen, G. von Freymann, S. Y. Choi, V. Kitaev and G. A. Ozin, *Adv. Mater.*, 2006, **18**, 1915–1919.

468 B. L. Ellis, P. Knauth and T. Djenizian, *Adv. Mater.*, 2014, **26**, 3368–3397.

469 G. Gao, H. B. Wu, B. Dong, S. Ding and X. W. D. Lou, *Adv. Sci.*, 2015, **2**.

470 J.-S. Lee, S. Tai Kim, R. Cao, N.-S. Choi, M. Liu, K. T. Lee and J. Cho, *Adv. Energy Mater.*, 2011, **1**, 34–50.

322 | *Chem. Soc. Rev.*, 2016, **45**, 281–322

This journal is © The Royal Society of Chemistry 2016